Environmental limitations in suction bucket based jacket foundation installation, using vertical lift-off from a jack-up vessel

N.T. van Doorn

July 13, 2016

TU Delft Delft University of Technology

SIEMENS

Environmental limitations in suction bucket based jacket foundation installation, using vertical lift-off from a jack-up vessel

Master of Science Thesis

Author:	N.T. van Doorn	
Committee:	Prof. dr. A. Metrikine	TU Delft - Chairman
	Ir. C. Keijdener	TU Delft
	Dr. ir. M.A.N. Hendriks	TU Delft
	Dr. F. Pisanò	TU Delft
	Dr. ir. K.N. van Dalen	TU Delft
	Ir. M. Reinders	Siemens Wind Power

July 13, 2016

TU Delft Delft University of Technology

SIEMENS

Summary

In order to stay ahead on trends in the growing market of offshore wind, Siemens Wind Power has been working on its own four-legged suction bucket based jacket foundation. The number of such foundations that are to be installed per wind park force installation works to take place over a long period of time, making it hard to plan around harsh weather conditions.

In order to find out whether installation works of this specific jacket design could take place in the same conditions as other offshore installation procedures, a 2D time domain MATLAB model has been created, containing the most important features of a heavy lifting jack-up crane vessel and its appropriate rigging elements. The model is used to calculate the forces in the crane cable, as a result of the jackets behaviour through its interaction with the water.

The environmental forces that act upon the jacket during the installation are based on a 40 meter deep ocean with an irregular wave field, modelled with the JONSWAP spectrum. The most important forces and influences caused by these waves have been incorporated in the model. For this specific jacket design some particular phenomena occur when the large suction buckets are lowered through the splash zone: an air cushion is created within the buckets and a vertical slamming arises when the water collides with the inner top. The latter initiates a jump in the jackets vertical velocity, resulting in oscillation in the crane.

With the resulting model, simulations are performed for a predefined set of wave combinations. The randomness of the irregular waves is taken into account by performing multiple simulations per wave combination, each using different initial conditions. A large number of such seeds (2000) were required to find out that the maximum dynamic amplification factor (DAF) values of the crane load cable has a Weibull distribution. In order to reduce computational time however, it is chosen to run only 50 simulations per wave condition of interest. Even though no statistically

profound conclusions can be drawn from these simulations, an insight is gained into which wave combinations should be handled with extra care. Those with a zero crossing period of 4 to 5 seconds showed resonant behaviour with the waves, resulting in un-acceptable slack and causing the load cable DAF values to exceed the maximum allowable value of 1.3. For significant wave heights of 2 meters, wave periods longer than 8 seconds showed tolerable DAF values.

For the wave conditions that showed intolerable DAF values, the jacket behaviour is studied more extensively, in order to find out what the individual force contributions are. Synchronization of the jackets vertical oscillation with the waves showed to be an important initiator of high load cable forces. Since the initial oscillations are caused by slamming and the jacket's eigen-period is affected by the heave added mass, these two phenomena are very important. Prevention of large cable forces can thus primarily be gained from reduction of both factors, e.g. by adjusting the rigging arrangement or the suction bucket design.

Acknowledgements

This report describes my master thesis for the master program Offshore and Dredging Engineering at the Delft University of Technology, which has been done in collaboration with Siemens Wind power.

Siemens Wind Power is a division within Siemens, focused on renewable wind energy. With more than 30 years experience in onshore- and 25 years in offshore-wind power business, she is one of the worlds market leaders within this field. The engineering division located in The Hague mainly focusses on the offshore wind sector and has a main goal of lowering its price per kWh, to ensure its long time future. She does so by invention of new technologies, by evolving existing products or simply by finding smarter ways of working.

I would really like to thank Siemens for giving me the opportunity to conduct this research and for providing me with a comfortable working environment to do so. I could always ask for professional opinions from the colleagues at the department, which helped me a lot with multiple tasks. I especially would like to thank Mark Reinders, my supervisor, for his input, his help and for the biweekly progress meetings we had.

Further I hereby thank Prof. Dr. Metrikine for the interesting discussions we have had during the progress meetings and my daily supervisor from the TU Delft, Chris Keijdener, for providing me with a lot of technical input and help, especially in MATLAB related problems. I had never used the program prior to this research and he had the patience to help guide me through its features and usage.

Lastly, I would like to thank Jasper for helping me with the report and most importantly my girlfriend, friends and family for the mental support throughout the process.

Tobias van Doorn, July 2016

Contents

List of Figures

List of Tables

Nomenclature

Latin symbols

A_c	Crane triangle length	m
a_{33}	Heave added mass	kg
A_γ	JONSWAP normalizing factor	$-$
A_p	Projected area	m^2
A_{ss}	Slamming area	m^2
A_{ti}	Inner bucket top area	m^2
A_v	Ventilation hole area	m^2
C	Coefficient	$-$
c	Wetted half-length	m
C_r	Contraction coefficient	$-$
C_s	Slamming coefficient	$-$
C_π	π drag coefficient	$-$
C_{pa}	Initial space average slamming pressure coefficient	$-$
D	Diameter	m
d	Water depth	m
E	Elevation	m
e_{tj}	Elevation between jacket's -COG and -top	m
F_g	Gravitational force	N
F_3	Vertical forces	N
F_{μ_s}	Suction force	N
F_μ	Air cushion pressure force	N
F_D	Drag force	N

F_e	Added mass force near seabed	N
F_I	Inertia force	N
F_m	Morison force	N
F_r	Resultant force	N
F_s	Slamming force	N
F_v	Vertical wave force	N
g	Gravitational acceleration	$\frac{m}{s^2}$
H	Wave height	m
h	Submergence	m
H_c	Crane triangle height	m
H_s	Significant wave height	m
h_{bi}	Inside bucket height	m
h_b	Distance to seabed	m
J	Mass moment of inertia	$\frac{kg}{m^2}$
k	Stiffness	$\frac{N}{m}$
k	Wave number	$\frac{rad}{m}$
K_c	Keulegan Carpenter number	$-$
k_{flow}	Pressure loss coefficient	$-$
k_s	Surface roughness	$-$
L	Length	m
L_{cur}	Deformed length	m
m	Mass	kg
P	Pressure	$\frac{N}{m^2}$
p	Perforation rate	$\%$
Q	Flux	$\frac{m^3}{s}$
Q_p	Exceedence probability	$-$
R	Radius	m
r	Arm	m
R_e	Reynold's number	$-$
s	Submergence	m
S_J	JONSWAP spectral density	$\frac{m^2}{Hz}$
S_{PM}	Pearson-Moskowitz spectral density	$\frac{m^2}{Hz}$

T	Kinetic energy	$Joule$
T	Wave period	s
t	Time	s
T_p	Peak wave period	s
T_z	Zero crossing period	s
$\dot{u}_{mf}$	Mac-Camy Fuchs horizontal wave particle acceleration	$\frac{m}{s^2}$
u	Elongation	m
u	Horizontal wave particle velocity	$\frac{m}{s}$
u_{rms}	Horizontal wave particle velocity root mean square	$\frac{m}{s}$
V	Volume	m^3
v	Velocity	$\frac{m}{s}$
v_b	Vertical bucket velocity	$\frac{m}{s}$
v_c	Crane lowering velocity	$\frac{m}{s}$
V_w	Volume of entrapped water	m^2
v_{wl}	Velocity left water volume	$\frac{m}{s}$
v_{wr}	Velocity right water volume	$\frac{m}{s}$
$\dot{u}$	Horizontal wave particle acceleration	$\frac{m}{s^2}$
$\dot{w}$	Vertical wave particle acceleration	$\frac{m}{s^2}$
w	Vertical wave particle velocity	$\frac{m}{s}$
$\ddot{x}$	Longitudinal acceleration	$\frac{m}{s^2}$
$\dot{x}$	Longitudinal velocity	$\frac{m}{s}$
x	Longitudinal direction / coordinate	m
y	Lateral direction / coordinate	m
z	Vertical direction / coordinate	m
z'	Wheeler transformed z coordinate	m
z_{ct}	Global crane tip z-coordinate	m

Greek symbols

α	Sling angle	rad
$\underline{\alpha}$	Random phase	rad
β	Wave direction	rad
β_b	Brace angle	rad
γ	JONSWAP peak shape parameter	$-$

γ_a	Specific heat ratio	$-$
γ_b	Boom hoist cable angle	rad
Δ	Critical flow regime	$\frac{1}{m}$
δ	Logarithmic damping decrement	$-$
ζ	Damping ratio	$-$
$\ddot{\eta}$	Surface acceleration	$\frac{m}{s^2}$
$\dot{\eta}$	Surface velocity	$\frac{m}{s}$
η	Surface elevation	m
η_a	Surface elevation amplitude	m
$\underline{\eta}_a$	Random surface elevation amplitude	m
$\ddot{\theta}$	Pitch rotational acceleration	$\frac{rad}{s^2}$
$\dot{\theta}$	Pitch rotational velocity	$\frac{rad}{s}$
θ	Pitch rotation	rad
λ	Wave length	m
λ_h	Structure height amplification factor	$-$
$\dot{\mu}$	Dynamic air pressure flux	$\frac{N}{m^2 s}$
$\dot{\mu}_s$	Suction dynamic air pressure flux	$\frac{N}{m^2 s}$
μ	Dynamic air pressure	$\frac{N}{m^2}$
μ_s	Suction dynamic air pressure	$\frac{N}{m^2}$
μ_u	Mean value horizontal wave particle velocity	$\frac{m}{s}$
ν	Kinematic viscosity	$\frac{m^2}{s}$
ρ	Density	$\frac{kg}{m^3}$
ρ_w	Density water	$\frac{kg}{m^3}$
ρ_{air}	Density air	$\frac{kg}{m^3}$
σ	Spectral width parameter	$-$
σ_u	Standard deviation horizontal wave particle velocity	$-$
ϕ	Roll motion	rad
ψ	Yaw motion	rad
ψ_w	Wake amplification factor	$-$
ω	Angular wave frequency	$\frac{rad}{s}$
ω_p	Angular spectral peak wave frequency	$\frac{rad}{s}$

Subscripts

∞	Maximum value
$\perp$	Perpendicular
0	Initial value
a	Added mass
$angle$	Under an angle
atm	Atmospheric
b	Boom
bhc	Boom hoist cable
c	Within the bucket
cb	Boom
d	Drag
h	Hook
i	Inertia
in	Inner/ inwards
out	Outer/ outwards
j	Jacket
$j + l$	Jacket plus left water volume
$j + l + r$	Jacket plus left and right water volume
lc	Load cable
$left$	At left side
max	Maximum value
mf	Mac-Camy Fuchs
mid	In the middle
rel	Relative
rig	Rigging
$right$	At right side
S	Solid
s	Sling
sub	Submerged
top	Top
tot	Total

Abbreviations

CAPEX	Capital expenditures
CFD	Computational Fluid Dynamics
COG	Center of Gravity
DNV	Det Norske Veritas
Ghz	Giga Hertz
JONSWAP	Joint North Sea wave project
kWh	Kilowatthour
MATLAB	Matrix labaratory
MSL	Mean Sea Level
ODE	Ordinary Differential Equation
RAO	Response Amplitude Operator
TP	Transition Piece
ULS	Ultimate Limit State

Chapter 1

Introduction

1.1 Problem description

These days, there is a global tendency to search for greener options for energy resourcing. A very good option is to harvest wind energy to generate electricity. Due to the fact that stronger wind speeds are available offshore compared to on land, offshore wind power is a very interesting field. The problem however still is that offshore wind farms are relatively expensive. Therefore, its price per kWh is higher than that of onshore wind farms. Nowadays, around 17% of the total Capital Expenditures (CAPEX) costs of offshore wind farms is made up by the foundation cost and another 4 % by installation of these foundations [16]. For onshore these two combined are good for 16% of the cost. This shows that these foundations form a high potential area to reduce the total costs. Therefore, research is being done in this field in order to design smarter solutions.

Nowadays, the most conventional solution for offshore wind foundations is a monopile: a hollow cylindrical steel structure with a certain diameter and wall thickness, which gets hammered into the soil. Looking at the current trend and future projects though, turbine sizes increase, as does the water depth at site, as is the prediction of amongst others renewable energy consultancies as BVG associates (2014) [42] and Stichting De Noordzee (2012) [43]. In order to be able to cope with the increasing (dynamic) loads resulting from this, the stiffness of the monopile is to be enlarged, hence its diameter and/or thickness is to be increased. These adoptions result in significant cost increases, making monopiles less economically feasible. Therefore, the industry has come up with other solutions, one of which is a

suction bucket based jacket foundation: a truss structure which by its configuration has a higher stiffness, thus is capable of coping with the increased loads. Furthermore, reports by Stichting De Noordzee in 2012 [43] state that the installation of these suction bucket founded structures has a benefit of low noise emission compared to piling procedures, a reduction of installation time offshore due to its lower amount of operation steps and the ability to fully and more easily decommission. Siemens Wind Power therefore is confident the future industry will demand such jacket structures and thus is working on its own design.

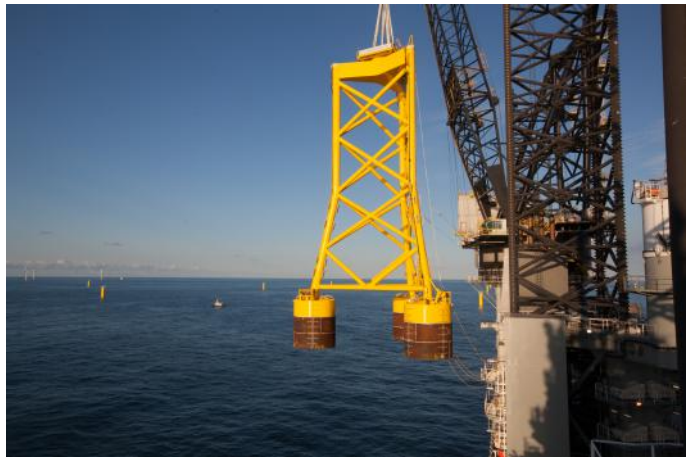

Figure 1.1: Three-legged suction bucket based jacket foundation installation at the Borkum Riffgrund project

Most wind towers/jackets that are or will be installed contain piles instead of buckets (e.g. projects as Beatrice, Alpha Ventus, Ormonde, Nordsee Ost). The oil and gas industry however does contain several suction bucket based jackets (e.g. Sleipner T, Draupner) which, because of their size, are mostly installed via a launch and upend method. Suction bucket mono-leg structure lift-off installation has been done for met masts at Dogger bank and Horns Rev2. Two more comparable projects done are one three-legged tower with suction buckets at Borkum Riffgrund (figure 1.1), one four-legged tower with suction buckets at Amstel Q13a-A (gas field) and several subsea suction bucket structures. In the near future, suction bucket based jackets for the wind projects Dudgeon, Burbo Bank Extension, Race Bank and Walney Extension will be installed (mainly for transformation platforms). The main

difference with the oil and gas industry is the amount of structures to be installed within a project. Oil and gas fields mostly require one large structure, where offshore wind farms usually conduct a vast amount of relatively smaller structures, resulting in multiple logistic challenges. These challenges mainly are seen in the offshore installation: Where the oil and gas industry can time their installation based on weather window, the offshore wind industry must spread its installation works over a larger amount of time, thus will be facing more rough weather. In order to minimize losses, workability should be as high as possible. Due to the fact that big offshore wind-projects containing these kinds of jacket structures are non existing yet, Siemens would like to make sure that such installation works can safely be performed in the same conditions as other offshore installation procedures: within the range of $2\ m$ significant wave height (H_s). This range secures a workability of approximately 70 % per year, which is required in order for the project to be economically feasible, according to Thomsen (2014) [40]. Another wave characteristic that highly effects the forces induced by the water is the wave period. In this thesis therefore combinations of the significant wave height with the wave period (in this case the zero-crossing period T_z) are studied.

1.2 Objective

The scope of this research is to find out, from an engineering point of view, what the critical stages and environmental limits are for suction-bucket-based jacket foundation installation using a heavy lifting jack-up vessel. This is done in order to technically support the assumption that these procedures can be performed in the same workability range as other comparable offshore installations. The environmental limits are defined in terms of combinations in significant wave height H_s and wave period T_z.

1.3 Approach

The boundaries of the to be determined environmental limits are based on safety, crane capabilities and comfort and are to be calculated by checking the responses off, and loads on equipment due to the interaction with the environment. This is done via hydrodynamic modelling of the system, describing interactions between the crane, jacket, waves and current. In order to do so, the theory behind the waves, the criteria to be satisfied and the installation stages during the procedure are to be explained, which is done in chapter 2. The model used to calculate loads and

displacements is created in MATLAB and is used to run a full-installation period for different sets of sea states, in the time domain. How the basis of this model is created, containing an explanation on how the crane and its lifting elements is modelled, can be found in chapter 3. An approximation of the set of hydrodynamic forces that in reality will act upon the structure is then included in this model. These forces, induced by the interaction between the water and jacket, are described in chapter 4. By keeping track of the displacements and velocities of the structure- and crane elements, the forces in lifting gear can be calculated. By comparing these obtained values with pre-set criteria, the limiting situations can be filtered out and maximum environmental conditions can be found. Statistical reliability of the values obtained can either be achieved by performing a series of simulations with different wave trains, by analysing a predetermined most unfavourable position or by using (very time consuming) computational Navier-Stokes solvers (CFD). In this thesis, the first two methods are used: In chapter 5, such studies are performed, together with the analysis of the results: which of the described forces influence the displacements the most severely and could adjustments be made in order to create a wider range of environmental conditions in which operations can take place? With the knowledge gained from these analysis, a first iterative step can be introduced in order to improve the model and design. Recommendations on these improvements, as well ass assumptions made in this thesis are discussed in chapter 6. Some of the assumable most effective adjustments are argued by implementing them in the model and comparing the results. The most important findings are summarized in chapter 7.

A quick overview of the project and summary of this section is presented in the flowchart in figure 1.2:

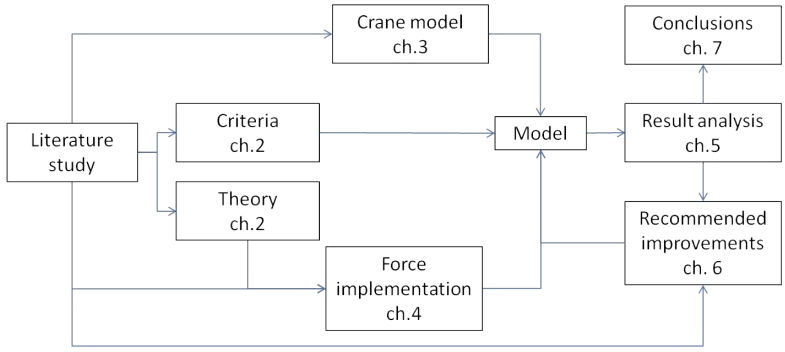

Figure 1.2: Flowchart of the project and the respective chapters

1.4 Jacket design

As was mentioned in section 1.1, in order to be one step ahead on the industry, Siemens is working on its own jacket design. An isometric view of this design can be found in figure 1.3a. As can be seen, the foundation package consist out of a four-legged suction bucket based jacket, with a separate concrete transition piece (TP) structure on top of it. The installation procedure is to separately install these two elements, in order to reduce maximum static weight in the cable. In this research, only the installation of the jacket will be considered. This part of the structure is build up from four large cylindrical, closed top suction buckets, each having a diameter of $9.5\ m$ and a height equal to that value (figure 1.3b). On top of these buckets four legs are positioned, which are held in place by one layer of horizontal braces and three layers of diagonal x-braces. The total footprint of the structure is $28\ m^2$, the total height is $66\ m$ and its total mass is $1,175\ t$. More details on the design can be found in appendix A.

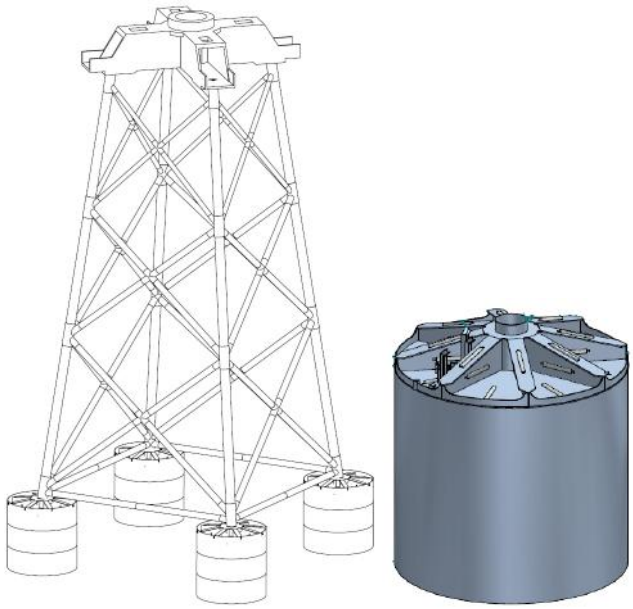

(a) Jacket **(b)** Bucket

Figure 1.3: Isometric view Siemens' jacket and bucket design

1.5 Offshore installation

The vast majority of offshore wind farms is installed by the use of jack-up vessels/barges (figure 1.4a): self-elevating units, consisting of a buoyant (either ship- or barge-shaped) hull with a number of legs (generally 3 to 6), which can be stationed on the sea floor, raising the hull over the sea-surface and there with provide a stable work platform at sea. Jack-up vessels/barges dominate the offshore wind energy market due to this property, combined with their relatively low day rate (compared to heavy lifting floating vessels/barges).

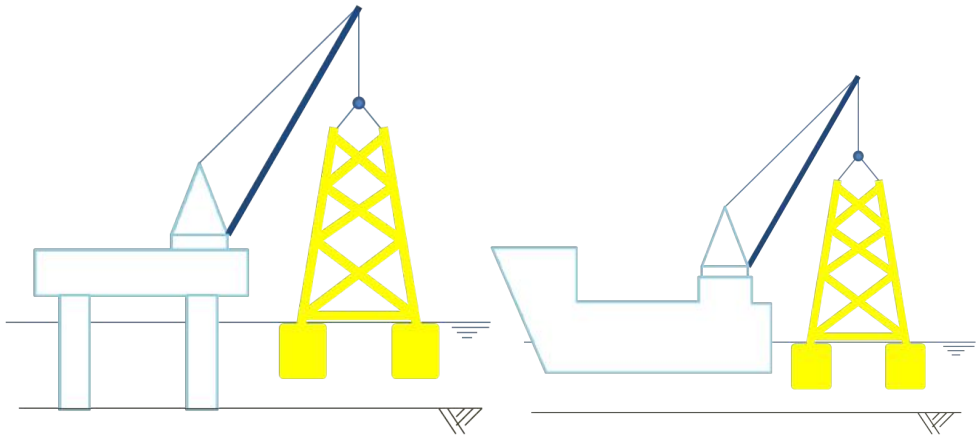

(a) Jack-up vessel **(b)** Floating vessel

Figure 1.4: Two different types of vessels used for offshore installation

Another type of vessel used in practice is the floating kind (figure 1.4b). The benefit of these types of vessels over jack-ups primarily lies in the possibility to install at bigger water depths, due to the fact that these vessels are not limited by the length of the legs. They can be kept in position using either anchors or dynamic positioning. Hydro-dynamically however, this option is totally different than the jack-up, mainly due to the fact that the vessel itself will now move due to environmental influences These movements cause the crane tip to have its own deflection- velocity- and acceleration. Furthermore, the shape of the vessel in the water will result in change of surrounding water movement and cause shielding effects. The orientation of the vessel and jacket therefore plays an important role on hydrodynamic behaviour, according to Li [28]. Even though for Siemens the future of this case is fairly insecure

from a financial perspective, it is believed that it is an interesting scenario, as floating vessels are better suitable for jacket installation, due to their large deck space. For this thesis however, the jack-up vessel is chosen to be worked with: the permeability of the legs make shielding effects negligible, so only incident waves upon the jacket structure are to be considered. Furthermore, the jack-up can be seen as a fixed structure; no wave induced vessel movements occur and therefore the crane does not move either. Even though it would be very interesting to compare the results from these studies with that of a floating vessel, unfortunately actual response amplitude operators (RAO's, parameters used to determine the behaviour of vessels in waves) are not available. Due to the fact that for floating vessels even more parameters influence the results, these will not be accurate enough. Performing the study on jack-up vessels will bring a good first prediction, which could be used for further studies on floating vessels in a later stage.

Chapter 2

Theories

In order to be able to create a model containing hydrodynamic forces and influences, it is important to create insight in the theories behind it. In this chapter therefore a brief introduction on motion definitions, in section 2.1, and wave theories used throughout the project, in section 2.2, are given. The forces induced by this oceanic behaviour induce jacket displacements and forces in the crane and its cables. In order to be able to find out what the limiting environmental conditions are, the criteria which are to be satisfied should be defined. This is done in section 2.3. The different stages during the full installation of the jacket are provided in section 2.4.

2.1 Motion definitions

In general, objects have a total of six degrees of freedom, three of which are translational and three of which are rotational (figure 2.1a). The translational degrees of freedom in respectively x (longitudinal), y (lateral) and z (vertical) direction are surge, sway and heave. The rotational degrees of freedom turning around respectively x, y and z axis are roll (φ), pitch (θ) and yaw (ψ). In this project however, it is chosen only to consider a 2D situation, with a total set of three degrees of freedom: heave, surge and pitch (figure 2.1b). This is done based on the assumption that for such heavy crane loads the vertical forces and displacements will be of highest importance for the dynamic crane forcing. Considering a 3D system brings a lot of additional mutual dependencies between degrees of freedom. The complexity this problem results in is considered not to weigh up to the physical effect it has on the load cable forces: It is assumed that the moments and forces in other directions than

x, z and θ have a lower influence upon the determination of the maximum environmental conditions. The wave direction is chosen accordingly, in order to describe worst case scenarios.

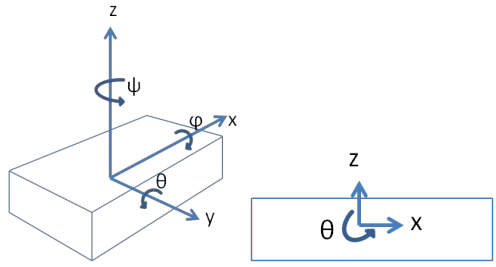

(a) 3D **(b)** 2D

Figure 2.1: Motion definitions

The equations of motion upon this 2D structure is given by Newtons second law of dynamics:

$$\sum_{j=1}^{3} M_{i,j}\ddot{q}_j = F_i \qquad i = 1 \dots 3 \tag{2.1}$$

Here, $M_{i,j}$ is a $3x3$ matrix of solid mass and inertia of the body, $\ddot{q}_j$ describes the acceleration of the body in direction j and F_i accounts for the sum of forces or moments that act in direction i.

2.2 Wave theory

In order to be able to determine the wave excitation loads, an understanding of wave properties is needed. Firstly, a regular wave will be described, propagating with a permanent wavelength, -period and -height, as can be seen in figure 2.2.

λ describes the wave length $[m]$, H the wave height $[m]$, η the surface elevation $[m]$ and d the water depth $[m]$. Other important properties are T the wave period $[s]$, angular wave frequency $\omega = \frac{2\pi}{T}$ $[\frac{rad}{s}]$ and wave number $k = \frac{2\pi}{\lambda}$ $[\frac{rad}{m}]$.

The surface elevation η of a regular wave can be described in a two-dimensional form, with x-and y describing the horizontal positions relative to the neutral position and β the wave direction. As explained before however, in this thesis only

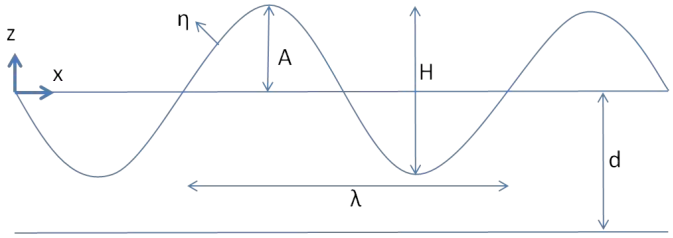

Figure 2.2: Wave defenitions

unidirectional waves will be considered. Therefore, y and β are considered to be zero. The wave surface elevation η as a function of time t and position x can now be described and by time differentiation, the surface velocity ($\dot{\eta}$) and acceleration ($\ddot{\eta}$) can be determined:

$$\eta(x,t) = \eta_a \sin(\omega t - kx) \tag{2.2a}$$
$$\dot{\eta}(x,t) = \omega\eta_a \cos(\omega t - kx) \tag{2.2b}$$
$$\ddot{\eta}(x,t) = -\omega^2\eta_a \sin(\omega t - kx) \tag{2.2c}$$

Ocean waves in reality though are irregular and random in shape, height, length, and speed of propagation. These irregular waves can be modelled as a summation of many sinusoidal wave components, each having its own frequency ω, amplitude $\underline{\eta}_{a_i}$, and phase $\underline{\alpha}_i$ (uniformly distributed between 0 and 2π) [20]. The underscores here indicate random variables. For a set of representative frequencies, the irregular wave elevation can be calculated by equation 2.3. The wave number here is directly related to the frequencies, through the dispersion relation in equation 2.4.

$$\underline{\eta}(xt) = \sum_{i=1}^{N} \underline{\eta}_{a_i} \sin(\omega_i t - k_i x + \underline{\alpha}_i) \tag{2.3}$$

$$\omega^2 = gk\tanh(kd) \tag{2.4}$$

In order to obtain the set of wave amplitudes linked to the chosen set of frequencies, a sea spectrum will be used, describing the distribution of wave energy over the representative frequencies. In this research, the JONSWAP spectrum is used for calculations. This spectrum is a modification on the Pierson-Moskowitz spectrum, which is based on data from the North Atlantic, for a developing sea state in a fetch

limited situation [20][25]. The equations involved in these spectra are given in appendix B.

The required inputs for the spectrum are the significant wave height H_s and the zero crossing period T_z. The ranges of these parameters are based on normal offshore installation ranges. Typically, a H_s up to $2\ m$ is considered to be the maximum wave height for safe installation works during offshore installation. As was stated in the previous chapter, by this thesis Siemens would like to investigate that installation works of their jacket structure can be done at these sea states. Therefore, for calculations, a maximum considered H_s of $2.5\ m$ will be used, with intermediate steps of $0.5\ m$. Det Norske Veritas (DNV) guidelines state that for these calculations, the T_z range that should be considered is given by equation (2.5) [9]. For T_z, intermediate steps of $1\ s$ will be used.

$$8.9\sqrt{\frac{H_s}{g}} \leq T_z \leq 13 \tag{2.5}$$

In figure 2.3a, the JONSWAP spectrum is created for H_s of $1\ m$, T_z of $9\ s$ and for 100 frequencies between $0\ \frac{rad}{s}$ and 3 times the peak frequency.

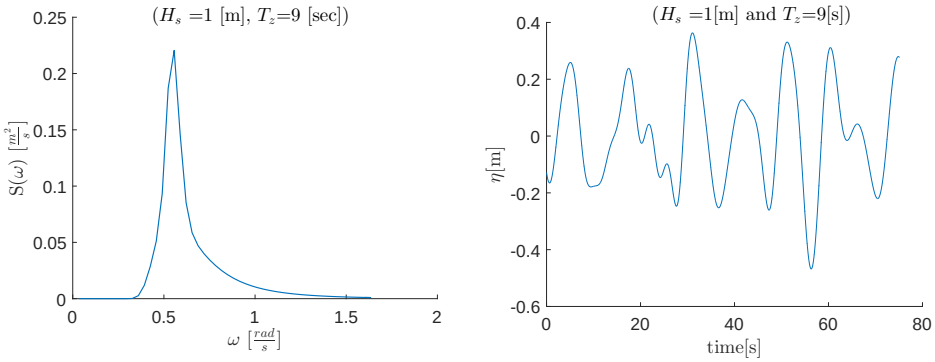

(a) JONSWAP spectrum **(b)** Irregular wave

Figure 2.3: Irregular wave created by use of the JONSWAP spectrum

In order to create an irregular wave using the obtained spectrum, an inverse Fourier transformation should be performed. The values of the JONSWAP spectrum can be used in order to calculate the wave amplitude η_{a_i} (equation 2.6). Now, by randomly choosing a phase α_i between 0 and 2π, all parameters of equation 2.3 are

calculated and the irregular wave elevation for the representative set of frequencies is created. This irregular wave is shown in figure 2.3b.

$$\eta_{a_i} = \sqrt{2S_J(\omega_i)\Delta\omega} \tag{2.6}$$

In the model, the phases that are chosen in correspondence with the wave frequencies are generated randomly by MATLAB. Due to the fact that it will choose these phases randomly each time the program is ran, the irregular wave will always be different from the last time it ran. In order to prevent this, the seed that MATLAB uses to find a random number is kept constant. By doing so, it will choose the exact same random phases for each run. The danger in this however is, that large forces, induced by differently chosen phases could possibly not be encountered: most hydrodynamic forces highly depend on the wave pattern and therefore on the phases in which they occur. In order to incorporate all possible forces and to be able to draw more statistical conclusions, for each wave combination multiple calculations are to be performed, each having differently chosen random phases.

2.2.1 Wave kinematics

Forces induced by waves are related to the water particle speed and/or accelerations. These values can be calculated by the description of the waves, as was described earlier in this chapter.

In the most general form, flow motion of any fluid can be described by Navier-Stokes equations, which uses the continuity equation (conservation of mass), conservation of momentum and the state equation for liquids. Using these phenomena, both the horizontal (u) and vertical (w) water particle velocity of regular waves in general, deep and shallow water can be described, which is done in respectively equations 2.7 and 2.8[20]. By time differentiation, the accelerations can easily be calculated too. Due to the fact that linear theory in irregular waves is used, this procedure is to be be repeated for each singular wave frequency considered. For each of these components, kd should be checked and its adequate horizontal and vertical wave particle velocity and acceleration should be calculated using formulas 2.7 and 2.8. The kinematics of the irregular wave can then be described by the summation of all these components.

$$u = \begin{cases} \frac{\eta_a \omega}{kd} \sin(\omega t - kx) & \text{if } kd < 0.3 \text{ (shallow)}; \\ \eta_a \omega \frac{\cosh(k(d+z))}{\sinh(kd)} \sin(\omega t - kx) & \text{if } 0.3 \leq kd \leq 3; \\ \eta_a \omega e^{kz} \sin(\omega t - kx) & \text{if } kd > 3 \text{ (deep)}. \end{cases} \tag{2.7}$$

$$w = \begin{cases} \eta_a \omega (1 + \frac{z}{d}) \cos(\omega t - kx) & \text{if } kd < 0.3 \text{ (shallow)}; \\ \eta_a \omega \frac{\sinh(k(d+z))}{\sinh(kd)} \cos(\omega t - kx) & \text{if } 0.3 \leq kd \leq 3; \\ \eta_a \omega e^{kz} \cos(\omega t - kx) & \text{if } kd > 3 \text{ (deep)}. \end{cases} \tag{2.8}$$

How the obtained values will be implemented into forcing, will be explained more elaborately in chapter 4.

2.2.2 Wave stretching

In order to be able to describe the horizontal wave velocity for each elevation above Mean Sea Level (MSL), an extension of the velocity profile is to be described. Different theories are developed for this stretching, each using linear theory [25]. Three theories are sketched in figure 2.4: the first one is to extrapolate the linear profile under MSL above MSL. In reality, this theory might give somewhat too high values above MSL. Therefore, another option is created, using the velocity at MSL for each elevation above this elevation. This theory however does not properly show the difference in velocity above MSL. Therefore, the last option is chosen for this thesis: the often used Wheeler profile stretching, which replaces the original vertical coordinate z by a rewritten vertical coordinate, such that the linear horizontal velocity at MSL is relocated upwards.

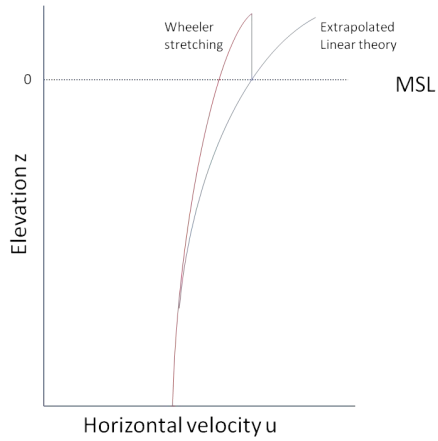

Figure 2.4: Horizontal velocity stretching

2.3 Criteria

In this section, the criteria are sketched, which are to be satisfied during the entire installation phase. As was mentioned in section 1.1, in practice these criteria are mainly formed by safety, maximum crane capacity and comfort for the people involved. The criteria used in this thesis mainly are linked the first two of these conditions:

- Maximum allowable dynamic load should be lower than the dynamic crane-, structure-, and lifting equipment-capacity. According to DNV, equipment in general is designed for a dynamic amplification factor (DAF) of 1.3 [10]. In this thesis, it is chosen to check these values for the crane cable, since its properties could not be adjusted. If for instance the dynamic forces would exceed the maximum value of the slings, or other replaceable elements, the problem could be solved simply by using other slings. For the crane cable this is not the case. Therefore, the DAF factor in this case is calculated by dividing the total set of forces in the load cable F_{lc} by that of the initial static forces (the weight in air of all elements hanging in that specific crane element ($m_{tot}g$)), as can be seen in equation 2.9. The first criterion states that this DAF should at all times be smaller than 1.3.

$$DAF = \frac{F_{lc}}{m_{tot}g} < 1.3 \tag{2.9}$$

- Secondly, cable slack should at all times be avoided, since the vertical relative velocity between the jacket and the crane tip can induce snap forces, inducing large displacements, an increase of the DAF and thus a higher chance of failure. The force in the lifting wire should therefore at all times contain at least 10 % of the static weight of the lifted object, written in calculable terms in equation 2.10. The static weight here is the weight hanging in the hook minus the buoyancy, calculated by $\rho_w g V_{sub}$, with V_{sub} being the submerged volume. This second criterion, written in equation 2.10, is assumed to be an adequate safety level with respect to the Ultimate Limit State (ULS) criteria, according to DNV [9].

$$\frac{F_{lc}}{0.1(m_{tot}g - \rho_w g V_{sub})} \geq 1 \tag{2.10}$$

If either one of the criteria described above is not satisfied, the operation with these environmental conditions can not take place in a safe manner and should not be performed.

2.4 Installation stages

According to e.g. DNV [9] and Kopsov (1995)[26], an offshore installation process in general contains four different stages that should be considered, each having its own main features of dynamic loading. These stages, listed in table 2.1, lead to external dynamic forces, which are to be added to the equation of motion of the system. Since the system highly depends on multiple environmental aspects, the most critical stage is not known forehand. In the coming subsections, the stages will be explained more elaborately.

Installation stage	**Main features of dynamic loading**
Lifting from deck/ above water	Pendulum motion of structure due to crane tip movement.
Lowering through splash zone	Air cushion inside bucket, slamming, immersion dependant changes in buoyancy and added mass.
Lowering towards seabed	Constant change of mass distribution and wetted surfaces.
Landing on seabed	Upward forces due to hydrodynamic pressure within the bucket, exit forces, changes in hydrodynamic coefficients and soil resistance.

Table 2.1: The installation stages and their main features of dynamic loading

2.4.1 Lifting from deck

When a structure is lifted, a pendulum is created from the structure hanging in the crane wires. In case of a stationary jack-up vessel the dynamic analysis for lifting in air plays a minor role and emphasis should be put on the remaining installation stages. In this research therefore, calculations will be performed starting with the jacket hanging in air, just over its target position. Initial displacements caused by slewing of the crane and wind will not be considered.

2.4.2 Lowering through the splash zone

Model tests performed by Bunnik (2004)[3] show strong non-linearity in the splash zone lowering process, caused by buoyancy effects in waves, impact loads, changes in added mass, damping effects and complex water flows. These effects might lead to unwanted oscillations, slack, and or large vertical loads. Apart from the change in buoyancy of the structure, Naess (2014) [32] states that by a sudden change in added mass, caused by water hitting the top of a suction bucket, a slamming force in vertical direction is induced, proportional to the relative velocity between the surface and the object. Due to the fact that this possibly is a high vertical impact-force, it could enforce slack and thus endanger the safety of work.

Another interesting factor that strongly influences dynamic effects in this stage is the so-called air cushion phenomena: When a bucket is lowered through the splash zone, there will be some air trapped within the bucket. This air creates a dynamic pressure, which has an effect on the buoyancy forces inside the bucket. Sufficient ventilation of air should be provided, in order to minimize these buoyancy forces. If this ventilation is not sufficient, the vertical upward buoyancy force might lead to higher proportions than the downward forces, causing either the structure to tilt and or loss of tension in lifting gear.

2.4.3 Lowering towards seabed

In the subsequent installation phase, where the jacket is lowered in between the splash zone and the seabed, the waves and current have large areas to act upon. For the submerged part of the structure, the buckets, several braces, and parts of the legs, the loads created by the kinematics described earlier are to be calculated, both horizontally and vertically. These forces are drag- and inertia based and depend on the relative velocities and accelerations of the water and the jacket. On top of these forces, mass distribution and wetted surface constantly change in this stage, leading to constant shifts in buoyancy forces and hydrodynamic coefficients.

2.4.4 Landing on seabed

When the jacket reaches close proximity to the seabed, the buckets will be introduced to some phenomena that influence the structure's behaviour: Upward forces due to hydrodynamic pressure within the bucket, water exit forces, and changes in hydrodynamic coefficients are induced in these regions. Once the jacket is lowered to the ground, the suction bucket will sink to a certain depth by its own weight. Because of the fact that this process is to a large extent uncontrolled, the structure

must be placed as perpendicular to the ground as possible, in order to avoid local stress peaks in the skirts when they touch the seabed. In this stage the response of the structure is very complex, due to the influence of the seabed and the interrelation between the lowering speed and crane tip oscillation cycle. The interaction with the soil is an entirely different study and will therefore not be considered in this research: Only the region where the bucket reaches close proximity to the seabed will be discussed.

2.5 Theories summary

In this chapter the theories behind structure-water interactions are described. Firstly the motion definitions used in this thesis have been explained. A very important assumption is made, by considering a 2D situation. The theory behind the modelling of the waves, the JONSWAP spectrum, is given and its usage to create input for the hydrodynamic forces, in terms of wave elevation- and kinematics is described. The criteria that are tested are given: At all times, the DAF of the load cable should be lower than 1.3 and slack should be avoided. In this thesis, the system will be tested for these criteria, from the moment the jacket hangs above its target position, in air, until the moment it reaches close proximity of the seabed.

Chapter 3

MATLAB model

In this chapter, the basics of the model that is created is explained. In MATLAB, a 2D representation of the jacket combined with its rigging is modelled. The latter contains a rigid crane boom, which is being held in place by an elastic boom hoist cable. Hanging in this boom are an elastic crane load cable, a hook, and a set of elastic slings. The jacket itself is considered to be rigid, since deformations of the structure are of no interest within this project.

The model is built up in small intermediate steps: At first, in section 3.1, the load cable is discretized and modelled as an elastic pendulum with a mass at its end. After that, the crane boom with its hoist cable is added, in section 3.2 and lastly the slings, crane lowering and jacket are modelled, in section 3.3, 3.4 and 3.5 respectively. The structural parameters used for calculations, for both the jacket and the rigging elements, can be found in appendix A.

The forces within the elastic elements of the model are determined using relative distances between nodes of that particular element. Knowing the displacements of these nodes, the elongation of the element can be calculated, which, when multiplied with the stiffness, represents the force within the element. The acquired node forces are added to the equations of motion. In order to be able to solve these equations, a state space representation of each nodal degree of freedom is created. This state space is then solved using MATLAB's ODE45 solver. Per time unit, it calculates the displacements, velocities, and accelerations, which are used again as an input for the calculations of the next time step. A check on the behaviour of the jacket hanging in the crane is performed in section 3.6.

How exactly the basis of the model is created, is to be found in the upcoming sections.

3.1 Load cable

As a first step, the load cable is modelled as an elastic pendulum with one fixed end, and a mass at the other end. The cable is discretized into N elements, which are seen as massless linear springs with a lumped mass at the end (the nodes). For each time step the relative distance between two nodes is calculated, by adding (tension) or subtracting (compression) the displacements to the length (figure 3.1). The deformed length of the cable element can then be solved by using equation 3.1.

$$L_{cur,i} = \sqrt{(x_i - x_{i-1})^2 + (z_i - z_{i-1})^2} \tag{3.1}$$

By subtracting this new length with its old, non-deformed length, and by multiplying this value with the stiffness, the force within the element is calculated, as can be seen in equation 3.2. Its x- and z-component can be used in the representative equation of motion. By using this method, the equations of motions become coupled and non linear, so traditional stiffness matrices can not be used in the solver; a force array is to be used instead.

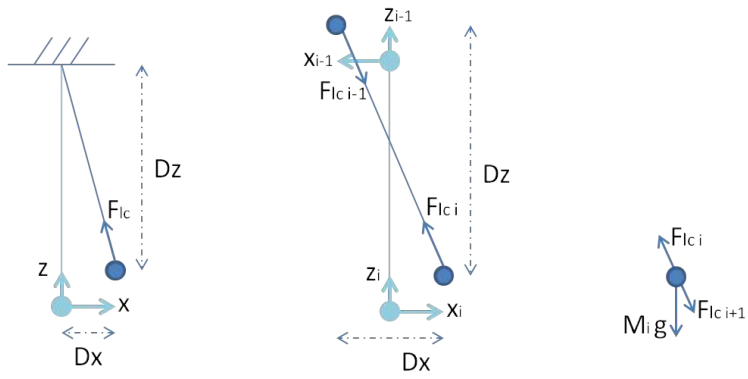

Figure 3.1: Cable nodal free body diagram

$$\begin{aligned} F_{lcx,i} &= k(L_{cur,i} - L_i)\tfrac{x_i - x_{i-1}}{L_{cur,i}}; \\ F_{lcz,i} &= k(L_{cur,i} - L_i)\tfrac{z_i - z_{i-1}}{L_{cur,i}} \end{aligned} \tag{3.2}$$

In order to model the initial position of the system, the pre-tension of the cable should be considered, which causes an initial elongation of the cable elements.

When this phenomena would not be taken into account, the system will not be in rest when all initial conditions are zero. The pre-tension is different for each element: since more summed weight hangs in the elements higher up, the elongation in these elements will be slightly higher than the ones below. When calculated via equation 3.3, the element elongation is used as the initial displacement of the representative nodes.

$$u_0 = \frac{\sum mg}{k} \tag{3.3}$$

Knowing the initial conditions, the parameters of the system, and how the forces are calculated, the model can be solved. For each degree of freedom, a state space is composed, describing the equation of motion. In this case it includes the forces in the cable ($\mathbf{F_{lc}}$) and those due to gravity ($\mathbf{F_g}$). By multiplying these vectors with the inverse mass matrix ($\mathbf{M^{-1}}$) and using equation 3.4, the accelerations can be calculated. By doing so for the entire system and by providing MATLAB's ODE45 solver with initial conditions and a time span, the displacements and velocities of all nodes can be calculated.

$$\ddot{\mathbf{x}} = \mathbf{M^{-1}}\mathbf{F_{lc}}(\mathbf{x}) - \mathbf{M^{-1}}\mathbf{F_g}(\mathbf{x}) \tag{3.4}$$

As a test, this method is used for a simple one-element cable. When no initial displacements are given and no external forces are working on the mass, the displacements should be, and stay zero. Solving this problem with MATLAB though, for cases with a high stiffness to mass ratio, a numerical error arises: When the pre-tensioned elongation of the cable is calculated outside of the solver and used in the solver, a non-zero difference in the order of 10^{-14} shows. This error causes a small displacement in the z-direction, which results in the mass to oscillate around its initial position, with an increasing amplitude. The growth of the amplitude stops after a certain amount of time, possibly because the relative cumulative error at that time instant is sufficiently high for the tolerances of the solver to be recognised and to be stopped by using more iteration steps.

A visualisation of such a growing error can be found in figure 3.2. Here, a stiffness of $26\ \frac{N}{m}$, a mass of $50\ kg$ and a cable length of $10\ m$ is used. For readability reasons, the time range is chosen to be lower than the range where the growth of the error stops, which in this case is at approximately $10,000\ s$.

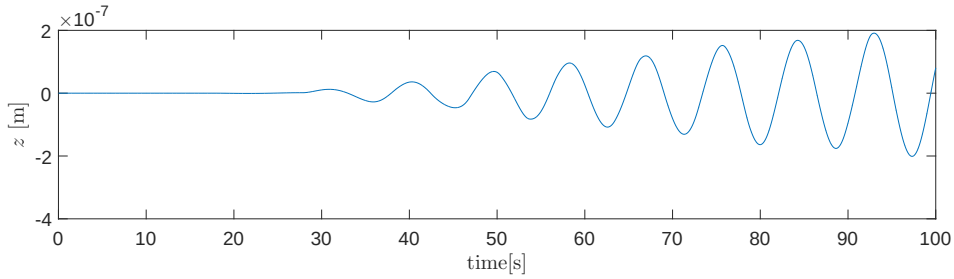

Figure 3.2: Vertical displacements of the elastic pendulum

Since the behaviour of the structure in the crane cable is the base of the model, it is important that this part of the model is validated to be correct. This is done using a Java Script, which calculates a double pendulum with elastic rods in the same way the cable is modelled [11]. The parameters of the cable model are set equal to those of the script, and its motions are monitored. The outcome of this validation is to be found in appendix C.

The properties of the load cable that are used for further calculations are based on 'Surelift 35' cables, widely used in offshore cranes [21]. In total, a set of eight cables are used, with a diameter of $44\ mm$, a mass of $9.83\ \frac{kg}{m}$, and a minimum breaking load of $191\ t$.

The effect of using more load cable elements upon the numerical error is discussed in appendix D, together with the numerical errors found when the model is extended as treated in the remaining of this chapter. Since conclusions on the amount of load cable elements to be used can only be drawn when the model is completed with forces, this number will be chosen later on, in section 4.7.

3.2 Crane boom

As a next step in the design of the crane model, a crane boom is added to the system, which is held in place by an elastic boom hoisting cable. A consideration should be made on whether or not taking crane boom elasticity into account. For this thesis, the additional work and complexity of calculations do not weigh up to the additional accuracy it induces: Park et al in 2011 [36] have compared the dynamic factor of an installation with an elastic versus a rigid crane. The difference found was 1.0-4.3 %. In addition to this relatively small influence, the crane stiffness and properties are

hard to properly define. The boom is therefore modelled as a rigid structure, which is able to rotate around its origin and thus creates an extra degree of freedom to the system. Using this rotation angle, the dynamic crane tip position can be described, which is required for the determination of the system's displacements and behaviour.

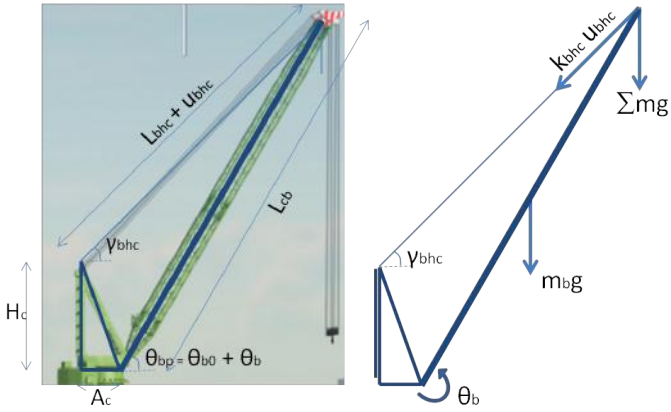

(a) Crane boom geometry **(b)** Crane boom statics

Figure 3.3: Geometry and statics of the crane boom

Definitions in geometry of the crane boom can be found in figure 3.3a. Dimensions are based on the 'Liebherr crane around the leg', with a main length of $108\ m$, a main lift capacity of $1,700\ t$ and a maximum tilting moment of $64,000\ tm$. This exact crane is installed on the 'Innovation': a heavy lifting jack-up vessel, which is primarily used for offshore wind installation projects. The properties of the boom hoist cable are based on 'PS620 cables', by WireRope Industries [21]. In total, a set of fourteen cables are used, each having a diameter of $57\ mm$, a mass of $13.93\ \frac{kg}{m}$ and a nominal breaking load of $247\ t$.

The load that is hanging in the hook causes an initial rotation of the boom, hence an initial elongation of the boom hoist cable. These values are required knowledge for the initial displacements of the nodes of the load cable and later the jacket. The static forces that act on the boom are represented in figure 3.3b. In order to find the value of the boom angle displacement, θ_b, for which the moments around the boom base are zero, all θ_b-dependant forces and geometry should be written in terms of

this angle. With these terms the static equation should be solved, using equations 3.5, 3.6 and 3.7, respectively representing the boom hoist cable angle (γ_{bhc}), the elongation of the boom hoist cable (u_{bhc}) and the static moment equation. Moments here are induced by the weight hanging in the crane, the tension due to the boom hoist cable and lastly the weight of the boom itself.

$$\gamma_{bhc} = \tan^{-1}\left(\frac{\sin(\theta_{bp})L_{cb} - H_c}{\cos(\theta_{bp})L_{cb} + A_c}\right) \tag{3.5}$$

$$u_{bhc} = \sqrt{(\sin(\theta_{bp})L_{cb} - H_c)^2 + (\cos(\theta_{bp})L_{cb} + A_c)^2} - L_{bhc} \tag{3.6}$$

$$\begin{aligned} L_{cb}\cos(\theta_{bp})\left(-\frac{1}{2}m_b g - \sum mg - k_{bhc}u_{bhc}\sin(\gamma_{bhc})\right) + \\ L_{cb}\sin(\theta_{bp})k_{bhc}u_{bhc}\cos(\gamma_{bhc}) = 0 \end{aligned} \tag{3.7}$$

The latter equation is to be solved for θ_b, by using the Newton-Raphson method: a method that uses a function, its derivative, and an initial guess in order to find the roots of a real-valued function [24]. In this case, an initial guess for θ_b (θ_{b-n}) is the starting input in the function described in the static moment equation (equation 3.7, which here is called $f(\theta_{b-n})$). The same initial guess is used as an input in the first derivative of that function: $f'(\theta_{b-n})$. The next iterative value for θ_b, θ_{b-n+1} is then calculated using equation 3.8. The accuracy of the method can be adjusted by tolerating a certain error, represented by $(\theta_{b-n} - \theta_{b-n+1})^2$. If this value is lower than the chosen tolerance of 10^{-20}, the proper root is found.

$$\theta_{b-n+1} = \theta_{b-n} - \frac{f(\theta_{b-n})}{f'(\theta_{b-n})} \tag{3.8}$$

Like in the pre-tension calculation for the load cable, this method arises a numerical error: the moment around the crane boom will never be exactly zero, so the initial θ_b will never be exact either. When no external forces nor initial displacements act on the system, and the load cable is modelled only as an point mass in the crane boom tip, the boom rotation calculated by the model is shown in figure 3.4. The parameters used are based on the stiffnesses, lengths and masses that are used for the actual model (which can be found in appendix A). After a period of $50,000\ s$, the growth of the angle stops, with an asymptote of $4 \cdot 10^{-4}\ rad$. Again, the figure is only shown for the first $100\ s$, for readability reasons.

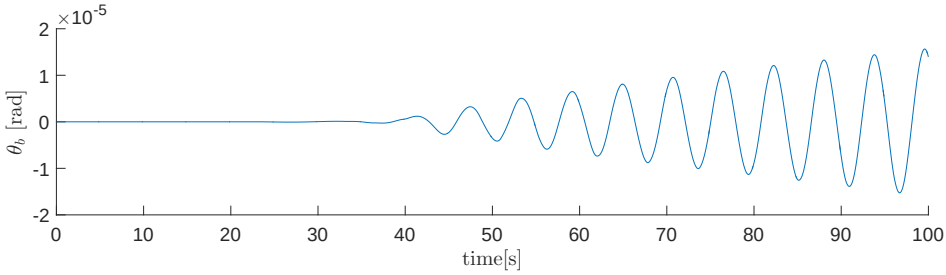

Figure 3.4: Crane boom's rotation

Now, the load cable with its elements can be added to the boom model. The previously used point mass in the crane tip is replaced by the forces in the first load cable element. These forces are calculated using the same method described in 3.1. This time, the displacements of the crane tip, caused by its rotation, are included. The equation of motion for the boom rotation is given in equation 3.9 and its parameters can be found in figure 3.5a. The values chosen for these parameters are given in appendix A and the system's erroneous oscillations due to the numerical errors are discussed in appendix D.

$$J_b\ddot{\theta_b} = -\frac{1}{2}m_b g r_x + F_{bhcx}r_z - F_{bhcz}r_x - F_{lcx,1}r_z - F_{lcz,1}r_x \tag{3.9}$$

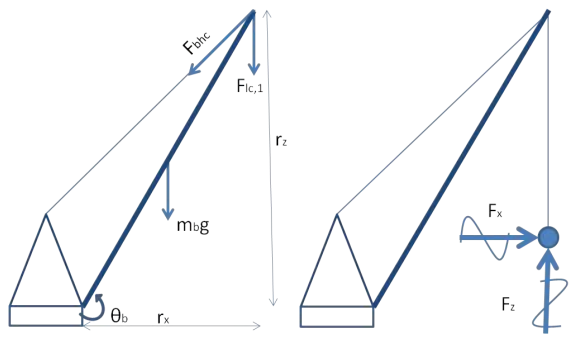

(a) Crane boom dynamics

(b) External forces

Figure 3.5: Crane boom

In order to be able to verify whether the model works so far, external forces as shown in figure 3.5b are applied upon the system. The node-displacements these forces induce are checked on plausibility. The forces are chosen based on expectable behaviour and magnitude: Oscillations are added in order to represent the waves, and magnitudes of amplitudes are chosen to be approximately half of the weight hanging in the load cable (in this case $9.81 \cdot 10^5\ N$). In figure 3.6, results are given for a simulation where a set of 10 load cable elements, a positive-x-directional force of $4 \cdot 10^5 \cos(2t)\ N$, and a positive-z-directional force of $4 \cdot 10^5\ (1 + 0.1\cos(2t))\ N$ (representing a constant and a fluctuating buoyancy force) were used.

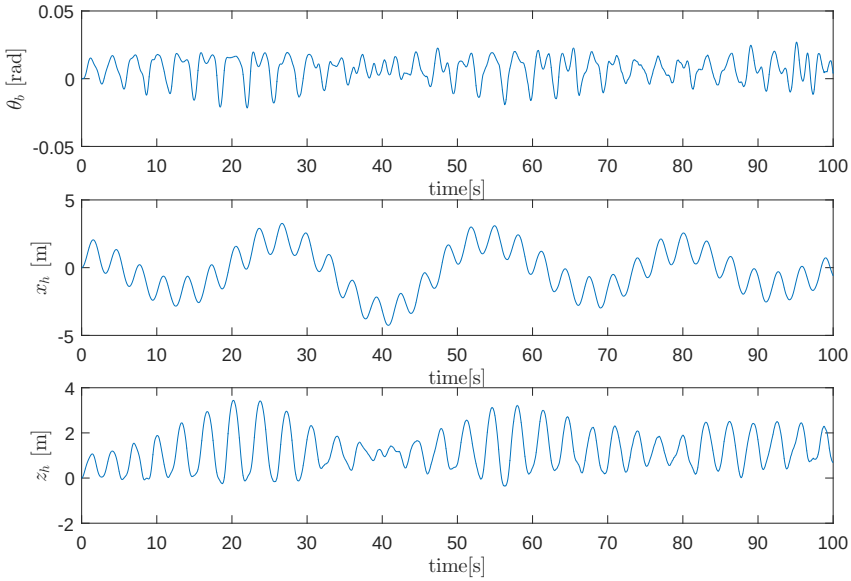

Figure 3.6: Boom's rotation and hook's displacements due to external forces

The displacements seem to oscillate with two periods standing out: a smaller approximate $3\ s$- and a bigger $30\ s$ one. The first can be explained by the external force frequency and the second relies on the stiffness and other parameters of the model. Striking further is that neither the z_h- nor the θ_b displacements oscillate around zero, which is caused by the constant positive z-directional force.

3.3 Slings

The next step is to add an object that is to be lifted by the crane, which will later on be represented by the jacket. As a starting point, this object is modelled as a square, which can translate in x-and z-direction and which can rotate around its centre of gravity (COG). The square is attached to the hook with two identical elastic slings, which are modelled as two, one-element-massless-springs. Their parameters are based on eight-stranded 'G1960 Noble ropes', by Nobles Big-Lift Devision [34]. These slings have a diameter of approximately $184\ mm$, a mass of $105.4\ \frac{kg}{m}$ and a minimum breaking load of $15,070\ kN$. Forces in these slings are calculated using the same method as was explained in section 3.1. The object combined with its slings is shown in figure 3.7a. The circle in the top represents the crane hook, which again is modelled as a point mass.

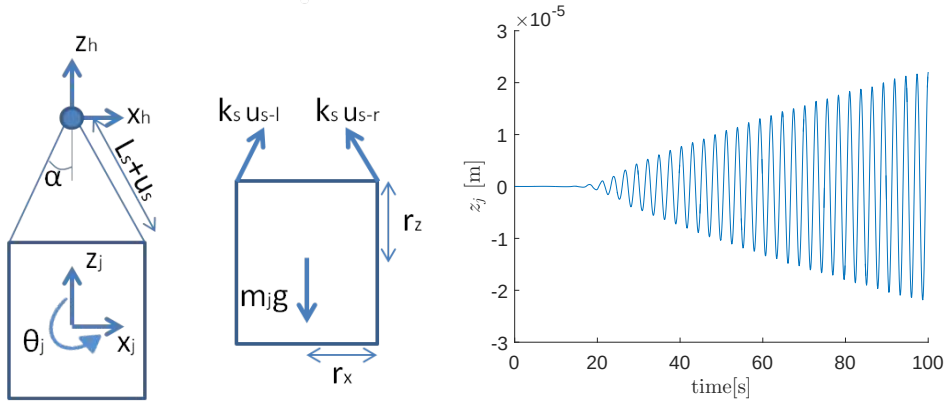

(a) Object coordinates

(b) Object free body diagram

(c) Numerical error in z displacement

Figure 3.7: Representatation of the jacket with its defenitions and displacement

The mass of the object, combined with the elasticity of the slings, induce an initial vertical displacement, which changes the angle in which the slings are positioned. These values can be solved by finding angle α for which the force equilibrium in z-direction accounts. Likewise for the boom pre-tension calculations, the Newton-Raphson method is used for these calculations. The static forces used for these calculations are shown in figure 3.7b and the equations that should be solved for α are listed in equation 3.10. These calculations again induce a numerical error,

resulting in increasing z-directional displacements in, as is shown in figure 3.7c.

$$\begin{aligned} u_s &= -L_s + \frac{r_x}{\sin(\alpha)}; \\ m_j g &= 2k_s u_s \cos(\alpha); \end{aligned} \tag{3.10}$$

When the square and slings are added to the model of the crane boom and load cable, and all pre-tensioned displacements are considered in the initial conditions, the system can be solved dynamically. The dynamic forces acting on the square are shown in figure 3.8a.

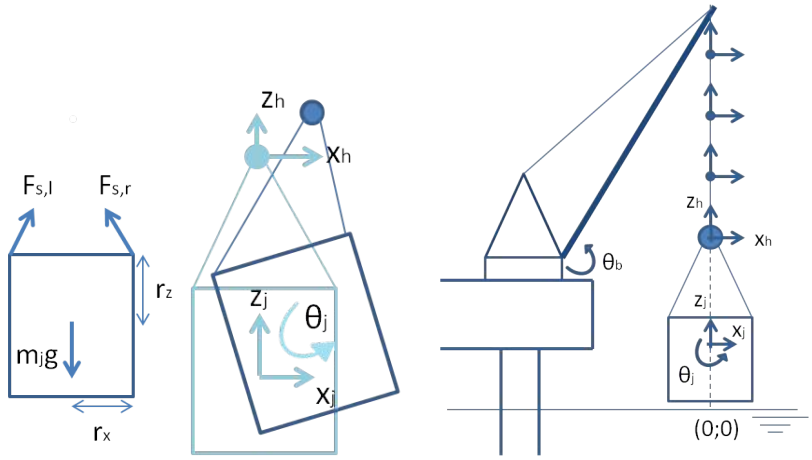

(a) Dynamic forces

(b) Dynamic motions

(c) Degrees of freedom

Figure 3.8: Sling dynamics and system's degrees of freedom

In order to be able to calculate the forces in the slings, its nodal displacements are used. These end nodes are positioned in the upper corners of the square and their displacements can be calculated using the translational and rotational ones of the square's COG [24]. The dynamic displacements that influence the system are shown in figure 3.8b. In equation 3.11 this method is shown for the left sling.

$$\begin{bmatrix} x_L \\ z_L \end{bmatrix} = \begin{bmatrix} x_j \\ z_j \end{bmatrix} + \begin{bmatrix} \cos(\theta_j) & -\sin(\theta_j) \\ \sin(\theta_j) & \cos(\theta_j) \end{bmatrix} \begin{bmatrix} x_{L0} \\ z_{L0} \end{bmatrix} \tag{3.11}$$

The first array represents the translation of the square, and the right matrices represent the displacements due to rotation of the square. x_{L0} and z_{L0} represent

the initial global coordinates of the left upper corner. It is convenient that the the distance between the COG and this corner does not change, due to the rigidity of the object (and later on the jacket). Therefore, these lengths do not change over time and can be used as constants for each time step.

The acquired equations of motions of respectively the hook and square are added to those of the boom and load cable, in form of a force vector. The force vector for the entire model so far, which's degrees of freedom are shown in figure 3.8c, is given in equation 3.12. In order to be clear, the representative degrees of freedom are positioned next to this vector: The first line represents the moment around the crane boom origin, followed by a set of $N-1$ numbers of x-and z-directional forces on the load cable nodes, the x- and z-directional hook forces and lastly the forces on the three degrees of freedom of the object: x- and z-directional forces and rotational moments around its COG. The arms required for the object's moment-calculations constantly change with its rotation. Their magnitudes are described by the multiplication of the rotational matrix with the initial coordinates, which is represented in the right matrice-array multiplication in equation 3.11.

$$\mathbf{F_{rig}} = \begin{bmatrix} -\frac{1}{2}m_b g r_x + F_{bhcx} r_z - F_{bhcz} r_x - F_{lcx,1} r_z - F_{lcz,1} r_x \\ -F_{lcx,1} + F_{lcx,2} \\ F_{lcz,1} - F_{lcz,2} - m_{lc} g \\ \vdots \\ -F_{lcx,(N-1)} + F_{hx} \\ F_{lcz,(N-1)} - F_{hz} - m_{lc} g \\ -F_{hx} - F_{sx,l} + F_{sx,r} \\ F_{hz} - F_{sz,l} - F_{sz,r} - m_h g \\ F_{sx,l} - F_{sx,r} \\ F_{sz,l} + F_{sz,r} - m_j g \\ -F_{sx,l} r_{z,l} + F_{sx,r} r_{z,r} - F_{sz,l} r_{x,l} + F_{sz,r} r_{x,r} \end{bmatrix} \begin{bmatrix} \theta_b \\ x_{lc,1} \\ z_{lc,1} \\ \vdots \\ x_{lc,(N-1)} \\ z_{lc,(N-1)} \\ x_h \\ z_h \\ x_j \\ z_j \\ \theta_j \end{bmatrix} \tag{3.12}$$

The dynamics of the system can be solved by solving $\ddot{\mathbf{x}} = \mathbf{M^{-1}F_{rig}}(\mathbf{x})$. The degrees of freedom of the system ($\mathbf{x}$) are shown in figure 3.8c and are represented by the right array in equation 3.11. It should be noted that the origin of the global coordinate system is positioned at MSL, right underneath the crane tip in rest (without considering pre-tensioned initial displacements). This is done due to its convenience in numerical calculations of the wave forces in the next stage. The system's erroneous displacements due to the numerical errors are discussed in appendix D.

The model is created such that the slings can be subdivided into multiple elements, by discretizing them into N nodes, each representing a lumped mass and

each being held in position by the sling elements, modelled as springs. Forces in these elements are determined using the same method as was used for the load cable: initial conditions are calculated via pre-tension calculations and relative distances between nodes is used in order to calculate tensioned lengths and thus forces. Likewise for the load cable elements, drawing conclusions on the amount of sling elements in this phase of the model is not possible yet: all forces are to be added to the system first. Since the slings only deform in longitudinal direction and are supposed to be in tension throughout the installation, it would seem logical that one sling element will be sufficient (when no slack line occurs). A study herein is performed in section 4.7.

3.4 Lowering crane

In the end, the jacket should be lowered towards the seabed, using the crane. This lowering procedure is modelled by enlarging the load cable with $v_c t$ (v_c being the lowering speed). This does cause some changes in the model: with an increasing load cable length, both the mass and stiffness of the cable increase accordingly. Therefore, the mass that hangs in the crane boom increases, which causes it to slightly tilt over.

For each time step, the change in length of the load cable, together with its effects on the other parameters, is used as an input in the force calculations: elongations of the load cable elements are calculated using the new stiffness, masses, and lengths and the element masses are constantly changed within the mass matrix.

The lowering of the crane further causes the global coordinates of the elements to constantly shift. These coordinates are required jacket elements' submergence determination.

Lastly, the lowering velocity of the crane should be considered in the total vertical velocity of the crane elements, which is a parameter that is required in calculations of several forces.

The increasing size of the load cable elements introduce minor errors in the descretization, due to the fact that the element length now depends on time. When the equations of motion are derived using the Lagrangian method, the kinetic energy is to be differentiated with respect to time. Time dependent parameters therefore introduce new terms in the equation of motion. For this research however, the errors are considered to be negligible, since only $50\ m$ of height difference is to be overcome.

3.5 Jacket geometry

The last step is to implement the jacket's geometry in the model. The square object that was used up until now is replaced by the jacket, using its geometry combined with its mass and inertia. The parameters used for this modelling are provided by Siemens and given in appendix A.

The element- and node-coordinates of this complex geometry are to be constantly monitored, since the forces that act on the structure depend on submerged volumes and relative displacements,- velocities, and- accelerations. By monitoring the translation and rotation of the jacket's COG, combined with its rigid distance to the point of interest, the coordinate global locations, displacements, velocities, and accelerations can be calculated, by using translational of- and angular velocities around the jacket's COG [24]. For velocity and acceleration respectively the formulas are given in equations 3.13 and 3.14. The arms r_x and r_z depend on θ_j, and are represented by the right matrix-array multiplication in equation 3.11.

$$\begin{bmatrix} v_x \\ v_z \end{bmatrix} = \begin{bmatrix} \dot{x}_j \\ \dot{z}_j \end{bmatrix} + \begin{bmatrix} 0 & -\dot{\theta}_j \\ \dot{\theta}_j & 0 \end{bmatrix} \begin{bmatrix} r_x(\theta_j) \\ r_z(\theta_j) \end{bmatrix} \tag{3.13}$$

$$\begin{bmatrix} a_x \\ a_z \end{bmatrix} = \begin{bmatrix} \ddot{x}_j \\ \ddot{z}_j \end{bmatrix} + \begin{bmatrix} 0 & -\ddot{\theta}_j \\ \ddot{\theta}_j & 0 \end{bmatrix} \begin{bmatrix} r_x(\theta_j) \\ r_z(\theta_j) \end{bmatrix} + \begin{bmatrix} 0 & -\dot{\theta}_j \\ \dot{\theta}_j & 0 \end{bmatrix} \begin{bmatrix} 0 & -\dot{\theta}_j \\ \dot{\theta}_j & 0 \end{bmatrix} \begin{bmatrix} r_x(\theta_j) \\ r_z(\theta_j) \end{bmatrix} \tag{3.14}$$

3.6 System behaviour

Having modelled the entire system, it is interesting to see what the vertical behaviour of the jacket is, when it is given an initial upward vertical displacement of $0.1\ m$. Figure 3.9 shows this reaction, in case the jacket is held in position with $70\ m$ of load cable length (the blue line in the upper figure) and in case the jacket is lowered with a velocity of $0.5\ \frac{m}{s}$, from 70 to $110\ m$ load cable length (lower figure). From these figures, the eigen-period of the rigging system as it is modelled can easily be found. This eigen-period is formed by the combination of the inertia of the crane boom and the set of elasticities of the crane boom hoist cable, the load cable and the slings. For the jacket that hangs still, the period is approximately $2.5\ s$. In case the jacket is lowered though, the period slowly increases from 2.5 to $2.7\ s$. This can be explained by the decreasing load cable stiffness, due to its increasing length. In order to visualise this small difference, in the red line in the upper figure the oscillation of a simulation with a load cable length of $100\ m$ is added.

In the lower figure further, z_j does not oscillate around zero, but its mean value decreases over time. This can be explained by the tilting behaviour of the crane boom, caused by the increasing mass that is hanging in it, as a result of the increasing length of the cable.

When the jacket is influenced by forces in the same range as the rigging's eigen-period, resonance could occur, causing large displacements and forces. Special care should therefore be taken in conditions where the wave periods are within this range. This later on will be enlightened in the analysis.

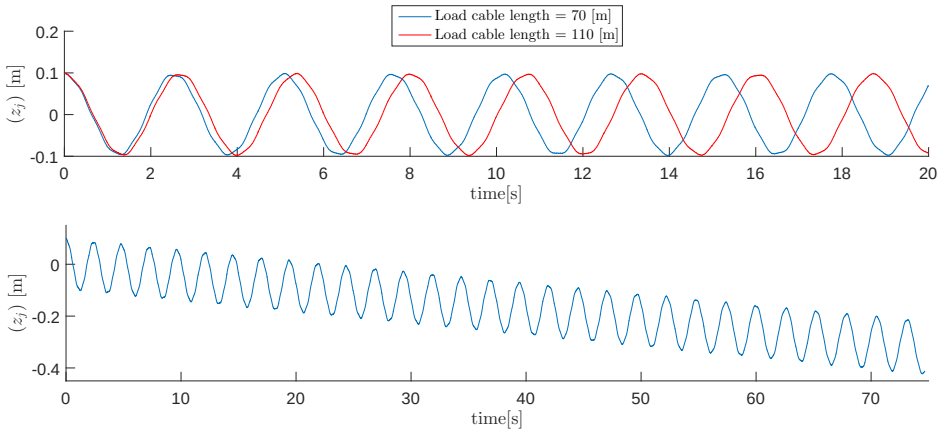

Figure 3.9: z-displacement jacket's COG, with an initial displacement of $+0.1\ m$

The next step is to add the environmental conditions with the forces and influences involved to the model, so displacements and load cable forces can be studied. These results can be used in order to find out whether, for those particular wave conditions, the criteria sketched in section 2.3 are satisfied. In order to test the behaviour of the system upon external forces, a sinusoidal horizontal force, and a constant-, and co-sinusoidal vertical force are introduced to the jacket's COG. Both are given a magnitude of $\frac{1}{3}^{rd}$ of the jacket's mass and a period of $10\ s$. The reactions in terms of displacements of the degrees of freedom of the crane boom, hook, and jacket's COG, which is lowered with a downward velocity of $0.5\ \frac{m}{s}$ are shown in figure 3.10.

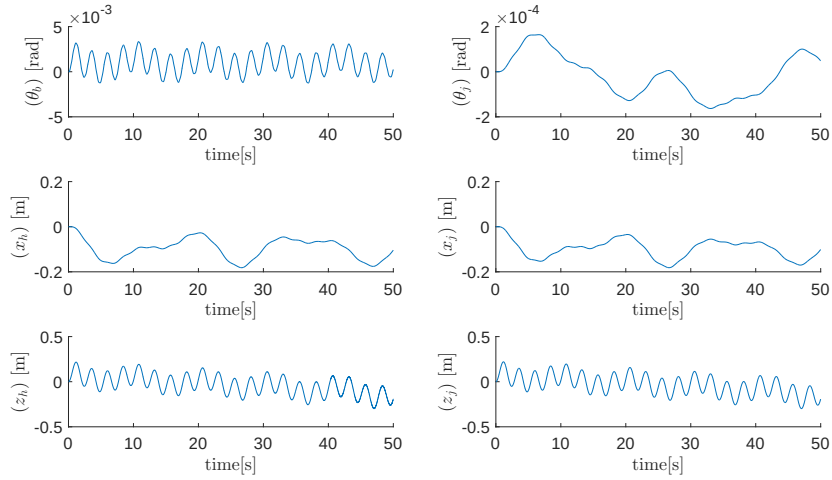

Figure 3.10: System's displacements as a reaction on external forces on jacket's COG

In the z-displacement of the jacket's COG, which is represented by z_j in the bottom right graph, two oscillating periods are observed. The smallest period corresponds to that found earlier in this section: the eigen-period of the rigging. The larger period corresponds with the period of the z-directional force that acts upon the system. In the x-direction, the oscillation is not smoothly sinusoidal, which is caused by the additional x-displacement the jacket and hook have as a result of the tilting of the boom. The period of the horizontal force however can still be recognized here.

In order to check whether the system satisfies the criteria, the load cable force F_{lc} in equation 2.9 is calculated by multiplying the cable stiffness with its stretched length. This length can be determined by monitoring the global coordinates of both the crane tip and the hook. The reactional force in the load cable is shown in figure 3.11. Comparing this behaviour with the displacements in figure 3.10, the resemblance with the z-directional displacements can clearly be found. The assumption made in section 2.1, that the load cable force primarily is induced by vertical motion is thus correct.

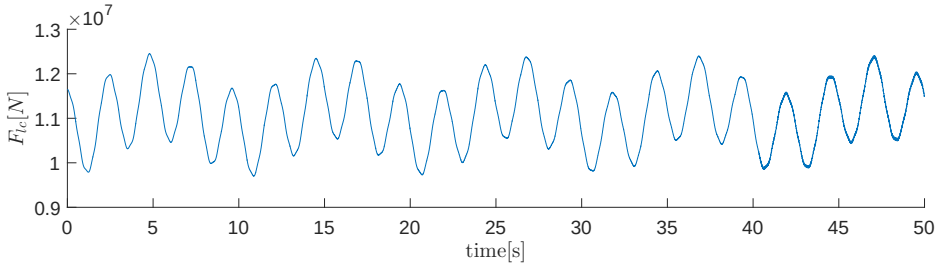

Figure 3.11: Load cable force as a reaction on external forces on jacket's COG

As an extra test, another set of external forces is added to the system. This time, the period of these forces is adjusted to that of the eigen-period of the rigging. As a result, in figure 3.12 and 3.13 respectively the displacements and load cable forces are plotted. As expected, the system shows resonance behaviour: the amplitude of the z- displacements and load cable force rapidly increase in amplitude. Another striking observation is that the jacket seems to drift off in x-direction.

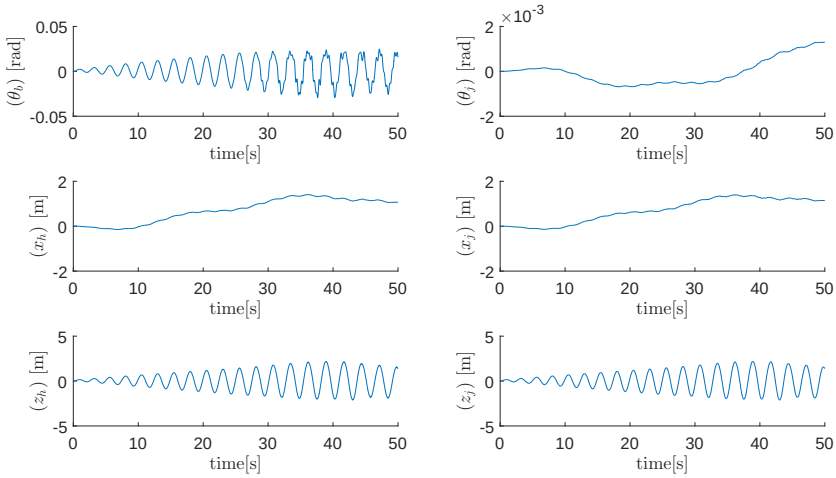

Figure 3.12: System's displacements as a reaction on external forces on jacket's COG, with a period in range of the system's eigen-period

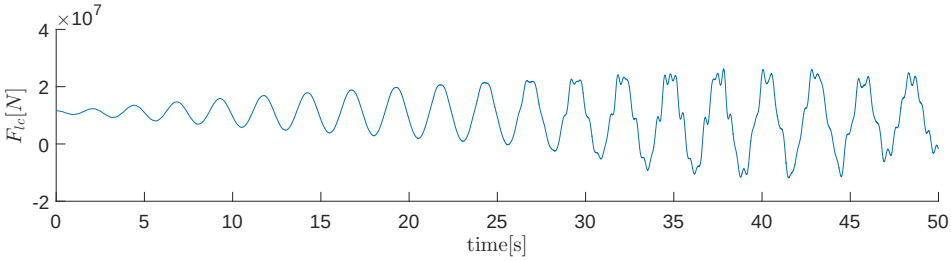

Figure 3.13: Load cable force as a reaction on external forces on jacket's COG, with a period in range of the system's eigen-period

In order to translate these results in terms of the criteria sketched, in the upper figure of figure 3.14 the static- versus the dynamic load cable lengths are shown, as is the the DAF of the load cable in the bottom figure. In the latter, the black line indicates the maximum allowable DAF of 1.3. As expected, the resonating behaviour encourages the criteria to be transgressed. In between the 25^{th} and 26^{th} second, the dynamically stretched cable length is shorter than that in the statical case, which indicates that slack occurs. The effect this has upon the system immediately can be observed: the beforehand smooth line now becomes non-smooth and reaches higher amplitudes. This once again shows that slack should at all times be avoided.

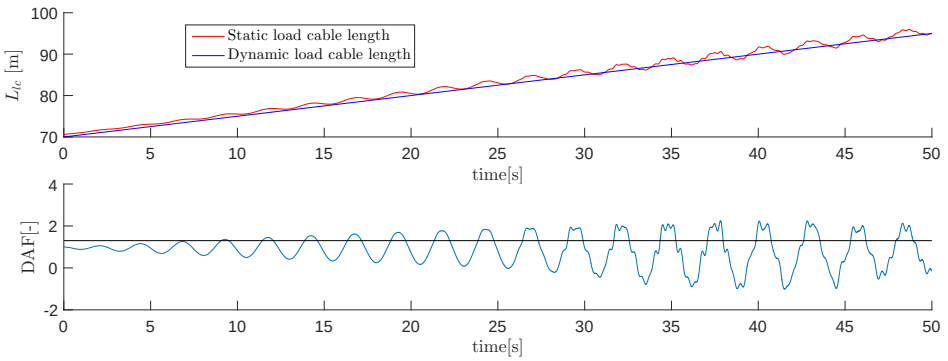

Figure 3.14: Load cable lengths and DAF, as a result on external forces

3.7 MATLAB model summary

In this chapter the design of the crane and its rigging in a MATLAB model is discussed. The biggest assumptions made herein are that the complete model is represented in 2D and that both the crane boom and the jacket are considered to be rigid.

The total set of degrees of freedom is described, containing the rotation of the crane boom θ_b, the x- and z displacements of the discretized load cable elements, that of the hook: x_h and z_h, the discretized sling elements, and lastly the translational and rotational behaviour of the jacket structure: x_j, z_j and θ_j. During the set up of this entire system, it has been shown that pre-tensioned initial conditions cause negligibly small numerical errors in the outcomes. These errors were found back once the entire system was modelled as one, as is shown in appendix D. /bigskip

Lastly, the interaction between the rigging elements was tested, both by giving the jacket an initial condition and by letting external forces act upon it. Via these studies respectively the eigen-period of the system is found and the behaviour and interactions between the DOFs are verified on plausibility.

Chapter 4

Forcing

Now the crane model is designed and tested, the environmental forces that act upon the jacket can be determined. In this chapter a description of the forces incorporated are given. It is important to keep in mind that it is not the goal of this research to perfectly model the interaction between the jacket and the oceanic environment, but to get a good and realistic estimation of the jacket's behaviour in common environmental conditions: some assumptions and modelling choices are made in order to simplify the model and reduce computational time.

Firstly, in section 4.1 the horizontal forces due to waves are explained, including the determination of hydrodynamic coefficients and equivalent diameters. Then, in section 4.2, the vertical forces caused by buoyancy are treated, followed by those caused by the vertical wave kinematics in section 4.3. Section 4.4 describes the difficulties in the splash zone transition, including bucket trapped air pressures and slamming phenomena. Then the inertial influences by added mass are discussed in section 4.5, followed by the interaction the buckets have when they reach close proximity of the seabed, in section 4.6. Lastly, in section 4.7 some important remaining parameters are discussed and chosen.

Within this chapter further choices are made regarding the consideration of taking additional forces and influences into account. Several of these phenomena are not considered in the model; the reason why this is done will be explained more elaborately in chapter 6.

4.1 Horizontal wave forces

The horizontal wave forces on submerged jacket elements can be calculated using the wave kinematics as were discussed in section 2.2, by using the Morison's equation. According to Journée [25], this is a semi-empirical equation for the in-line forces on a body in oscillatory flow (waves), assuming that the flow acceleration is more or less uniform at the location of the body. It is a horizontal wave force approximation, consisting of a drag- and inertia term. In equation 4.1, the Morison force per unit length is given for a cylindrical structure, considering relative velocity and acceleration between the waves (u_i and $\dot{u}_i$ respectively) and the structure itself (x_i and $\dot{x}_i$ respectively).

$$F_{mi} = \frac{1}{4}\pi D_a^2 \rho_w \dot{u}_i + \frac{1}{4}\pi D_a^2 \rho_w C_a(\dot{u}_i - \ddot{x}_i) + \frac{1}{2} D_d C_d \rho_w |u_i - \dot{x}_i|(u_i - \dot{x}_i) \qquad (4.1)$$

A limitation in Morison's equation, in case of a vertical cylinder in waves, is that it requires the diameter of the cylinder to be much smaller than the wavelength. If it is small enough, diffraction effects have to be taken into account. In practice, the ratio diameter to wavelength is acceptable for $D < \frac{\lambda}{5}$. For larger diameters, the structure will influence the patterns in the waves themselves and outcomes are not totally correct. In terms of the jacket used for this research, all legs- and braces will definitely satisfy this ratio. The buckets however have a too large diameter, causing this condition not to be true for all wave components. Despite that however, Morison here will be used for force calculations for the buckets as well, since it is considered to give a good (according to Iyalla in 2012 [22] conservative) approximation of reality. In addition, it is known that the forces in horizontal direction are of less importance for the criteria which are studied. In the discussion, section 6.3.2, the influence diffraction would have on the system is briefly studied.

In the following subsections a stepwise method is given explaining all parameters in Morison's equation, given in equation 4.1.

4.1.1 Equivalent jacket diameters

Firstly, the jacket consist out of four legs and a set of both horizontal and diagonal braces. In theory, Morison's equation can be performed for each of these members individually. Since this would introduce a large amount of computational time though, this part of the jacket is written in terms of equivalent horizontal diameters, aligned in the jacket's centre. The stick model is used, which is a method that uses vertically

subdivided jacket compartments, each having its own equivalent diameter. These diameters are determined by calculating the summation of all components within that particular vertical compartment, factored by individual member diameters and the angle in which they are positioned. A downside herein is that it results in the members being placed at the centre of the structure, neglecting effects of spatial separation. According to Vugts in 2002 [45] however, this assumption results in a more conservative load estimation.

A representation of the equivalent diameters, determined using the stick model, is given in figure 4.1. The method used is based on a manual by Dubbers in 2004 [13] and is described in appendix E, together with its outcomes.

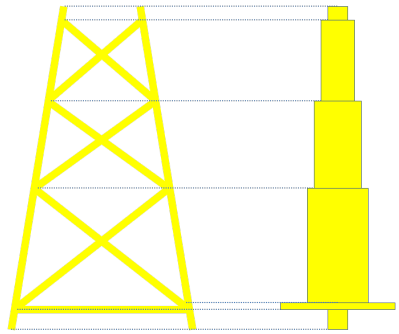

Figure 4.1: Equivalent jacket diameters in the stick model

4.1.2 Wave kinematics

The next step is to calculate the wave kinematics for each submerged component. As was discussed in section 2.2.1, the wave particle velocity and acceleration of an irregular wave depend on the wave elevations of each individual wave component. In order to be able to calculate these elevations, an x-coordinate should be provided as an input. For each jacket component (the buckets are considered individually and for the legs and braces the equivalent diameters are used), the representative x-coordinate used for these calculations is considered to be that in the middle of the submerged part of the component's centreline, as can be seen in figure 4.2a. The determination of the location of this coordinate is provided in appendix F.

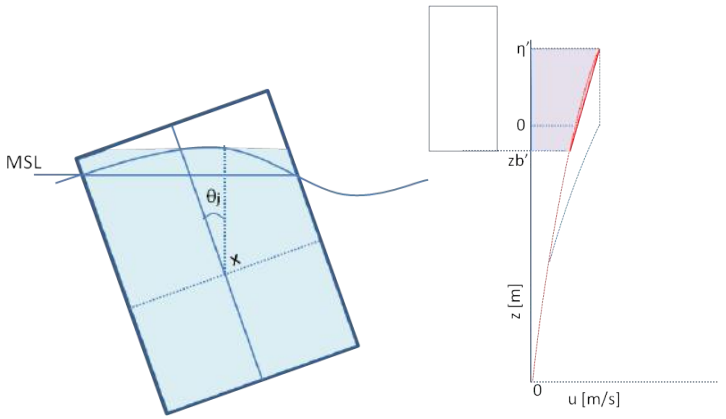

(a) Element submergence level **(b)** Horizontal velocity profile

Figure 4.2: Submergence elevations

Knowing the representative x-coordinates for the submerged elements, wave elevation η can be calculated for each location at each time instant. This is done by using equation 2.2, which was given in section 2.2. This η, at the representative x-coordinate, is considered to be the wave elevation for that entire component.

As an input in Morison's equation the kinematics at each submerged elevation should be calculated via the wave kinematics given in equation 2.7. Due to the fact that this will be time consuming in computations, a simplified method is used here. The profile is considered to vary linearly between the top- and bottom elevation, as is visualised in figure 4.2b. Therefore, only the kinematics at these two elevations are to be calculated. As was explained in section 2.2.2, the horizontal velocity follows the Wheeler stretch over height. Therefore, the top and bottom elevations should be rewritten to their transformed Wheeler elevations, by using equation 4.2 [25].

$$z' = \frac{d}{d+\eta} z + d\left(\frac{d}{d+\eta} - 1\right) \tag{4.2}$$

4.1.3 Morison coefficients

Both the drag- and inertia related forces in Morison's equation contain certain coefficients, respectively C_d and C_a. The former coefficient is a dimensionless quantity used to quantify the drag or resistance, and the latter quantifies the inertial part of Morison's equation.

As can be seen in equation 4.1, the inertia part consist out of two terms: one with- and one without a coefficient. This is due to the fact that the inertia coefficient C_m actually is defined as $1+C_a$, where only C_a, the added mass coefficient, describes the interaction between the movement of the structure and water. The other force describes the so called FroudeKrylov force, which is introduced by the unsteady pressure field, generated by undisturbed waves. Therefore, only the second term shows a dependency on the structure's acceleration.

The derivation of both coefficients is given in appendix G.

4.1.4 Forcing

The inertial force depends on the relative acceleration between the jacket and the water particles. The latter is known, but the former is not, since the acceleration is not a generated output in MATLAB's ODE45 solver. Due to the fact that the acceleration for each time step can not be gained via the solver itself, Morison's equation should be rewritten in terms of a generalized, structure's acceleration independent, force.

Firstly, the acceleration of a jacket component depends on both translational and rotational accelerations of the COG, as was explained before, in equation 3.14. The generalized force should therefore be calculated using both the translational and rotational part. $\ddot{x}_i$ In Morison's equation should thus be replaced by this acceleration, which is given in equation 4.3.

$$\ddot{x}_i = \ddot{x}_j - \ddot{\theta}_j r_{zi} - \dot{\theta}_j^2 r_{xi} \tag{4.3}$$

Equation 4.4 shows the two equations of motion that are to be solved in order to acquire $\ddot{x}_j$ and $\ddot{\theta}_j$. When solved, these values can be used in equation 4.3 and subsequently in Morison's equation.

$$m_j \ddot{x}_i = F_{mi}(\ddot{x}_j, \ddot{\theta}_j) \tag{4.4a}$$

$$J_j \ddot{\theta}_i = r_{zi} F_{mi}(\ddot{x}_j, \ddot{\theta}_j) \tag{4.4b}$$

The result of the generalised Morison's equation is given in equation 4.5. As can be seen it now is written in all known terms.

$$F_{mi} = \frac{J_j m_j \rho_w (\pi D_{ai}^2 \dot{u}_i (1 + C_{ai}) + 2 C_{di} D_{di} (u_i - \dot{x}_j) |u_i - \dot{x}_j| + \pi C_{ai} D_{ai}^2 r_{xi} \dot{\theta}_j^2)}{-C_{ai} m_j \rho_w \pi D_{ai}^2 r_{zi}^2 + C_{ai} J_j \rho_w \pi D_{ai}^2 + 4 J_j m_j} \tag{4.5}$$

By solving the acquired equation, a force per unit length is calculated. Via the equations given in equations 4.6a to 4.6d, this force can be written in terms of a horizontal resultant wave force and moment around the jacket COG. These equations are based on the assumption of linear profiling between the upper- and lower submerged elevation, and are visualised in figure 4.3. z_1 And z_2 respectively describe the arms between the jacket's COG and the resultant force of the linear part F_{r1} and the constant part F_{r2}. Notice that the elevations indicated with an apostrophe indicate those rewritten into Wheeler elevations.

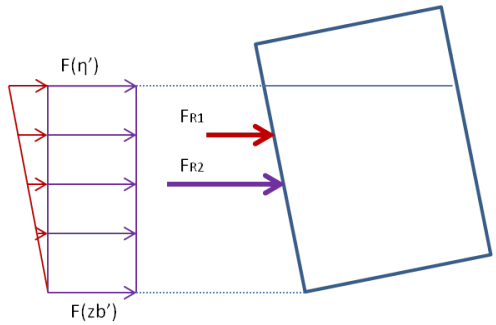

Figure 4.3: Horizontal wave profile- and resultant forces

$$z_1 = z_b + \frac{2}{3}(\eta - z_b) \tag{4.6a}$$

$$z_2 = z_b + \frac{1}{2}(\eta - z_b) \tag{4.6b}$$

$$F_{r1} = \frac{1}{2}(\eta - z_b)(F(\eta') - F(z_b')) \tag{4.6c}$$

$$F_{r2} = (\eta - z_b) F(z_b') \tag{4.6d}$$

A short summation of the horizontal wave force calculation for an individual jacket element is shown in figure 4.4. Starting with the irregular wave pattern at the left, the wave elevation is calculated for a representative x-coordinate. The upper and lower submerged component elevation are calculated an rewritten to Wheeler elevations. For both elevations, the wave kinematics are calculated and implemented in the generalized Morison's equation, in order to calculate the force per unit length. By assuming linear variation between both elevations, the resultant forces and moments are calculated, which are shown in the right of figure 4.4. These steps are to be repeated for each submerged jacket component and lastly, the summation of these resultants is to be implemented into the equations of motion of the jacket.

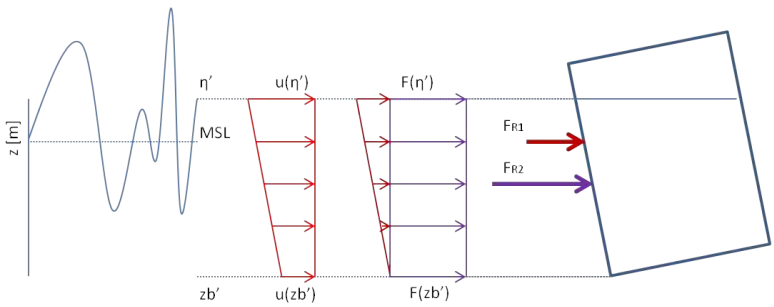

Figure 4.4: Summation of the horizontal wave force calculations

By considering 2D, only two in stead of four buckets are used for force calculations. Since the wave pattern is assumed to be uni-directional, the force upon the two other buckets will be of the same magnitude as those calculated, so the buckets' Morison's forces can simply be considered twice.

Further, according to Barlas in 2012 [1], the shielding effect should be considered: once the waves have passed the first buckets in line, the wave elevation and kinematics will be somewhat reduced, due to the interaction between bucket and water. This results in lower forces upon the second buckets in line. According to a simplified method described by DNV [8] this phenomena can be incorporated by calculating the reduced horizontal velocity at the second bucket in line using equation 4.7. Here, $\dot{x}_0$ is the velocity in case no shielding is considered and x and y represent the coordinates of interest. Since uni-directional waves are considered, y is zero and the exponent in the equation is cancelled.

$$\dot{x} = \dot{x}_0 \left(1 - \sqrt{\frac{C_d D}{x + \frac{4D}{C_d}}}\right) \exp -0.693 \left(\frac{y}{0.25\sqrt{C_d D(x + \frac{4D}{C_d})}}\right)^2 \tag{4.7}$$

4.1.5 Current forces

The forces induced by current are calculated by inserting the current kinematics into Morison's equation. These kinematics depend on the submergence of the elements, since current velocity has a certain profile over the water depth. DNV [8] states that this profile can be approximated by equation 4.8. The current velocity at the surface ($v_{current,0}$), is based on the mean surface current velocity measured at an offshore wind farm in the North sea, with a magnitude of $0.5\ \frac{m}{s}$, as is found by Wagenaar in 2010 [46]. Further, z_i indicates the distance to the still water level (negative downwards) and d the water depth (positive). In order to reduce calculation steps, the velocities of the currents per submergence are added to those of the waves, prior to Morison's calculations. Due to the constant velocity per elevation, the acceleration terms of the current are zero. Therefore, only drag-related forces will be induced by the current.

$$v_{current} = v_{current,0} \left(\frac{z_i + d}{d}\right)^{\frac{1}{7}} \tag{4.8}$$

In figure 4.5, the displacements of the jacket's COG are plotted in case the horizontal wave forces are exerted upon the structure. In the upper plot the jacket is held at $35\ m$ submergence and the lowering velocity of the crane is set to zero. The difference between x_j with current, indicated in blue, versus that without current in red can clearly be seen: the current induces an offset of approximately $2\ m$. The waves induce an irregularly oscillating movement around this offset.

In the bottom figure the same study is performed, with the jacket $15\ m$ submerged, resulting in the buckets to be within closer range of the waves. Amplitudes in this case reach higher values than were previously observed. The difference in the effect of the current between these two cases is not that clear though; even though the buckets are in higher current velocity regions (equation 4.8), less jacket elements are submerged.

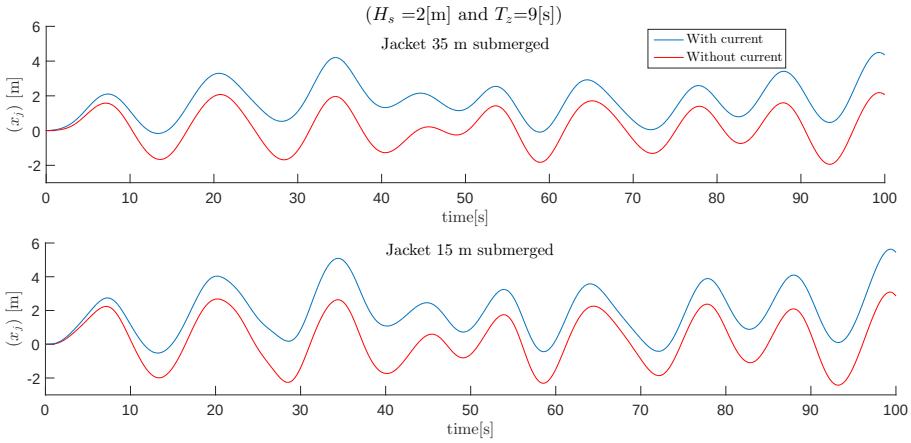

Figure 4.5: x-displacement jacket COG due to horizontal wave forces (with and without current)

4.2 Buoyancy

Buoyancy forces are introduced once elements are submerged, and are calculated by multiplying the submerged volume (V_{sub}) with the gravitational acceleration (g) and the density of water (ρ_w). In order to find V_{sub}, the jacket is subdivided in elevation ranges, for which the horizontal areas are approximately the same. These elevations are taken equal to the stick-model and respectively contain the areas described by the horizontal shells of the buckets, the top of the buckets, the jacket legs, the horizontal braces and the diagonal braces. As an example, the first and latter of these horizontal areas are given figure 4.6a.

Per elevation range, V_{sub} is calculated by multiplying the acquired horizontal areas with the associated submerged level, which is determined using the upper- and lower submerged z-coordinates. As can be seen in figure 4.6b, the difference in submergence over the horizontal plane is not considered in the area calculation, since the submergence level over the entire width is considered to be equal. Additional tilting moments are therefore not incorporated in the model. The moments induced by the actual rotation of the jacket on the other hand are taken into account. Once the jacket is tilted around its COG, buoyancy arms and thus moments occur. Due to symmetry of the jacket, these arms are found by the difference between the center coordinate of each elevation level and that of the jacket's COG.

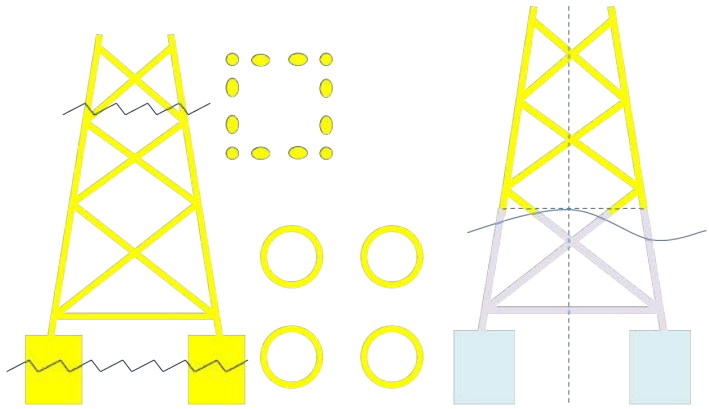

(a) Horizontal buoyancy areas **(b)** Submergence

Figure 4.6: Submerged volume determination

In figure 4.7, the forces in the load cable, as well as the z-displacements of the jacket's COG are plotted, in case the jacket is held still at full submergence and merely the buoyancy forces are switched on in the solver. The buoyancy pushes the jacket up until it oscillates around approximately $0.6\ m$, in the rigging's eigen-period found in section 3.6. The force in the load cable shows that the buoyancy force oscillates around a force of approximately $4.1 \cdot 10^6\ N$. In order to validate whether this value is plausible, it can be used to reversely calculate V_{sub}. The outcome is that the jacket is submerged with a volume of $410\ m^3$. Looking at the jacket volume for this submergence the actual volume indeed is close to this value.

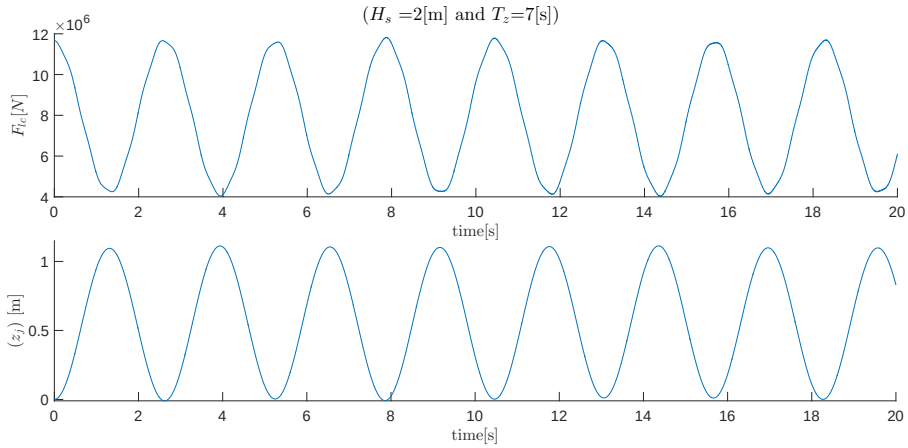

Figure 4.7: Load cable force and jacket's COG z-displacement, caused by buoyancy

4.3 Vertical wave forces

Likewise for the horizontal wave forces discussed in section 4.1, the water particle movements in vertical direction cause forces upon the jacket. These forces too are subdivided in a drag- and inertial term, respectively F_{vd} and F_{vi}:

$$F_v = F_{vd} + F_{vi} \tag{4.9}$$

The drag term, given in equation 4.10, is proportional to the vertical velocity of water particles (w) and that of the member itself ($\dot{z}_i$). The vertical wave particle velocity is calculated for each wave train individually, using the method described in section 2.2.1. The vertical velocity of the jacket member once again can be written in terms of the crane lowering velocity and the translational- and rotational velocity of the jacket's COG, using equation 3.13.

$$F_{vd} = \frac{1}{2}\rho_w C_d A_p \left|w - \dot{z}_i\right| (w - \dot{z}_i) \tag{4.10}$$

A_p In this formula describes the projected area normal to the motion and the drag coefficient C_d we have seen before, in section 4.1.3. Once again, it depends on R_e, k_s and K_c, as has been explained in equations G.1 to G.6 in appendix G. Obviously, this time vertical- in stead of horizontal parameters are to be used. Important here

is that, since equivalent diameters are not used here, the angles of the diagonal braces should be taken into account. According to guidelines in DNV [8], the drag coefficient of a member with an angle β_b with the direction of the flow should be calculated by multiplying the coefficient of a member perpendicular to the flow with the cosines of β_b to the power three:

$$C_{d-angle} = C_{d-perp} \cos^3(\beta_b) \tag{4.11}$$

The second term in equation 4.9 is called the vertical wave excitation force and is the inertial force that the waves excite upon the structure, in case the structure itself would not move. It is therefore calculated by multiplying the submerged mass plus added mass with the vertical wave particle accelerations:

$$F_{vi} = \rho_w V_{sub}(1 + C_a)\dot{w} \tag{4.12}$$

The added mass coefficient C_a once again depends on the steady value of C_d and K_c, as was explained in equation G.7 and appendix G. Likewise for the drag coefficient, the angles in which the diagonal members positioned decrease the added mass. The values found for perpendicular motions should in this case be multiplied with the squared cosines of the angle β_b:

$$C_{a-angle} = C_{a-perp} \cos^2(\beta_b) \tag{4.13}$$

For V_{sub}, the same submergence levels are used as those calculated in the previous sections. The wave elevation is considered to be equal over the entire width of the submerged part of the jacket and is calculated with the global x-coordinate of the middle of the jacket, as can be seen in figure 4.8.

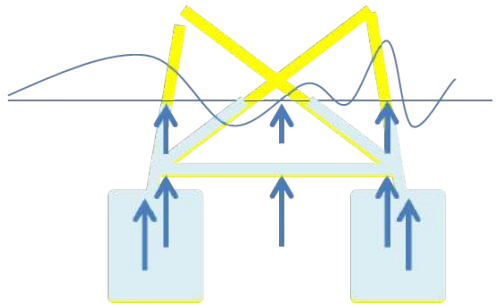

Figure 4.8: Submergence and vertical wave forces

Since unidirectional waves are considered, the jacket members pointing in y-direction feel the same wave accelerations over their entire length. The members in the x-direction however do not. In order to be accurate therefore, the forces over these members should be integrated over their length. However, due to the fact that this will introduce quite some computational time, three points per submerged elevation are considered, as can be seen in figure 4.8. The arrows represent the vertical wave forces upon the buckets, horizontal braces and partially submerged diagonal braces. For these three points, the vertical wave velocities and accelerations are calculated.

It is further assumed that the forces upon the members in y-direction have a bigger influence upon the system than those 'lumped' in the middle. Their contribution on the total vertical forces in that plane will therefore be somewhat over $\frac{1}{4}$ (which is its amount of volume per horizontal level: e.g. per elevation there are 8 diagonal braces, 2 of which point in y-direction on both the left and right side of the jacket). The vertical wave excitation forces therefore are multiplied with $\frac{3}{8}$, $\frac{2}{8}$ and $\frac{3}{8}$ for the left, mid and right respectively. For the diagonal members in figure 4.8 for instance, the total vertical excitation force is calculated by equation 4.14. This division is only used for the inertia term since for the drag term it is automatically included in the determination of the areas normal to the flow.

$$F_{vi} = \frac{3}{8}\rho_w V_{sub}(1 + C_a)(\dot{w}_{left} + \dot{w}_{right}) + \frac{2}{8}\rho_w V_{sub}(1 + C_a)\dot{w}_{mid} \tag{4.14}$$

Since the legs of the jacket are almost in line with the flow, its drag- and added mass coefficient are nearly zero. In addition, physically a large wake in vertical flow will be formed by the bucket tops. Therefore, vertical wave force calculations are not performed on the jacket legs.

In figure 4.9, the force in the load cable as well as the z-displacements of the jacket's COG are shown, in case the jacket would be held still at either 15 or 35 m submergence (respectively in blue and red) and merely the vertical wave forces are switched on in the solver. The jacket oscillates around zero in an irregular fashion, and for the 35 m submergence the vertical wave forces have a considerably smaller effect than the 15 m submergence case. This can be declared by the fact that in the later case the bucket top and horizontal braces are within range of the wave kinematics. These elements create a larger area for the vertical wave forces to act upon than in the more submerged case, where the diagonal braces are in the wave area.

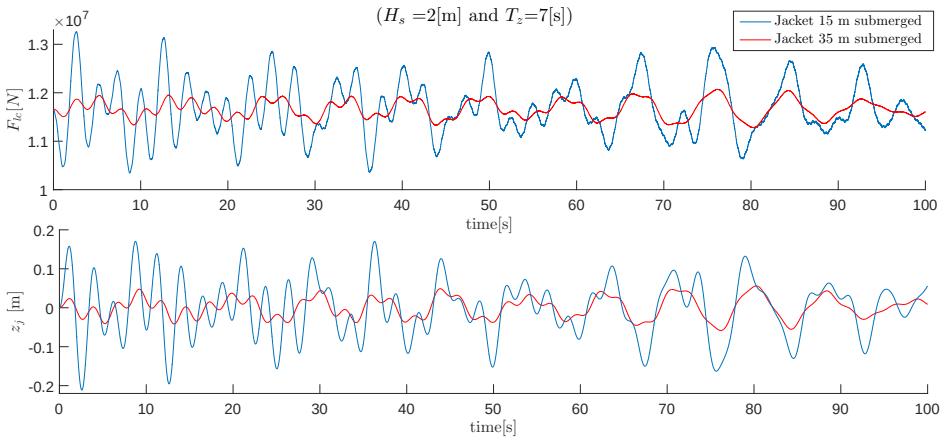

Figure 4.9: Load cable force and z-displacement, caused by vertical wave forces

4.4 Splash zone

The most complex stage in the installation of the jacket is that where the buckets cut through the waterline. Two highly non-linear and hard to predict phenomena occur: the formation of an air cushion within the buckets and slamming against the buckets' top. The process of lowering a suction bucket through the splash zone can thus be subdivided in two stages. In this section, both phenomena are discussed, in the chronological order of occurrence.

Firstly, the walls of the bucket cut through the water. The trapped air within the bucket builds up a certain pressure, causing the water elevation within the bucket to be somewhat lower than that outside the bucket. An air cushion is created, which results in an additional upward buoyancy force upon the bucket. The pressure within this cushion depends on the size of the ventilation hole in the bucket. When it is chosen to small, the buoyancy force can induce tilting of the structure or worse, slack.

Once the water within the bucket rises up to the top, the relative velocity between the water and lowering speed induces an upward force: the slamming force.

4.4.1 Air cushion

Due to the fact that the air within the bucket is only able to escape through the limited area of the ventilation hole, there will be a pressure build-up within the bucket. This pressure pushes the water downwards and the bucket upwards, resulting in a difference in water level between the in- and outside of the bucket. Using fluid- and thermodynamic rules, an expression for the pressure within the bucket can be determined and solved. Whit this pressure the upward force acting on the jacket can be calculated.

Terms that are involved in this phenomena are shown in figure 4.10. In order to be able to determine and solve the equations, some assumptions are made. The most important one is that it is assumed that the water elevation inside the bucket is uniform and rises like a piston. Pressure distribution in the air cushion therefore is considered uniform too. Further, the air within the bucket is only able to flow outwards through the ventilation hatches. According to Faltinsen [15] though, compressibility of both air and water influences their interaction inside the bucket. When the air cushion 'collapses', air bubbles will be formed in the water, meaning that air does not only exit the cushion through the ventilation hole, but into the water too. Since this effect is complex and generally small on maximum local stresses, because it works in a time scale smaller than the one for local maximum stresses to occur, air bubble formation is not considered in this thesis.

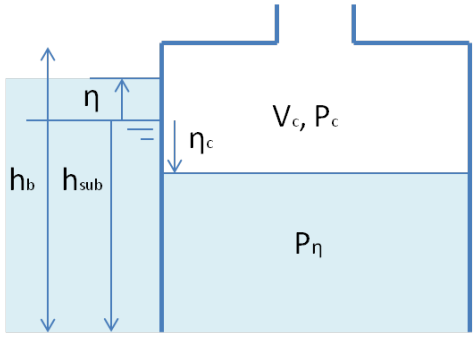

Figure 4.10: Air cushion in bucket

By using the mentioned assumptions in collaboration with some basic conservation laws, the pressures within the buckets can be determined. The air pressure within the bucket, $P_c(t)$, consist out of the constant atmospheric air pressure P_{atm} and a dynamic variation term $\mu(t)$:

$$P_c(t) = P_{atm} + \mu(t) \tag{4.15}$$

This cushion pressure is set equal to that of the water surface within the bucket $P_\eta(t)$, which contains the atmospheric air pressure, the pressure by the elevation of the incident waves and the pressure by the water elevation within the bucket $\eta_c(t)$ (both positive upwards):

$$P_\eta(t) = P_{atm} + \rho_w g\eta(t) - \rho_w g\eta_c(t) \tag{4.16}$$

By setting $P_\eta(t)$ equal to $P_c(t)$, an expression for $\eta_c(t)$ is generated:

$$\eta_c(t) = \eta(t) - \frac{\mu(t)}{\rho_w g} \tag{4.17}$$

These terms can now be used in the continuity equation, which is an equation based on the law of conservation of mass. The terms within this equation are discussed below.

$$-\rho_c(t)Q_{out}(t) = \frac{d\rho_c(t)}{dt}V_c(t) + \rho_c(t)\frac{dV_c(t)}{dt} \tag{4.18}$$

The outgoing volume flow of air, $Q_{out}(t)$ is determined using Bernoulli's equation, resulting in equation 4.19 [2]. A_v Is the ventilation hole area and C_r is the contraction coefficient, which according to Calvert [4] is 0.62 for sharp orifices.

$$Q_{out}(t) = C_r A_v \sqrt{\frac{2\mu(t)}{\rho_{air}}} \tag{4.19}$$

In order to be able to write an expression for the dynamic density of the air inside the cushion, $\rho_c(t)$, some additional assumptions are made. This term is dynamic due to the fact that adiabatic compressibility of the air is considered. The term 'adiabatic' indicates that there will be no transfer of temperature between the air of the cushion and its surroundings, and 'compressibility' means that a change of pressure within the bucket causes the air density to change in accordance. Lastly, the air is considered to be an ideal gas, which makes it possible to use isentropic relations. By using equation 4.20, $\rho_c(t)$ can be described in terms of initial pressure (P_{atm}), air cushion pressure ($P_c(t)$), initial density (ρ_{air}) and the ratio of specific

heat (γ_a, which has a value of 1.4 [18]). The water on the other hand is assumed to be incompressible, so ρ_w remains constant.

$$\rho_c(t) = \rho_{air}\left(\frac{P_c(t)}{P_{atm}}\right)^{\frac{1}{\gamma_a}} \tag{4.20}$$

By substituting the expression of the air pressure within the bucket ($P_c(t)$ in equation 4.15) into equation 4.20 and taking the time derivative, $\frac{d\rho_c}{dt}$ can be written in terms of the dynamic air cushion pressure and its derivative:

$$\frac{d\rho_c}{dt} = \rho_{air}\frac{1}{\gamma_a P_{atm}}\dot{\mu}(t)\left(1+\frac{\mu(t)}{P_{atm}}\right)^{\frac{1}{\gamma_a}-1} \tag{4.21}$$

The only term left in equation 4.18 is the instantaneous volume of the air cushion $V_c(t)$ and its derivative $\frac{dV_c}{dt}$. The former term can easily be determined using the bucket's geometry, by equation 4.22. A_{ti} here describes the inner area of the bucket, h_{bi} the inner bucket height and $h_{sub}(t)$ the submerged part of the bucket, as shown in figure 4.10. Since $z = 0$ at MSL, the latter term is equal to the global bottom coordinate of the bucket of interest and can be calculated using the jacket's COG global coordinate together with equation 3.11.

$$V_c(t) = A_{ti}(h_{bi} - |h_{sub} - \eta_c|) \tag{4.22}$$

The equation for $h_{sub}(t)$ is given in equation 4.23 and includes the global crane tip z-coordinate (z_{ct}), the load cable length ($L_{lc} + v_c t$), the elevation between the hook and the top of the jacket (determined by the sling length (L_s) and initial angle (α_0)), the elevation between the jacket's COG and -top (e_{tj}), and lastly the translated- and rotated global z-coordinate of the bucket's bottom. For readability reasons, $h_{sub}(t)$ is rewritten with all time-independent factors combined into z_{tot}.

$$\begin{aligned} h_{sub}(t) &= z_{ct} - (L_{lc} + v_c t) - (L_s cos(\alpha_0)) - e_{tj} + (z_j + \sin(\theta_j)x_{L0} + \cos(\theta_j)z_{L0}); \\ &= z_{tot} + z_j + \sin(\theta_j)x_{L0} + \cos(\theta_j)z_{L0} - v_c t. \end{aligned} \tag{4.23}$$

By substituting the acquired value into the volume determination in equation 4.22, and by rewriting $\eta_c(t)$ via equation 4.17, the air cushion volume and its derivative can be written in terms of all but $\mu(t)$ and $\dot{\mu}(t)$ known parameters (note that both $h_{sub}(t)$ and $\eta_c(t)$ are positive upwards).

$$\begin{aligned} V_c &= A_{ti}(h_{bi} + z_{tot} + z_j + \sin(\theta_j)x_{L0} + \cos(\theta_j)z_{L0} - v_c t - \eta + \frac{\mu}{\rho_w g}); \\ \frac{dV_c}{dt} &= A_{ti}(\dot{z}_j + \cos(\theta_j)\dot{\theta_j}x_{L0} - \sin(\theta_j)\dot{\theta_j}z_{L0} - v_c - \dot{\eta} + \frac{\dot{\mu}}{\rho_w g}). \end{aligned} \tag{4.24}$$

By substituting all these terms into equation 4.18, $\dot{\mu}(t)$ can be subtracted:

$$\dot{\mu}(t) = \frac{\dot{\eta} - \dot{z}_j - \cos(\theta_j)\dot{\theta_j}x_{L0} + \sin(\theta_j)\dot{\theta_j}z_{L0} + v_c - C_r\frac{A_v}{A_{ti}}\sqrt{\frac{2\mu}{\rho_{air}}}}{\frac{V_c}{A_{ti}\gamma_a P_{atm}}\left(1 + \frac{\mu}{P_{atm}}\right)^{-1} + \frac{1}{\rho_w g}} \tag{4.25}$$

The solution for $\mu(t)$ can be found by solving this first order equation, by introducing an extra degree of freedom into the solver in MATLAB. The initial conditions for both $\mu(t)$ and $\dot{\mu}(t)$ are zero.

Since equation 4.25 contains the square root of $\mu(t)$, trouble arises once $\mu(t)$ becomes lower than zero. Physically this means that the bucket sucks in air, which occurs once the water elevation within the bucket has a higher downwards velocity than the bucket itself. To take this phenomena into account, the square root should be rewritten. In order to do so, the source of equation 4.19 should be examined. The outward flux is determined using Bernoulli's equation:

$$\frac{1}{2}\rho_w v_{in}^2 + \rho_w g h_{in} + P_{in} = \frac{1}{2}\rho_w v_{out}^2 + \rho_w g h_{out} + P_{out} \tag{4.26}$$

Considering v_{in} and $h_{in} - h_{out}$ to be zero, the equation can be rewritten in terms of v_{out}, P_{in} and P_{out} (equation 4.27a). Since $P_{in} = P_c(t) = P_{atm} + \mu(t)$ and $P_{out} = P_{atm}$, $v_{out}(t)$ can be written in terms of $\mu(t)$. In order to get rid of the $\sqrt{-\mu(t)}$ term, equation 4.27b and 4.27c can be used for $Q_{out}(t)$. In the formulation of 4.25, the Q_{out} term changes from a minus to a plus (air flows inwards in stead of outwards). This may only be used if $\mu(t)$ of that specific time step is lower than zero.

$$P_{in} - P_{out} = \mu = \frac{1}{2}\rho_w v_{out}^2; \tag{4.27a}$$

$$P_{out} - P_{in} = -\mu = \frac{1}{2}\rho_w(-v_{out})^2; \tag{4.27b}$$

$$-v_{out} = \sqrt{\frac{-2\mu}{\rho_w}} \tag{4.27c}$$

Once the dynamic air cushion pressure is known, the buoyancy force it introduces upon the jacket, which is considered to be applied upon the middle of the bucket, can be calculated by multiplying $\mu(t)$ with the perforated top area of the bucket. This entire set of calculations obviously is to be performed for both buckets. The summation of these forces and moments respectively act on the z_j and θ_j indexes in the state space system.

Figure 4.11 shows how the buoyancy force induced by the dynamic air cushion pressure in the both buckets acts over time, when the jacket is lowered with a constant velocity of $0.5\frac{m}{s}$. The waves are created using a H_s of $2\ m$ and a T_z of $7\ s$, and the bucket starts somewhat above the water line. The fact that the force inside the right bucket drops to zero earlier than it does in the left bucket, indicates that the water inside the right bucket hits the top earlier.

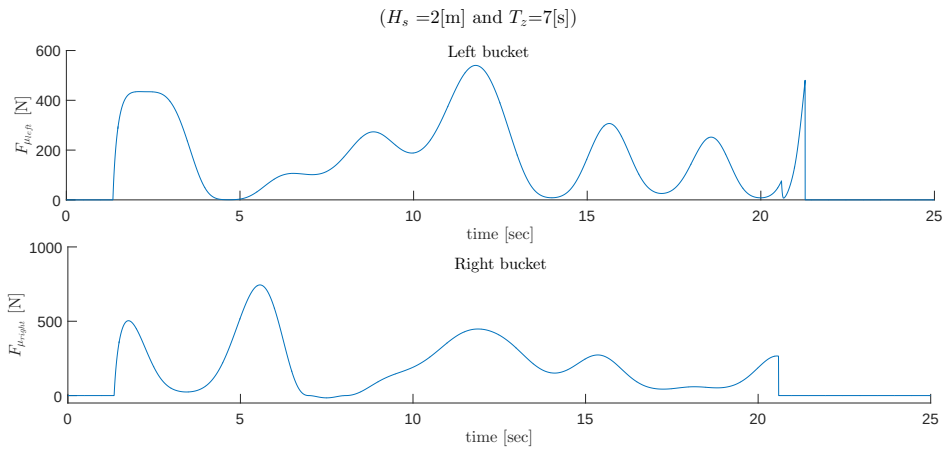

Figure 4.11: Force on buckets, caused by the air cushion's dynamic air pressure

4.4.2 Slamming

Once the water inside the bucket rises all the way up to the top, slamming occurs. The fact that this is a high, impulsive upward force makes it an important feature in terms of the slack criterion. It is hard to properly determine its influence, due to its non-linearity, random maximum value and unknown impact time. For this jacket design specifically, it is even harder to predict its form and magnitude, due to the influence of the air cushioning effect.

In this section, three methods are discussed that could be used in order to determine the slamming: by use of a slamming coefficient, by the change in added mass and by conservation of momentum. The first of these two methods are widely used in the field and recommended by DNV [9]. Due to the peculiar geometry of the buckets though, reliability of these methods is questionable. Therefore, the conservation of momentum, a more direct approach, is discussed too.

Slamming coefficient

Equation 4.28, an equation for the slamming force which is widely used in guidelines like DNV, shows it is primarily dependent upon the relative speed between the object and water surface, v_{rel}. Further, it introduces a slamming coefficient, C_s:

$$F_s = \frac{1}{2}\rho_w C_s A_{ss} v_{rel}^2 \tag{4.28}$$

The proper determination of this slamming coefficient is very complex and geometry-dependent. In practice therefore, the best way to determine C_s is by experiment, which is usually done by measuring forces during impact of the object upon the water surface. Assuming this acquired peak impact load is only made up by the slamming force, C_s can be extracted using equation 4.28. In reality however, it is not completely true that only slamming determines the impact force: drag, inertia, and buoyancy forces will also have a (small) influence. This assumption therefore often leads to overestimated values. In addition, since the slamming force depends on how and when the structure hits the water surface, results using similar conditions in experiments often show a considerable degree of scatter in C_s values, according to Selvåg [38]. The outcomes will greatly depend on the test set-up and calculation theory used. Since non of such experiments will be conducted during this thesis, a method should be found to properly determine the coefficient theoretically.

Many studies have been conducted upon the theoretical value of the coefficient, mainly focussed on wedges and cylinders. Even though these theories are not directly applicable to the suction buckets, it is good to gain insight in the phenomena.

A complete review of all methods goes beyond the scope of this thesis, but an introduction is given to the most common ones:

Initial theories were created assuming irrotational and incompressible flow and negligible air density, gravity and surface tension. The first investigation was done by von Karman in 1929 [44], who investigated the impact of floaters upon (still) water by considering a wedge-shaped under surface, having a so called dead-rise angle with the horizontal water line. Conservation of momentum between water and body was considered, so that the force could be calculated based on the change in added mass (the high-frequency added mass limit was used). He considered a flat plate, with a width of $2\ c(t)$ (with $c(t)$ being the wetted half-length: the distance between the centreline of the wedge and the undisturbed free surface). This free surface was assumed to be located at the undisturbed free surface. His model is shown in figure 4.12a.

Wagner in 1932 [47] continued on von Karman's research, because he was determined the free surface rise-up during penetration could not be neglected. This phenomena is caused by deformed free water surface, resulting in spray and the formation of a jet. His research resulted in a larger half-width of the flat plate, dependent on the vertical lowering velocity of the object and the dead-rise angle as is shown in figure 4.12b.

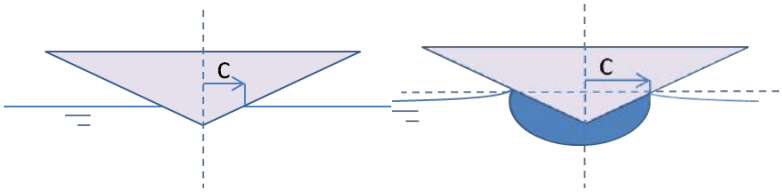

(a) Von Karman wedge **(b)** Wagner wedge

Figure 4.12: Wetted lengths

The width on which the slamming pressure acts determines the magnitude of the slamming force. The most important influencer of this width is the dead-rise angle. In addition to that, the pressure coefficient (equivalent to the slamming coefficient) increases rapidly for lower dead-rise angles. The lower the angles got, the less accurate von Karman's and Wagner's calculated coefficients seemed to be. In case their theories were used on flat surfaces, infinite impact pressures seemed to occur, since water was assumed to be incompressible. Taking compressibility of water into account, both men concluded that the magnitude of maximum impact pressure is equal

to the acoustic pressure: the product of fluid density, body velocity and velocity of sound in the fluid. However, drop test experiments on flat bottom structures (with a dead-rise angle lower than 2 to 3 deg) later show lower peak pressures than the values acquired from this theory. This was considered to be caused by the entrapped air between the body and water surface. The compressibility of both air ánd water therefore turned out to be important. In addition, if the air cushion that was formed would collapse, air bubbles would be created, affecting the water flow. So surface tension and water aeration significantly seemed to affect the maximum slam force (wet vs dry surface). Neglecting these phenomena therefore will give somewhat conservative values, according to Faltinsen [15].

Ma et. al. [29] later on describe the effect of the fluid compressibility during slamming. They state that the trapped air layer between a flat plate and a water surface expanses and contracts multiple times, resulting in pulsating loads on the structure: In the first impact, the air is extensively compressed and forms a thin layer when approaching to the water surface. It will deform the free surface near the edge of the structure (in their case a flat plate). The slamming pressure rises fast to its peak value and then drops, due to the fact that the air now starts to expand again. Lowering velocity dependent, this process could repeat multiple times, resulting in pulsating loads. The highest of these so-called space average slamming pressure peaks (at first impact), according to DNV [8] can be written in terms of v_{rel} and C_{pa} (the initial space average slamming pressure coefficient, with a recommended value of 2π for dead-rise angles of 0 deg). The pressure calculated by this relation, given in equation 4.29, can be integrated over the impact area in order to get the slamming force (for the bucket specific, that would be A_{ss}).

$$p_s = \frac{1}{2}\rho_w C_{pa} v_{rel}^2 \tag{4.29}$$

The outcome seems to correspond very well with the slamming force given in equation 4.28. It therefore appears that the slamming coefficient should be taken to be 2π. This value is equal to Wagner's' upper limit initial slamming coefficient for cylinders through the splash zone. It should however be noted that these coefficients are only valid during the initial stage of the impact and are assumed to be conservative when calculating the slamming load post impact. When this method is used for the slamming calculation of the bucket, when it is lowered with 0.5 $\frac{m}{s}$ and encounters an irregular wave with H_s of 2 m and T_z of 7 s, only the first slamming impact is considered and the constant C_s of 2π is taken into account, the calculated slamming force upon the left bucket is shown in figure 4.13a.

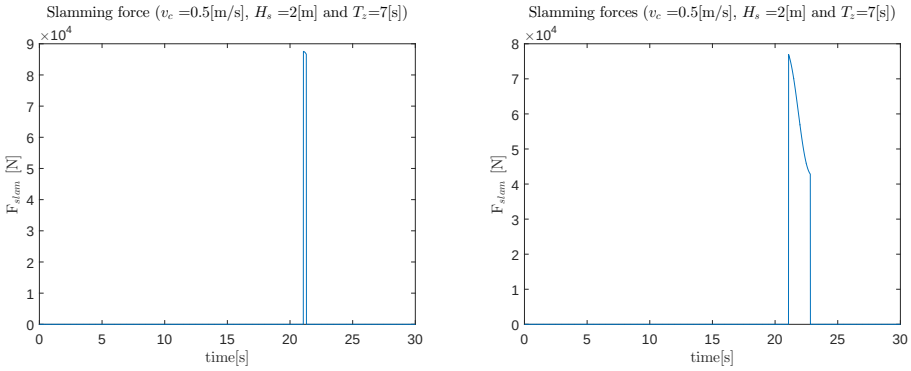

(a) Constant C_s of 2π **(b)** Varying C_s

Figure 4.13: Slamming forces calculated with slamming coefficient

Campbell, Wellicome and Weynberg [5] later on integrated the pressure distribution from the Wagner model over a plate and derived an expression for the slamming coefficient that decreases over time. This time dependent coefficient is given in equation 4.30. Using this method, the slamming coefficient is used for a somewhat longer period of time after impact: the initial impact is still 2π, but it decreases rapidly to a lower value. In figure 4.13b, the same calculations are done, using the varying C_s.

$$C_s = \frac{2\pi}{1 + 1.5\frac{Vt}{R}} \tag{4.30}$$

Going back to the geometry of the buckets, the vertical walls that entrap the water bounds the air and water to escape from the ventilation hatches only. Therefore, the theories described above are not entirely applicable to the buckets. Smith et. al. [39] showed, by means of experimental tests, that slamming forces on horizontal flat plates without vertical sides are significantly less than those on horizontal flat plates with vertical sides (2D). The magnitudes of the slamming forces in figure 4.13a and 4.13b indeed show lower values than those found for buckets in literature. E.g. a study on splash zone transition of the Gjøa ITS subsea structure with suction buckets performed by Naess et al. in 2014 [32] showed forces in the magnitude of 10^5 to 10^6. The buckets in their case were somewhat smaller than those treated in this thesis.

Furthermore, all studies described here consider flat water surfaces; ocean waves can be taken into account in the relative velocity, but the shape of the wave surface

within the buckets is hard to determine. These non-linearities make the empirical equations even harder to evaluate. The impact pressure distribution will in practice be non-symmetric, because of the non-horizontal water line and trapped air. The air cushion in the bucket has an effect on this too: the pressure by the upcoming water will in reality be distributed more symmetrically and the slamming impact time will somewhat differ. All of these factors depend on the relative velocity between the structure and the water surface, making it hard to determine when, how and to what extend slamming occurs.

Change in added mass

Another method to determine the slamming force, described by Faltinsen in 1990 [14], is by looking at what physically happens when a bucket is lowered through the splash zone. The bucket vertical walls first easily slide through the water, a negligible amount of heave added mass (a_{33}) is to be considered. Once the top of the bucket reaches the water-level though, this added mass rapidly increases to a way larger value, containing both the entire bucket area and the water volume that is entrapped within the bucket. This change in added mass is visualized in figure 4.14. An important feature of this assumption is that the added mass resulting from the pressure in the air cushion is neglected.

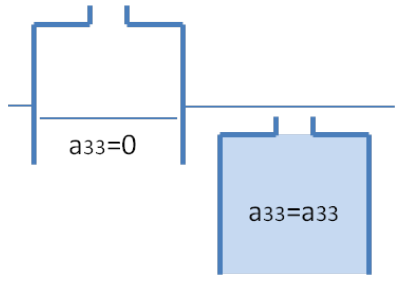

Figure 4.14: Change in added mass

The phenomena described induces a set of vertical forces upon the structure (F_3), containing an inertial force, which is related to accelerations and the slamming force, which is related to velocities:

$$F_3 = \frac{d(a_{33}v_{rel})}{dt} = a_{33}\frac{dv_{rel}}{dt} + \frac{da_{33}}{dh}\frac{dh}{dt}v_{rel} = a_{33}\dot{v}_{rel} + \frac{da_{33}}{dh}v_{rel}^2 \tag{4.31}$$

The slamming force is given by the last term in equation 4.31, and contains the change in heave added mass over submergence ($\frac{da_{33}}{dh}$) and the relative velocity between the water surface and the bucket top v_{rel}. In order to be able to solve this equation for the slamming force, the heave added mass should be written in terms of the submergence. Naess in 2014 [32] conducted research on this bucket splash-zone interaction. By means of model testing he found the relation between the heave added mass and submergence, as is shown in figure 4.15a.. He did so for a bucket of $7\ m$ high and $5\ m$ diameter.

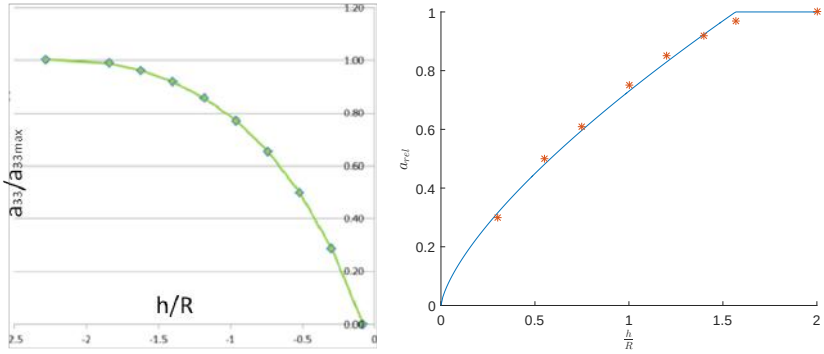

(a) According to model testing done by Naess [32]

(b) Approximation used in model

Figure 4.15: Change in added mass over submergence

Since the actual formulation of this graph was not given, an approximation of the formula is sought, by using the points found in the graph. This is done using the built in curve fitting tool in MATLAB, taking in mind that the slope of the graph especially is of importance for the slamming force. Due to the fact that this slope is highest for lower submergence, special care is taken in this part of the formulation. This can be seen in figure 4.15b, which shows the relation given in equation 4.32.

Due to the fact that the slope in the last points is almost zero anyway, no much care is taken in fitting the curve properly through the last points, which would make the formulation more complex.

$$\frac{a_{33}}{a_{33max}} = 0.73 \left(\frac{h}{R}\right)^{0.7} \tag{4.32}$$

The heave added mass of the fully submerged bucket, a_{33max} is calculated in appendix H. This is done by making use of the disk added mass described in DNV [9]. Knowing this added mass term, equation 4.32 is differentiated over h, giving $\frac{da_{33}}{dh}$ in equation 4.31. The only term left is the relative velocity between the bucket and the water surface, v_{rel}, which contains the vertical velocity of the wave elevation and that of the bucket, as can be seen in equation 4.33. The rate of the dynamic pressure within the bucket is taken into account here too, since the air cushion affects the bucket's vertical velocity prior to slamming. The wave elevation is taken to be that in the middle of the bucket.

$$v_{rel} = \dot{\eta} - \dot{z}_j - \cos(\theta_j)\dot{\theta}_j x_0 + \sin(\theta_j)\dot{\theta}_j z_0 + v_c - \frac{\dot{\mu}}{\rho_w g} \tag{4.33}$$

This formulation does take all influences of the bucket into account: the effect of the air cushion upon the relative velocity, the geometry of the bucket, the entrapped water within the bucket, and the perforation rate of the bucket. The slamming force now looks different from when it was calculated with C_s, as can be seen in figure 4.16. It shows an impulsive peak at the slamming instant, followed up by some fluctuations in magnitude, spread over the time in which the added mass is fully formed.

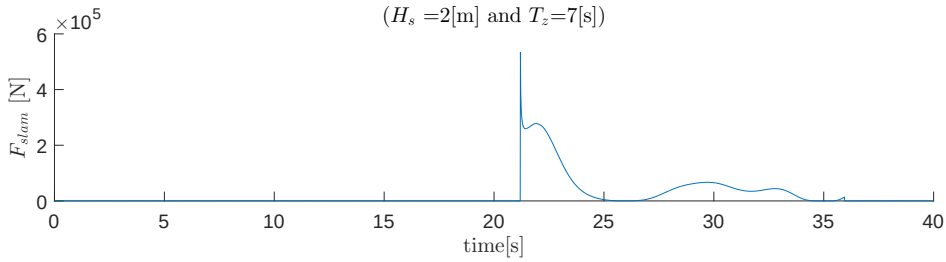

Figure 4.16: Slamming force calculated with change of added mass

Conservation of momentum

The latter method however still contains one uncertainty: the method used to describe the added mass over submergence is not very decent. Apart from the fact that no exact formulation is known for the dependency, it here is based on model testing on a bucket with different geometry than the one used in this research. A third method therefore is given, which does not describe the slamming in terms of a force, but as a jump in the jacket's velocity, both vertically and rotationally. This jump causes a sudden change in displacements, hence is directly linked to forces in the crane cable. Where the previous method was based on an impulsive force due to a change in momentum of the bucket individually, here the momentum of both the water and the bucket are considered together; conservation of momentum in this case is utilized.

A perfectly inelastic collision is considered, which states the amount of kinetic energy lost for the objects in collision is zero. The physical process can easily be explained by figure 4.17: two objects, with a certain mass and velocity, move towards each other. Once they collide, they stick together and move further as one object, with one new velocity [12]. This approach gives a way more realistic approximation of the slamming influence, due to the fact that all parameters and formulations used are actually known, so no major assumptions are to be made. The collision shown in figure 4.17 can be translated to the situation where the top of the bucket collides with the water inside of it. Due to its arm with the jacket's COG, rotational momentum should be considered too (containing the mass moment of inertia and rotational velocity). Both the vertical- and rotational velocity of the jacket will experience a jump in magnitude once slamming occurs.

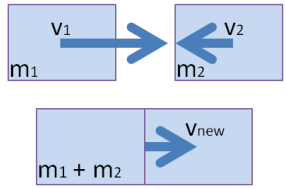

Figure 4.17: Perfectly inelastic collision

Due to the geometry of the jacket and since irregular waves are considered, multiple scenarios can be sketched in terms of the order of slamming occurrence. Depending on the water elevation within the buckets, either one of the buckets will

experience slamming prior to the other (or it could happen simultaneously). Further, the water within one (or both) of the bucket(s) could let go of the bucket top subsequential to slamming. For now, purely looking at slamming and not considering the disconnection of the water with the bucket after slamming has occured, there are three scenarios:

- The left bucket hits prior to the right;
- The right bucket hits prior to the left;
- Both buckets hit simultaneously.

As an example, the first of these scenarios is explained more elaborately. For this case the before- and after collision snapshots are sketched, each containing its own parameters required for momentum calculations. The according vertical- and rotational momentum conservation equations are given respectively in equation 4.34 for figure 4.18a and in equation 4.35 for figure 4.18b. Since calculations are performed as seen from the jacket's COG, the additional masses and inertias introduced by the water volumes result in non-diagonal mass matrices. The method used to determine and incorporate these matrices is described in section 4.5, since its resemblance with the added masses induced by submerged elements.

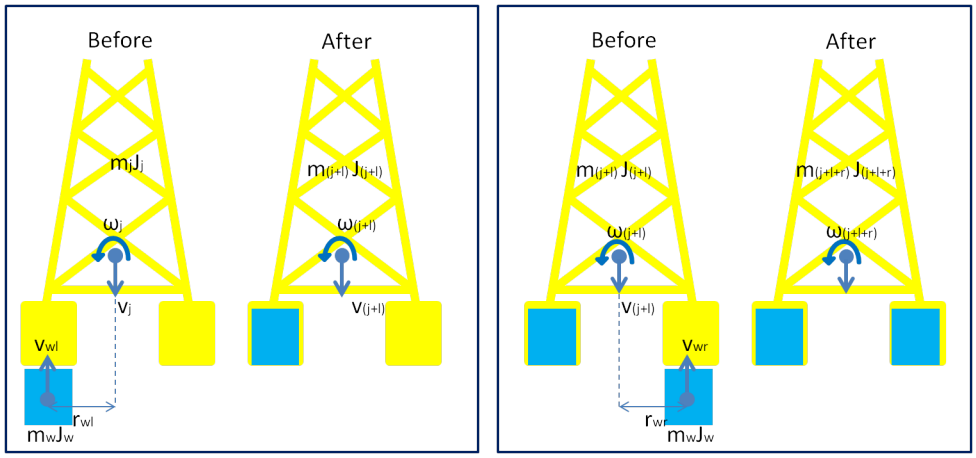

(a) Left bucket collision (equation 4.34) **(b)** Right bucket collision (equation 4.35)

Figure 4.18: System's conservation of momentum (the left bucket hits prior to the right)

$$\begin{aligned} v_{wl}m_w + v_j m_j &= m_{(j+l)}v_{(j+l)}; \\ -|r_{wl}|m_w v_{wl} + \omega_j J_j &= J_{(j+l)}\omega_{(j+l)}. \end{aligned} \tag{4.34}$$

$$\begin{aligned} v_{wr}m_w + v_{(j+l)}m_{(j+l)} &= m_{(j+l+r)}v_{(j+l+r)}; \\ |r_{wr}|m_w v_{wr} + \omega_{(j+l)}J_{(j+l)} &= J_{(j+l+r)}\omega_{(j+l+r)}. \end{aligned} \tag{4.35}$$

Within the MATLAB model, the collision method can be implemented by using the built in 'event-function', which for each time step detects whether a certain event occurs. In case of slamming, it detects when the difference between the water elevation in the bucket and the inside of the bucket is smaller than $10^{-4}\ m$. Once it finds out that this is the case, it stops the differential equation, tracks what has set off the action and acts upon that. For instance: once it tracks that the left bucket slammed the water, while the right bucket has not been submerged yet, it provides the solver with the jump in velocities by adapting the initial conditions of the next step by its new velocities, calculated with equation 4.34. It uses the outcomes of the time step prior to collision to do so. Once the initial conditions are changed, it switches to the next mode, in this example that where the left bucket is submerged, and the calculations continue.

In total there are four different modes to be encountered, all of which are shown in figure 4.19 (the blue buckets indicate submergence): either no buckets-, both buckets-, only the left bucket-, or only the right bucket- are/is submerged. Each of these modes has its own set of possible events, which are indicated by the arrows. Each of these events subsequently pushes the solver towards its own next mode.

In figure 4.20, the jumps in vertical jacket COG velocity (left lower figure) and the rotational velocity (right lower figure) due to slamming are shown, together with their reaction upon the global z-coordinate of the jacket (left upper figure) and its angle θ_j (right upper figure). The crane lowering velocity v_c here is set to zero, the jacket is positioned such that the bucket tops are approximately half a meter above MSL, and all forces but slamming are switched off. The red and blue circles indicate the moments where slamming occurs upon respectively the left and right bucket. The forces and influences involved in the water exit phases are not yet considered here. They will be discussed in section 4.4.3.

What can be seen in figure 4.20 is that just after the 2^{nd} second the waves hit the left bucket, causing an upward jump in velocity $\dot{z}_j$ and a negative jump in rotational velocity $\dot{\theta}_j$. These jumps cause an upwards displacement of the entire jacket and a rotation around its COG in the negative direction. Just before the 6^{th} second, the water hits the right bucket too, causing another positive jump in $\dot{z}_j$ and this time a positive jump in $\dot{\theta}_j$.

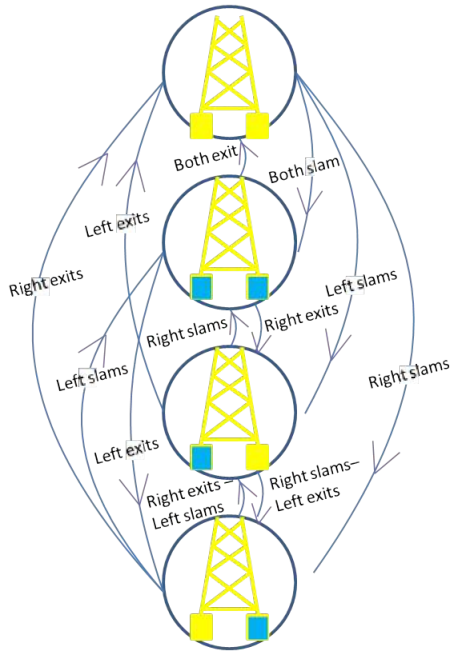

Figure 4.19: Collision diagram

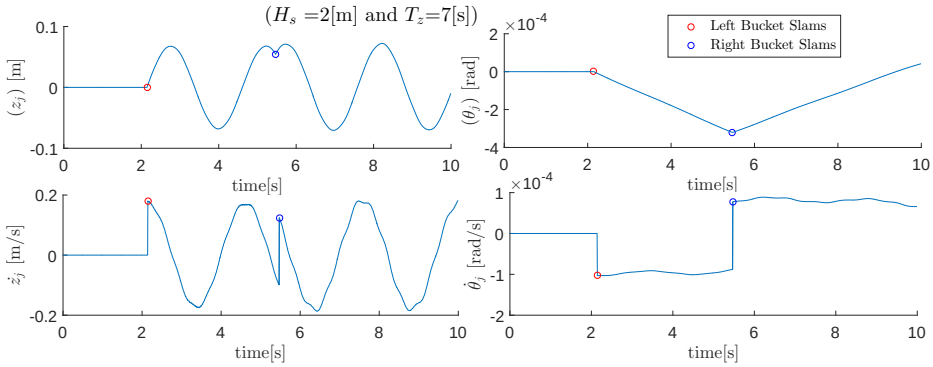

Figure 4.20: Jacket's vertical and rotational velocities, caused by collision

Slamming summary

In this section three methods of slamming determination are discussed: by using a slamming coefficient, the change in added mass and the conservation of momentum (collision). The first option already was rejected, since it does not properly consider the bucket's geometry, resulting in too low forces. When comparing the results from the latter two methods, a clear difference can be found. In order to be able to show these differences more clearly, a relatively small lowering velocity of the crane of $0.1\ \frac{m}{s}$ is considered and a simulation is done with all other forces but slamming switched off. In figure 4.21 from top to bottom respectively the force in the load cable, the vertical -and rotational displacement- and velocity of the jacket's COG are plotted. The red line shows the results found for the change in added mass method and the blue those of the collision method.

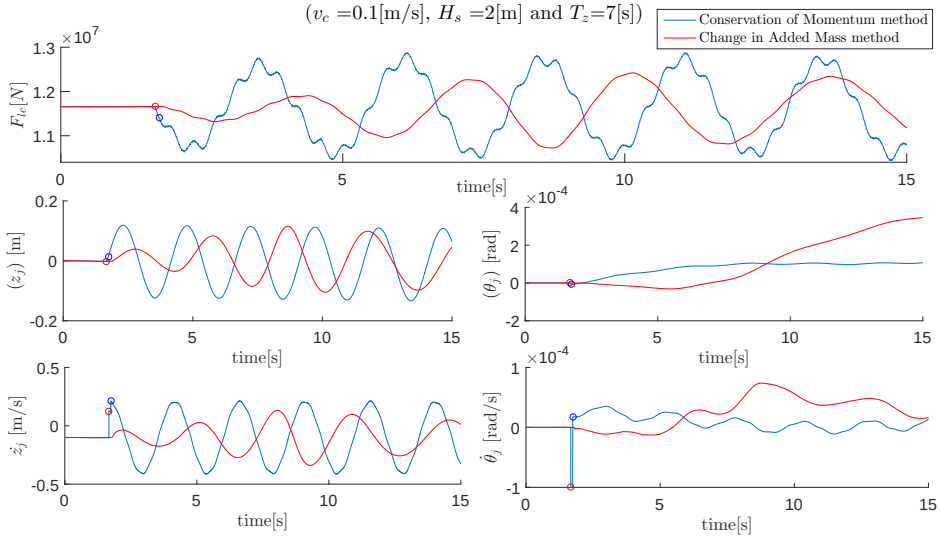

Figure 4.21: Comparison of slamming methods

Looking at the bottom figures, the difference between the two methods can clearly be seen: where the collision method introduces sudden jumps in velocity, the force due to the change in added mass causes it to grow spread out over a larger amount of time. The magnitude and immediate occurrence of the vertical jumps induce larger amplitude- and frequencies in vertical displacements and load cable

forces. Those in rotational direction cause totally different behaviour in rotation of the jacket too.

From this it can be concluded that the method of change in added mass lacks accuracy in sudden, impulsive behaviour, which is of the essence for slamming. With this knowledge, combined with the fact that less assumptions are made in the collision method, the latter method is considered to show results the closest to reality. Therefore, the method that uses conservation of momentum is used in the further processing of the model.

As was mentioned in the beginning of this section, the slamming phenomena is very non linear and hard to predict. Since it depends on the motions of both the water and the structure, the outcome of just one wave train per wave combination is not representative of what might happen in reality. It could be the case that, due to a small phase difference in the wave, the slamming force with the same parameters is way different in both magnitude and timing. In order to give a more accurate representation therefore for each combination of wave parameters multiple scenarios are to be studied, using a variation in seeds for random phase determination in the inverse Fourier transformation of the JONSWAP spectrum. This method will be explained more elaborately in chapter 5.

4.4.3 Bucket exiting

As was discussed in the previous section, it could occur that the bucket exits the water again, subsequent to slamming. When this happens, air gets sucked back into the bucket. This will happen with a certain delay, since the area of the ventilation hatch is smaller than that of the bottom of the bucket. The pressure at the bucket bottom therefore has more power to push the water upwards than the gravity and air pressure have to push it down. A visualisation of this phenomena is given in figure 4.22.

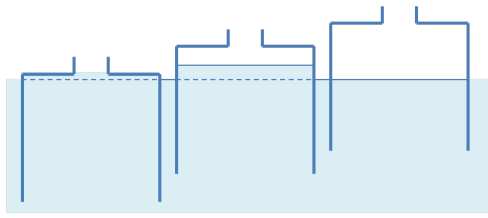

Figure 4.22: Bucket exit process

The air pocket that is created will exert a suction force upon the bucket, pulling it downwards with the water. The force of this under-pressure could be seen as the force needed to lift up the enclosed volume of water that is higher than the water-level on the outside of the bucket. This effect continues until the water level inside the bucket reaches that of the outside, and the pressure of the air within the bucket is equal to P_{atm} again. Likewise for the air cushion, the water elevation and pressure distribution within the bucket is considered to be uniform, which makes it easier to find descriptions of the volume of the air pocket.

In order to be able to determine this dynamic under-pressure, the continuity equation is used to determine the pressure and volume of the air pocket, like was done in section 4.4.1. Using the same assumptions, the continuity equation can be solved, from which a first order differential equation is filtered. By solving this equation, given in equation 4.36, the suction pressure due to water exit is calculated. Since the method used is comparable with that of the air cushion calculations in section 4.4.1, the derivation of $\dot{\mu}_s(t)$ can be found in appendix I.

$$\dot{\mu}_s(t) = \frac{\dot{\eta} - \dot{z}_j - \cos(\theta_j)\dot{\theta_j}x_{L0} + \sin(\theta_j)\dot{\theta}_j z_{L0} + v_c + \frac{A_v}{A_{ti}}\sqrt{\frac{2\mu_s}{\rho_{air}}}}{-\frac{V_s}{A_{ti}\gamma_a P_{atm}}\left(1 - \frac{\mu_s}{P_{atm}}\right)^{-1} - \frac{1}{\rho_w g}} \tag{4.36}$$

The force that acts upon the bucket due to the under pressure is calculated by multiplying the pressure with the bucket inner (perforated) area. In addition to this force, the mass of the entrapped water volume higher than the outside level should be incorporated in the system's mass matrix.

In figure 4.23 an example of the force on the left bucket due to suction (F_{μ_s} in blue) and air cushion pressure (F_μ in red) is given, for the same conditions as were used in the previous section. As can be seen, the overpressure (visualised in figure 4.24c) builds up in the bucket, until the water hits the top, at the 2^{nd} second. From that moment on the bucket is totally submerged, so there is no air inside it any more, hence the air-pressure is zero. Just before the 5^{th} second, the water-level outside the bucket has reached the level of that of the top of the bucket, in a downward fashion. Therefore, the process described in this section starts, and the dynamic suction pressure inside the bucket builds up (figure 4.24a). Once the water gets sufficiently low, the under-pressure is gone, the dynamic pressure drops to zero and there is no suction force any more (figure 4.24b). Once this happens, at approximately the 6^{th} second, the solver switches to the next mode, where it could detect the next slamming instant at the left bucket and where it incorporates the air

cushioning effect (F_μ). Depending on the relative velocities and movements of the water- and bucket, another over- or under pressure follows. These two methods are to be used separately in the solver, in order to be able to track the moment when it should jump to the next mode.

Due to the fact that the jacket is held still, this process continues itself two times in the plotted 30 seconds.

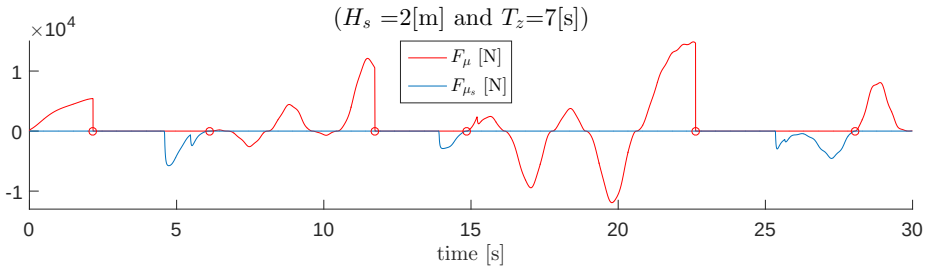

Figure 4.23: Left bucket air pocket forces due to suction and air cushion

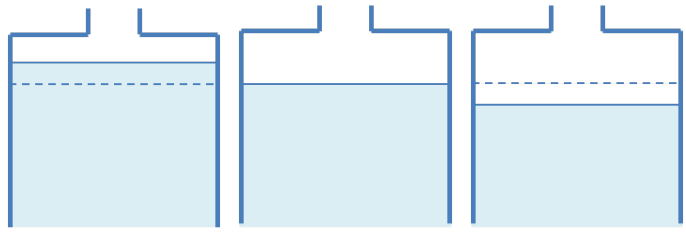

(a) Underpressure **(b)** Neutral **(c)** Overpressure

Figure 4.24: Air pressures inside bucket

The forces induced by these pressures are relatively low, so their influences upon the structure's velocity and displacements are fairly minor. As a comparison to the load cable force and vertical velocity found in the previous sector, in figure 4.20, in red a plot is made where the suction forces now are included (merely F_{μ_s}, so not F_μ). No direct noticeable influence of the suction force is found. In practice however, the fact that the bucket has exited the water entails another slamming will occur.

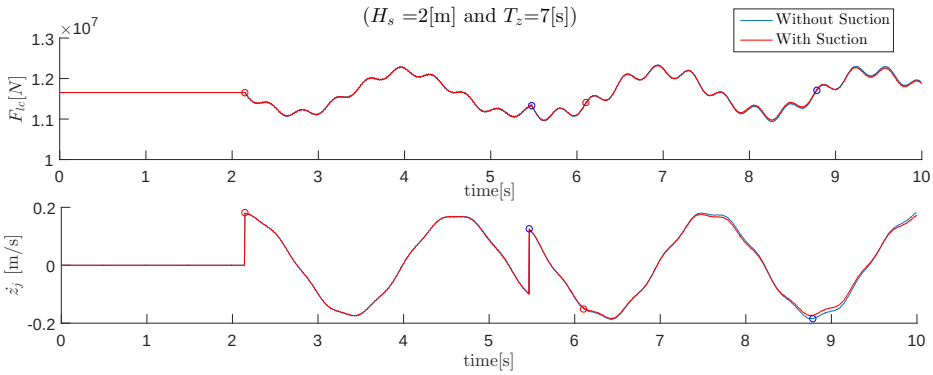

Figure 4.25: The influence of the suction force upon the vertical velocity

4.5 Added masses

So far in this chapter, only horizontal- and vertical added mass coefficients have been treated. The submerged components of the jacket however cause constant shifts in masses. Due to the fact that displacements are seen from the COG of the jacket in air, the added masses of the system are coupled, since the COG's of the submerged elements have an arm with that of the jacket. Changes of masses in x-and z- directions therefore initiate changes in the rotational directions too. For the jacket, each submerged element has its own added mass matrix, which is to be added to the mass matrix.

In order to determine the added mass matrix of an element i, the kinetic energy of that specific element is to be calculated, by using equation 4.37.

$$T_i = \frac{1}{2} m_i v_i^2 \tag{4.37}$$

The velocity of each element, v_i, can again be calculated using equation 3.11 and 3.13. The outcome of the acquired kinetic energy contains elements of the jacket COG's velocity degrees of freedom: $\dot{x}_j$, $\dot{z}_j$ and $\dot{\theta}_j$, respectively listed in the velocity array $\dot{q}_i$. The added mass matrix can now be determined by another definition of the kinetic energy, written in terms of this matrix and $\dot{q}_i$.

$$T_i = \frac{1}{2} \dot{q}_i^T M_i \dot{q}_i \tag{4.38}$$

By setting both definitions of the kinetic energy equal to each other, the added mass matrix can be subtracted:

$$M_i = \begin{bmatrix} m_i & 0 & \begin{matrix} -2m_i \sin(\theta_j) x_{L0i} \\ -2m_i \cos(\theta_j) z_{L0i} \end{matrix} \\ 0 & m_i & \begin{matrix} 2m_i \cos(\theta_j) x_{L0i} \\ -2m_i \sin(\theta_j) z_{L0i} \end{matrix} \\ \begin{matrix} -2m_i \sin(\theta_j) x_{L0i} \\ -2m_i \cos(\theta_j) z_{L0i} \end{matrix} & \begin{matrix} 2m_i \cos(\theta_j) x_{L0i} \\ -2m_i \sin(\theta_j) z_{L0i} \end{matrix} & \begin{matrix} m_i (x_{L0i}^2 + z_{L0i}^2) \\ +J_i \end{matrix} \end{bmatrix} \tag{4.39}$$

For each submerged element, the mass m_i, inertia around its own COG J_i, and arms x_{L0i} and z_{L0i} are to be inserted in this matrix, which is than added to the mass matrix of the jacket.

In figure 4.26, the jacket's COG displacements and rotations, as well as the force in the load cable are shown, in case the added mass matrices are considered (the blue line) and in case they are not (the red line). All forces discussed in this chapter were taken into account in these calculations. It seems the added mass has quite some influence on the system: somewhat smoother displacements are the result of the growth in inertia, which causes amplitudes to be larger.

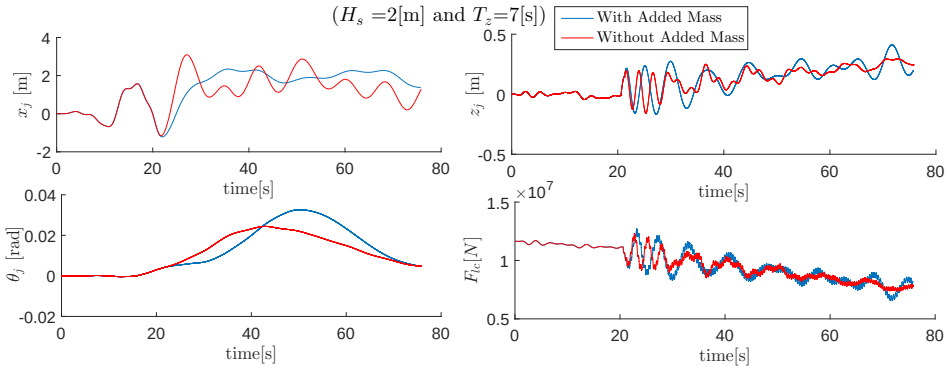

Figure 4.26: Displacements, rotation and load cable force with and without the influence of added mass

Another important element of the added mass is the effect it has upon the eigen-period of the system. As can be seen in the vertical jacket displacements, in figure 4.26, the jacket without added mass involved oscillates in the eigen-period found in section 3.6. The jacket that is being lowered with the influence of the added mass on the other hand shows different behaviour.

A comparison of these two, without external forces involved and with the jacket given an initial vertical displacement of $+0.1$ meter, is given in figure 4.27. The upper and lower figure respectively show the jacket behaviour without and with added mass. The period with added mass grows more rapidly once the jacket is submerged (at approximately the 20^{th} second). The additional inertia causes the jacket to oscillate slower than before; the more jacket elements submerge, the higher this delay is. Where the eigen-period without added mass growed from 2.5 to 2.7 s, here it increases to 6 s. Like was mentioned in the previous chapter, the closer the wave period is in range of the eigen-period of the system, the higher the chance on resonance and large load cable forces. Since for the eigen-period with added mass included the value varies between 4 and 6 seconds, the lower period waves considered in this thesis will probably result in large DAFs.

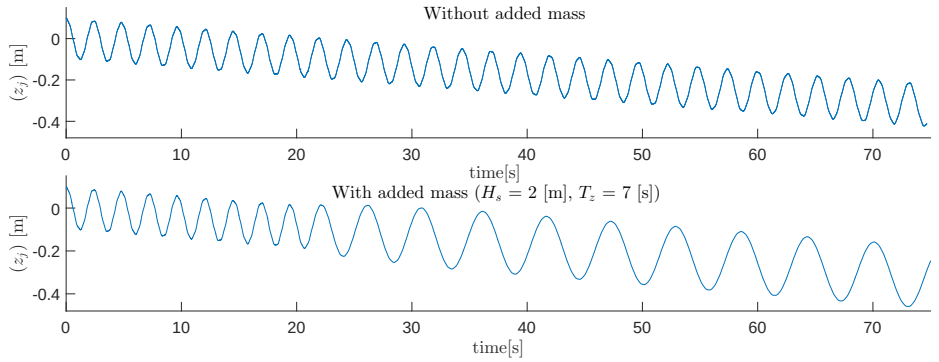

Figure 4.27: The influence of added mass on the jacket's vertical oscillation

4.6 Bucket in proximity of the seabed

As soon as the buckets reach close proximity of the seabed, flows of the surrounding water change and affect the forces upon the jacket. According to guidelines in DNV [9], the three most severe effects are the following:

- Changes in added mass;
- Change in drag terms;
- Hydrodynamic pressure build up inside the buckets.

Even though these phenomena are probably not directly influenced that much by the wave conditions, since the buckets are distanced far from the surface, the displacements and velocities of the jacket due to the process prior to this period do differ for different wave conditions. This jacket behaviour subsequently influences the magnitudes of the forces discussed here. Therefore, the forces in this region are taken into account within the model. The determination of these forces is done in a somewhat more approximate fashion, partly by uncertainties in coefficient behaviour.

From the determination and implementation of these forces, which can be found in appendix J, it turned out that dominant terms act asymptotically for smaller distances to the seabed. This asymptotic behaviour in practice is liquidated by the decreasing vertical velocity of the jacket, since the crane operator decreases his lowering speed when the buckets almost touch the seabed. In the model however only one constant lowering velocity is used, resulting in no nullification of the phenomena and thus large forces (up to $10^7\ N$, which is close to the jacket's weight). Therefore, the solver is stopped approximately 30 % of the bucket diameter from the seabed, in order to prevent these non realistic forces and displacements to occur. Even though the forces are incorporated in the model, they will not influence the jacket's behaviour that severely, during this limited simulation time. In section 6.3.3, the effect these forces have upon the load cable forces, when different lowering velocities are used are discussed.

4.7 Parameters

In order to be able to run simulations with the model, some parameters remain to be chosen. In this section, respectively the lowering velocity of the crane, the amount of load cable elements and the amount of sling elements are chosen. As was previously mentioned, in order to choose these parameters, the presence of all forces and influences are a requirement.

4.7.1 Crane lowering velocity

As was discussed in section 4.4 the forces in the splash zone transition are influenced by the lowering velocity of the crane. When the jacket is lowered at a fairly low

velocity, the relative velocity between the bucket and the water will be somewhat lower, resulting in lower force magnitudes. On the other hand, more wave elevation changes will induce larger fluctuations in the air cushioning formation, and multiple slamming impacts might occur. In practice it is often chosen to use high lowering velocities in the splash zone. Despite the fact that forces will be somewhat higher, they will only occur once. However, for now it is not yet known which of these two options are preferred in terms of the sketched criteria.

According to DNV, a normal crane lowering velocity in offshore operations like this is $0.5\ \frac{m}{s}$ [9]. The incremental in the splash zone however could go up to $1\ \frac{m}{s}$. In order to get a quick view on the influence the lowering velocity has upon the air cushioning effect and slamming, for three different crane velocities the left side of figure 4.28 shows the air cushion force as well as the suction force for the left and right bucket in respectively the upper and lower figure. The right figure shows the velocity jump, with respect to the lowering velocity. The solver is ran until both buckets are submerged a distance of half their diameter, so no more bucket exit can occur. The blue line shows the splash zone transition for $v_c = 0.2\frac{m}{s}$, the red line for $0.5\frac{m}{s}$ and the green line for $1\frac{m}{s}$. Striking is that for a lowering velocity of $0.2\frac{m}{s}$, multiple slamming occur. Apparently, using these wave conditions, this lowering velocity is not sufficient to prevent this from happening. For the other two velocities this is not the case.

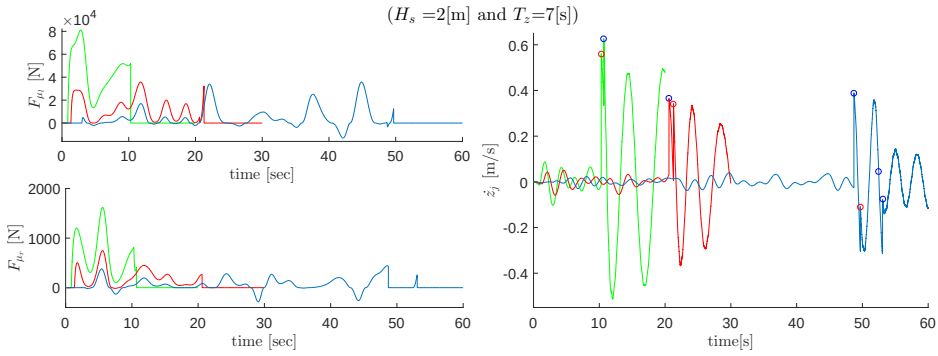

Figure 4.28: Air cushion forces and velocity jumps for different crane lowering velocities

In figure 4.29, the load cable DAF values are shown for a set of crane lowering velocities ranging from 0.1 to 1 $\frac{m}{s}$, with increments of 0.05 $\frac{m}{s}$. This is done for waves with a H_s of 2 m and a T_z of 5, 6, and 7 s. In figure 4.30, the according number of slamming occurrences are given.

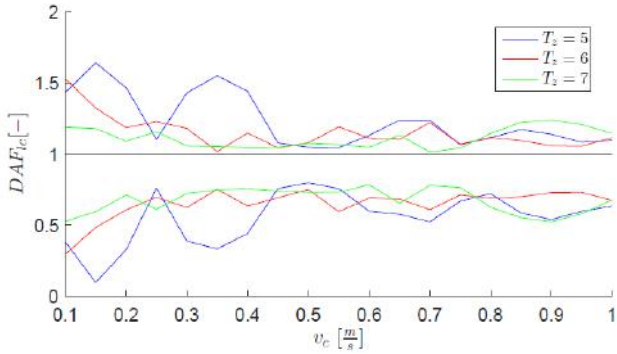

Figure 4.29: Maximum and minimum DAF for different crane lowering velocities

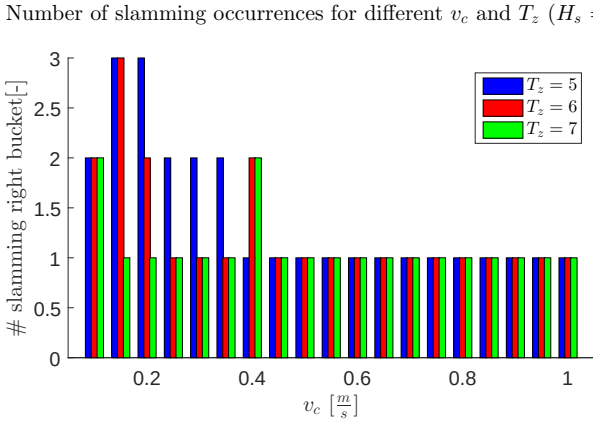

Figure 4.30: Number of slamming occurrences for different crane lowering velocities

Even though it seems that high DAF forces seem to be correlated with multiple slamming, which happens for lower lowering velocities, conclusions can not be drawn by these figures, since only wave conditions with one constant random phase

are considered. A parameter study on the lowering velocity is not a goal of this research though, therefore such a study is not performed here. It is chosen to use a velocity of $0.5\ \frac{m}{s}$, recommended by guidelines in DNV [8]. This velocity is kept constant during the entire process of installation, in order to make sure that no accelerations occur directly caused by the crane.

4.7.2 Number of load cable elements

In section 3.1 it has been stated that the amount of load cable elements still remain to be chosen. It is to be found out for which amount of load cable elements the outcomes converge to a certain output. A factor of consideration herein is the amount of time it takes in order for the solver to find the solution. For a higher amount of elements, the solver has to work with a larger set of degrees of freedom, resulting in larger computational time.

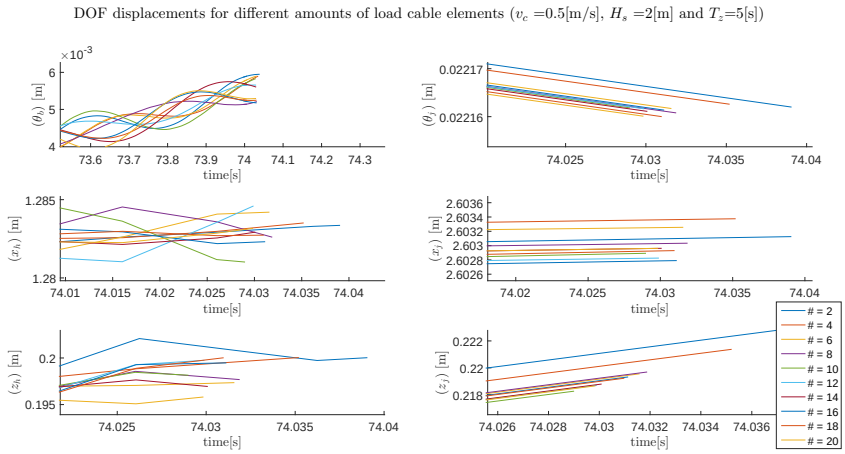

Figure 4.31: Different numbers of load cable elements

Using a set of rather fierce wave conditions ($H_s = 2\ m$ and $T_z = 5\ s$), the outcomes for a set of 2 to 20 load cable elements with increments of 2 elements are sought. The displacements of all DOFs for these different amount of elements are plotted in figure 4.31. The plots are zoomed in at the final time, in order to be able to see the differences. For these amounts of load cable elements the differences are maximal 1 %. On the other hand, the time it takes for the code to solve the problem for 20 cable

elements, $2498\ s$, is ten times higher than the time it takes to solve for 2 elements, $244\ s$. This difference in time does not weigh up to the minor improvement in accuracy. Considering the fact that for the analysis eventually a large set of calculations are to be done, it is chosen to work with 2 load cable elements for the resulting time of this research.

4.7.3 Number of sling elements

Likewise for the load cable, the number of sling elements are to be chosen. For the same wave conditions used in the previous section, a set of five different numbers of sling elements are tested (1, 3, 5, 7 and 9 elements). The difference in the displacements of all DOFs is shown in figure 4.32 and once again seems to be really small. The difference in time it takes to solve however is significantly higher for more sling elements: $13,702\ s$ for 9 elements versus $244\ s$ for 1 element. Here too, this time difference does not weigh up to the accuracy achieved. It is therefore chosen to work with 1 sling element for the remaining of the research.

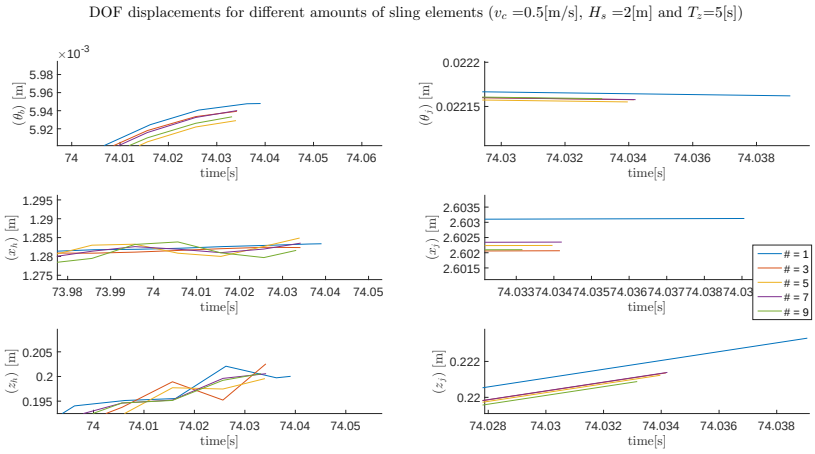

Figure 4.32: Different numbers of sling elements

4.8 Forcing summary

In this chapter the external forces induced by the environmental conditions are discussed. The equations used in the model to incorporate these forces are given and all relevant choices and assumptions are explained. The biggest assumptions made are structural approximations of jacket members, in terms of equivalent diameters, submerged volumes, and area's on which forces act. Further, diffraction is not taken into account, some fluid- and thermodynamic assumptions are made in air cushion determination, and lastly some forces that are assumed to have a negligible effect are not considered. In chapter 6, the assumptions made are set up for discussion and some of the neglected forces are discussed more elaborately.

The three installation stages that are primarily of interest are shown in figure 4.33, from left to right respectively describing the splash zone transition, the region in between the splash zone and seabed and the region where the buckets reach proximity of the seabed. The first zone is dominated by air cushioning effects and slamming forces. Both these effects are hard to predict, since they depend on the bucket geometry and the relative velocity between the water and jacket. It has been chosen to determine slamming via the conservation of momentum. The subsequent stage is dominated by the forces induced by wave kinematics and by constant changes in submerged volumes, resulting in buoyancy forces and added masses. In the last stage, changes in added mass, drag and a pressure build up in the bucket influence the system's behaviour.

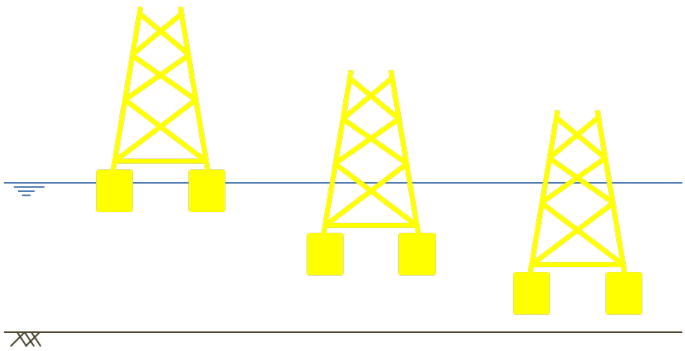

Figure 4.33: Installation stages

Chapter 5

Analysis

In this chapter, the model is used to analyse how the system behaves on the forces described in the previous chapter. In order to gain a first insight in the individual force contributions upon the load cable forces, one specific wave combination is used to study the jacket's behaviour when forces are switched on and off. This analysis is performed in section 5.1.

By running the simulations for each of the wave combinations of interest, the actual goal of this thesis can be achieved. Since one simulation does not encounter the randomness in irregularity of the waves, for each of the wave combinations these simulations are ran multiple times, with different initial conditions: in section 5.2 a Monte Carlo simulation is used in order to illuminate wave combinations that do not satisfy the criteria sketched in chapter 2. In this section further more cases have been studied that showed particular behaviour, in order to increase the insight in individual force contributions and their interaction with each other.

The downside of a Monte Carlo simulation is that it introduces large computational times, especially when it is to be repeated project specifically for multiple wave combinations. In order to prevent this, another option would be to find wave condition specific worst case scenarios. An effort in finding these cases is done in section 5.3.

Lastly, by using brutal computer calculation force in section 5.4, a well known statistical distribution is sought, by using a larger number of seeds in the Monte Carlo simulation. Such distributions can be used in order to predict probabilities of intolerable DAF values.

5.1 Force contributions

It is interesting to see how the jacket behaves in certain wave conditions and which forces seem to dominate in influence on this behaviour. Looking at this specific jacket design, especially the effect slamming has on the displacements and forces in the load cable is interesting. In this section therefore an analysis is performed, where the contribution of each force is studied separately. These studies are based on the output of one specific wave combination: a H_s of 2 m and a T_z of 7 s. This combination is chosen since it is common in the North sea according to Haver [19] and, as was explained in chapter 1, 2 m significant wave height is assumed to be the maximum allowable boundary value.

In figure 5.1, the response in terms of the jacket's COG displacements (on the left) and velocities (on the right) are given, from the top respectively the rotation, x-displacement, and z-displacement are shown. Once again, the red and blue circles represent slamming on the left and right bucket respectively.

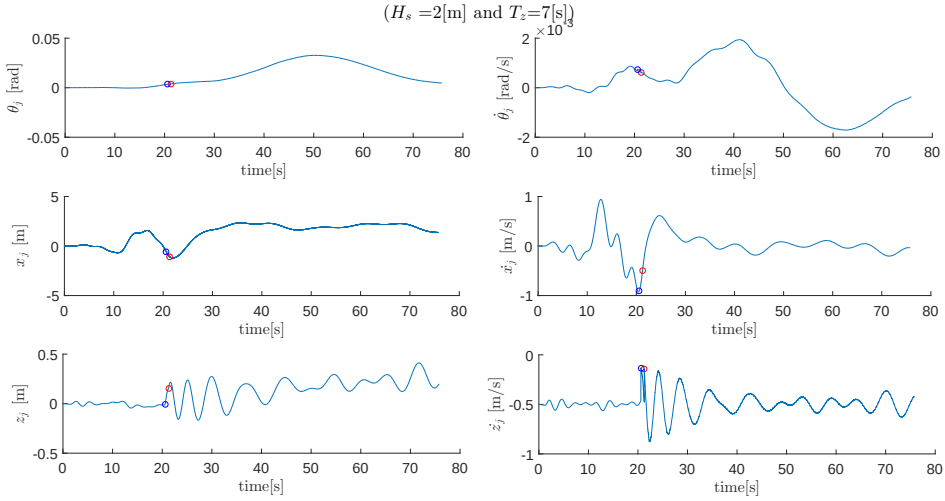

Figure 5.1: Jacket's COG displacements and velocities

In figure 5.2 the according load cable DAF is given. Looking at both figures, several particular behavioural patterns can be found. Knowing how forces in the system are modelled, some of these patterns can immediately be linked to certain forces.

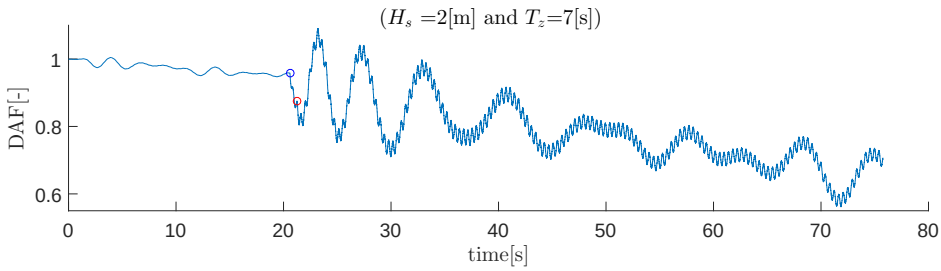

Figure 5.2: Load cable DAF

5.1.1 Buoyancy

In order to show actual the influence buoyancy has upon the jacket's behaviour, in figure 5.3 the DAF, z_j and $\dot{z}_j$ are plotted, with and without buoyancy switched on, respectively in blue and red.

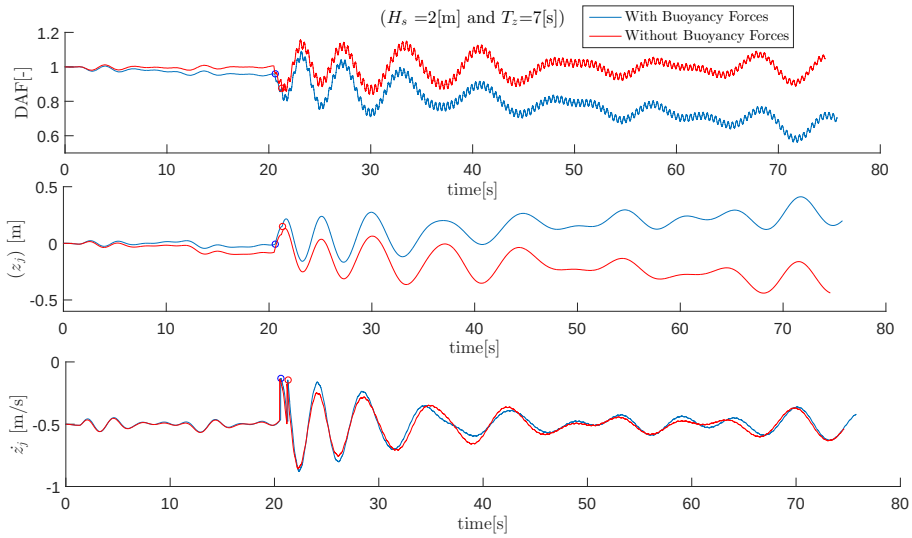

Figure 5.3: Results with and without buoyancy

What can be seen here, is that the jacket without buoyancy is not being pushed upwards, and load cable DAF fluctuates around 1.

5.1.2 Slamming

A next striking observation in figure 5.2 is that from the moment slamming occurs an extra, high frequency oscillation is added to the system. Looking at this phenomena more in detail, the same analysis is performed as was done for the buoyancy, this time with the slamming force switched off in the solver. Comparing the results with the previously acquired ones, the high frequency oscillation seems to have something to do with the velocity jumps induced by slamming: in the upper figure in figure 5.4, which represents the DAFs with (blue)- and without (red) slamming, it can be seen that for the latter one, the high frequency oscillation is not induced at all.

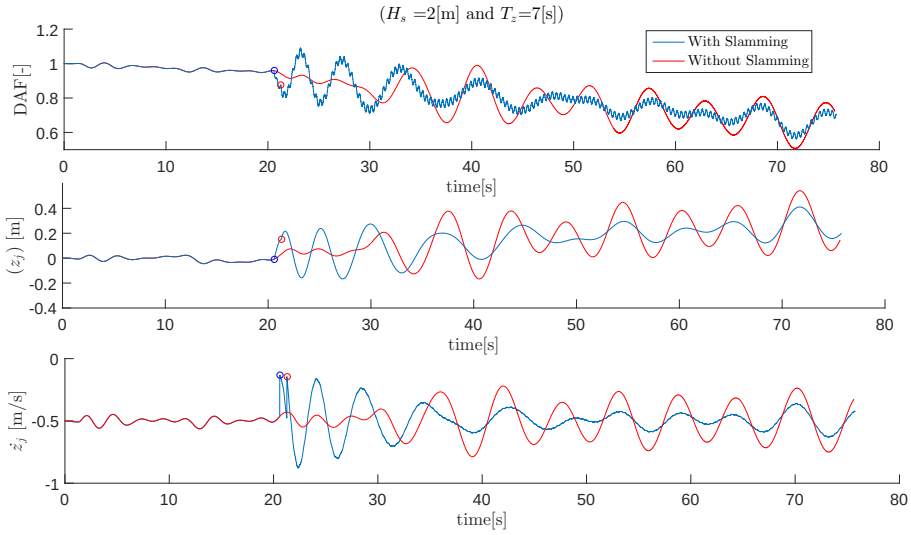

Figure 5.4: Results with and without slamming

For the case where slamming is still switched on in the vertical displacement and velocity, respectively displayed in the mid- and lowest figure in figure 5.4, the small oscillation can not be found back. Looking at figure 5.1, it could neither be found in the rotational- or x-directional movement of the jacket's COG. Studying the remaining degrees of freedom of the system however, the exact same period was found in the rotation of the crane boom θ_b, as is shown in figure 5.5.

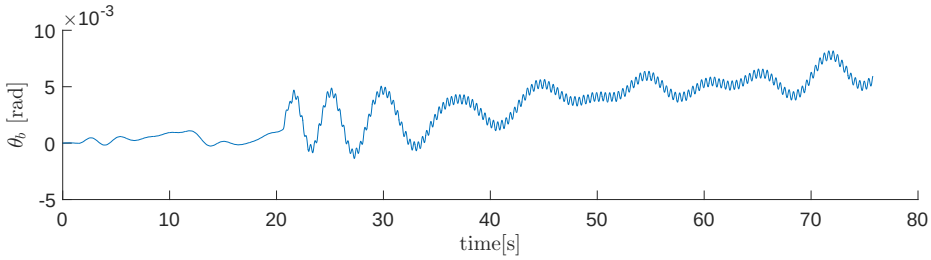

Figure 5.5: Crane boom's rotation

It seems that the slamming induces the crane boom to oscillate in its eigen-period: the sudden jump in velocity is transferred all the way through the jacket members, the slings, the hook and the load cable. In order to visualise this, in the left figure in figure 5.6 the crane boom's eigen-period is shown in blue. This oscillation is created by giving the crane boom an initial rotation of $-0.002\ rad$. The slamming effect is represented by giving the jacket an initial upward displacement of $0.1\ m$ and dropping it from there, which is shown in the red line. Both boom rotations oscillate in the exact same period, proving that slamming does initiate the boom rotation.

The amplitude of this additional oscillation further depends on the timing and magnitude of the slamming. Zooming in on the DAF that was found before, with slamming involved (which is done in the right figure), it can be seen that the boom rotation induced by the left bucket slamming shows a somewhat smaller amplitude than the one induced by that of the right.

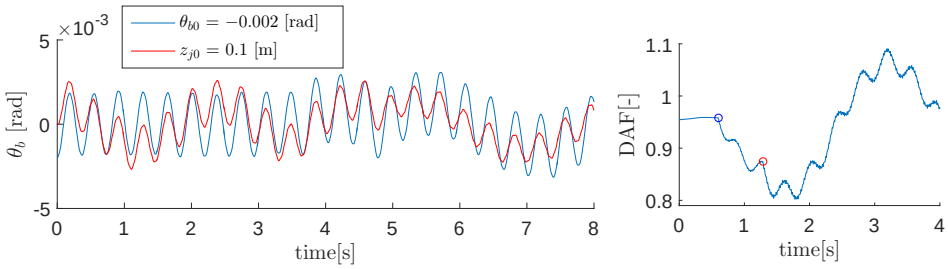

Figure 5.6: Study on small frequency oscillation, induced by slamming

Going back to figure 5.4, where the behaviour with and without slamming was compared, it can be seen that apart from the additional high frequency oscillation, the behaviour of the system without slamming is quite different than it was with slamming. When slamming is involved, the jump in velocity causes vertical displacements and upwards forces. The load cable DAF therefore drives downwards earlier in time than is the case without slamming. As a reaction to that, the jacket starts oscillating in the cable, with the same period as the rigging eigen-period with added mass, as was found in section 4.5.

Summarizing: the slamming initiates the jacket to oscillate in the crane, in the eigen-period of the crane and its rigging, together with added mass. The sudden jump in velocity is transported all the way through the jacket, slings and load cable and induces the crane boom to oscillate in its eigen-period. This oscillation causes the origin of the load cable, the crane tip, to oscillate too, resulting in the same oscillation in the load cable force and DAF.

5.1.3 Vertical wave kinematics

Where the slamming initiates the jacket to oscillate in the system's eigen-period, over the remaining time of installation this oscillation's period grows more extensively than observed before, in section 4.5. The amplitude of this oscillation is highly affected too. One might expect that the forces that have the highest effect in these phenomena would be those induced by the vertical waves, since these forces dominate in vertical direction. In order to find out what the effect of these forces is, a run with them being switched on in blue, and off in red, is performed. The results found are plotted in figure 5.7. All other forces, including slamming, are taken into account in these runs.

As expected, the vertical wave forces (both drag and inertia) indeed have a large effect on the vertical oscillation. These effects specifically are large starting at the approximately 30^{th} second, corresponding to the region where both the buckets and the horizontal braces are to the largest extend affected by the waves, as was explained in section 4.3, figure 4.9. For this case, the vertical wave forces seem to actually subtract energy from the system, since the amplitudes of the oscillations without these forces switched on are smaller than those without them being considered. The period of the red line further seems to be more aligned to that of the eigen-period of the rigging with added mass, showing that these forces affect the period of the oscillation too.

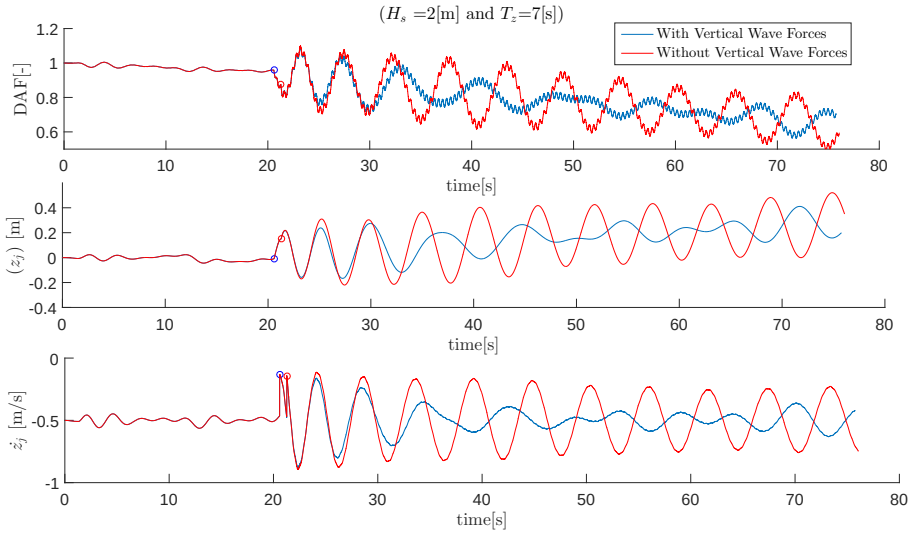

Figure 5.7: Results with and without vertical waves

By looking at the influence of the drag- and inertia terms separately, which is done in figure 5.8, the vertical wave forces appear to be inertia dominated. The behaviour of the red line, where the inertia terms are switched off, seems to correspond better with the red line in figure 5.7, where no vertical wave forces were considered. The inertia here thus causes the delay in oscillation and the dampened amplitude. The drag term on the other hand does not seem to have a large influence on both characteristics: the green line, where vertical drag forces are neglected, does not differ that much from the blue line, where both terms are switched on. Since both forces are $90\ deg$ out of phase, due to the phase difference between velocity and acceleration, the fact that the summation of the two almost equals the inertia term shows that the amplitude of this term for this specific case is higher than that of drag.

Summarizing: the vertical wave forces influence the vertical oscillation of the jacket, both in amplitude and the period of oscillation. It seems that it accelerates the growth of the oscillation period and for this specific case it dampens out the amplitude.

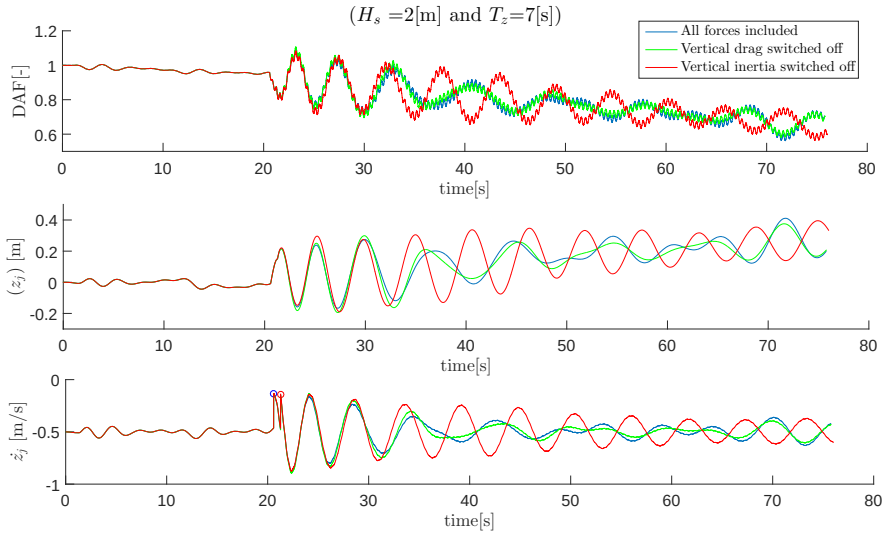

Figure 5.8: The influence of vertical wave drag- and inertia

5.1.4 Air cushioning

In figure 5.9, the contribution of the air cushioning effect is studied. Even though its direct influence upon the system is fairly low, it should be noted that it does influence the behaviour prior to slamming. Therefore, even though it is not visible for this particular case, it could affect both the timing- and magnitude of the slamming. Since it was discovered that slamming does have quite an influence on the system, the air cushioning effect could in fact indirectly lead to high forces in the load cable.

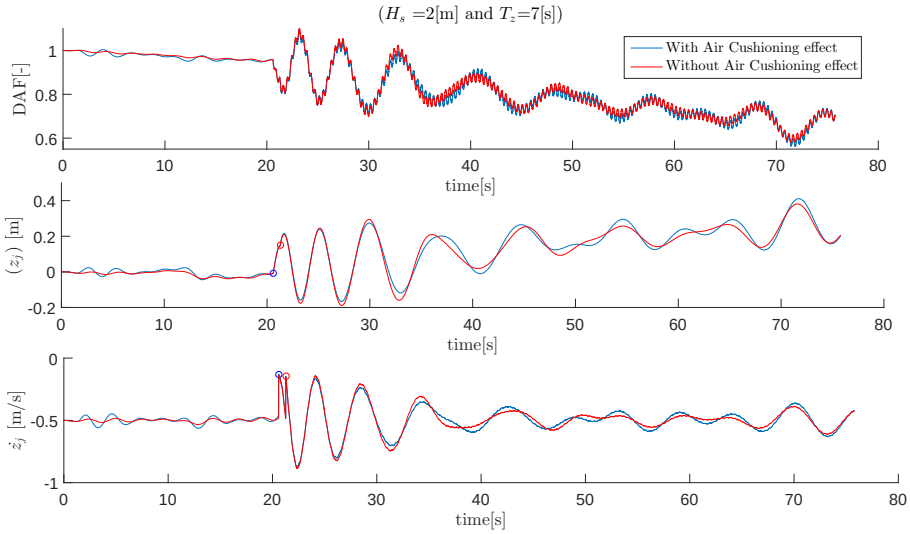

Figure 5.9: Results with and without air cushioning

5.1.5 Horizontal wave kinematics

Lastly, it is interesting to see to what extend the horizontal forces influence the jacket behaviour. So far it has been stated multiple times that the horizontal wave forces do not have a large effect on the forces in the load cable. Looking at figure 5.10, where calculations are performed with (blue) and without (red) horizontal wave forces incorporated, this assumption indeed seems correct.

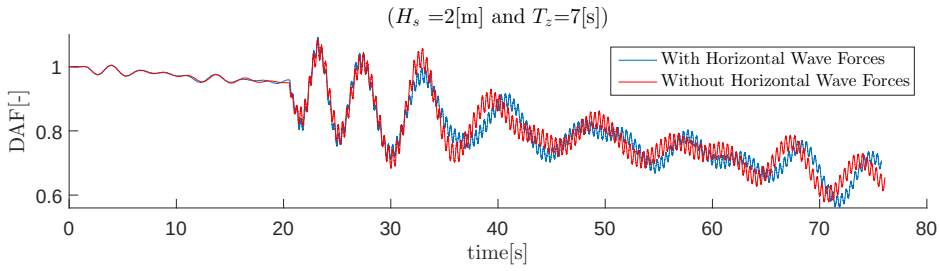

Figure 5.10: Load cable DAF with and without horizontal wave forces

It is interesting however to see what the effect is on the rest of the degrees of freedom. As can be seen in figure 5.11, the behaviour in x-direction is totally different without horizontal waves being considered. Logically, since not one of the remaining external forces act upon the jacket works in this direction. The horizontal waves have a large effect on the rotation of the jacket too (θ_j). This too is logic, since horizontal displacements automatically induce rotations of the jacket, due to the non-symmetrical geometry over the horizontal and due to the the fact that the jacket is pulled back by the crane boom.

What further can be observed in figure 5.11 is that the horizontal waves create large horizontal displacements prior to slamming, at the approximately 20^{th} second. This is logic because this is the period where the buckets cut through the surface; creating large areas for the horizontal waves to act upon. Keeping in mind that wave elevations and kinematics are calculated using global x-coordinates, and assuming the vertical velocity of the jacket is slightly lower due to the horizontal displacement, the horizontal wave forces too have an indirect effect upon the magnitude and timing of slamming.

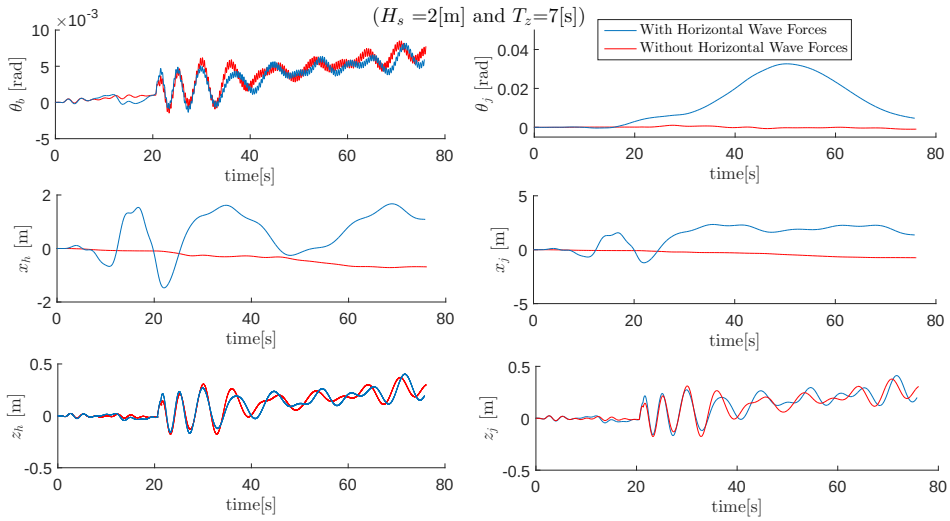

Figure 5.11: System's DOF displacements with and without horizontal wave forces

5.1.6 Summarizing

In order to summarize the contributions of each external force upon the load cable DAF, in figure 5.12, their influences are given separately. This time however this is done only switching on the force in question individually. Despite the fact that force-interactions are now not considered, this method gives an insightful overview.

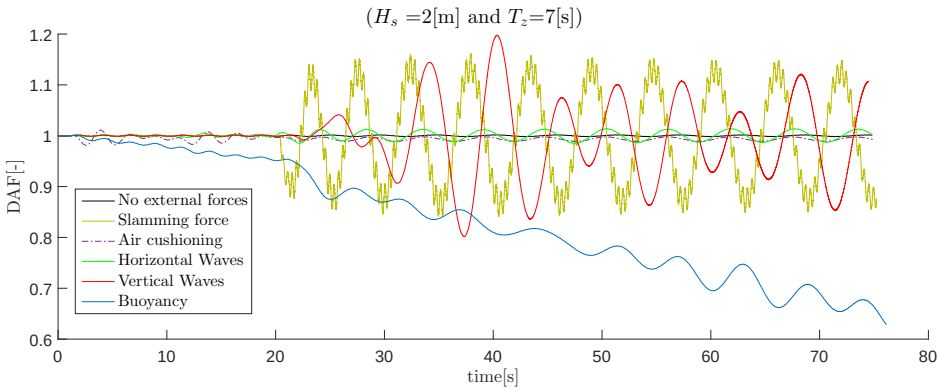

Figure 5.12: The individual influence of each of the external forces upon the load cable DAF

Again, both the influence of slamming and the vertical wave forces seem to dominate this picture, followed by the large upwards forces due to buoyancy.

5.2 Wave combination results

Up until now, the analysis is performed for one wave combination only. The scope of this thesis however is to look at each wave combination within the range of interest. Due to the fact that performing a complete study like was done in the previous section upon each of these wave combinations would introduce a large amount of work, probably with a lot of similarities in results, from now on only particular behaviour will be examined more in detail.

As a first insight in the maximum values in load cable DAF for all different wave combinations, table 5.1 is created. Calculations in order to come to this table were done using the same constant random seed for phase ($\underline{\alpha_i}$) determination. Statistically therefore, no conclusions can be drawn from these values yet.

T_z / H_s	**0.5**	**1**	**1.5**	**2**	**2.5**
4	1.190	1.395	1.598	1.932	2.113
5	1.059	1.057	1.032	1.181	1.323
6	1.031	1.052	1.125	1.175	1.224
7	1.030	1.048	1.053	1.091	1.121
8	1.025	1.010	1.001	1.042	1.113
9	1.043	1.047	1.094	1.132	1.188
10	1.046	1.094	1.163	1.231	1.299
11	1.049	1.058	1.067	1.074	1.073
12	1.044	1.046	1.044	1.038	1.030
13	1.043	1.049	1.055	1.058	1.057

Table 5.1: Maxima in DAF for different wave combinations

What is striking from this table, is that for low T_z-values, the maxima in DAF seem to exceed the 1.3 boundary, even for relatively low wave heights. This outcome is expected, since these wave periods correspond with the jacket's eigen-period as was found in section 4.5, thereby resonant behaviour is introduced. Even though the waves are irregular, looking at the JONSWAP spectrum, for a T_z of $4\ s$, the peak period is $5.12\ s$, so a lot of the harmonic waves within the irregular wave have a period in range of the eigen-period of the system with added mass, which showed to be 4 to $6\ s$.

The resonating behaviour of one of the wave combinations showing exceeding DAF values (H_s= $1\ m$ and T_z =$4\ s$) is shown in figure 5.13, in terms of the system's displacements. The vertical displacements show largely amplified amplitudes, throughout the entire installation process. In x-direction further a large offset can be found, causing the jacket to rotate around its COG quite severely too.

The combination of these displacements cause large forces in the load cable. In the blue line in figure 5.14 the according load cable DAF is plotted. As can be seen it indeed exceeds the threshold value of 1.3, indicated by the black line, multiple times.

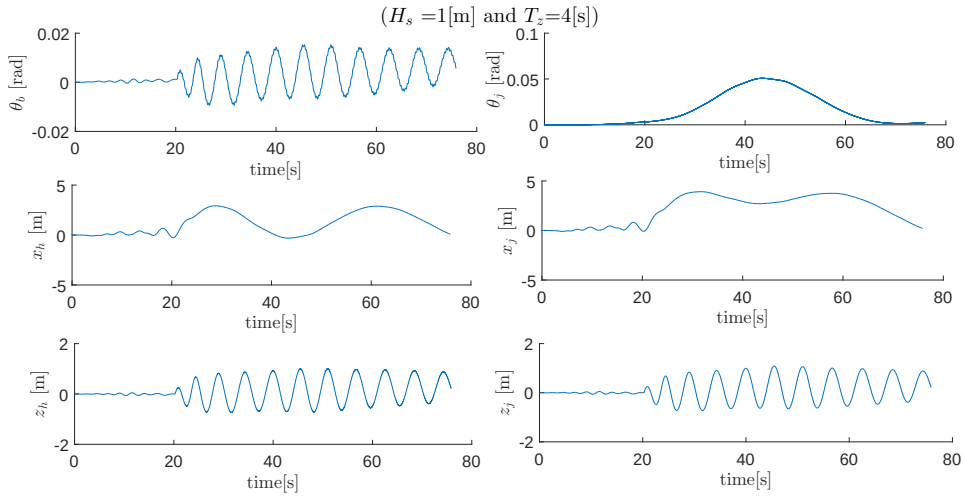

Figure 5.13: Resonating behaviour for low wave period, in DOF displacements

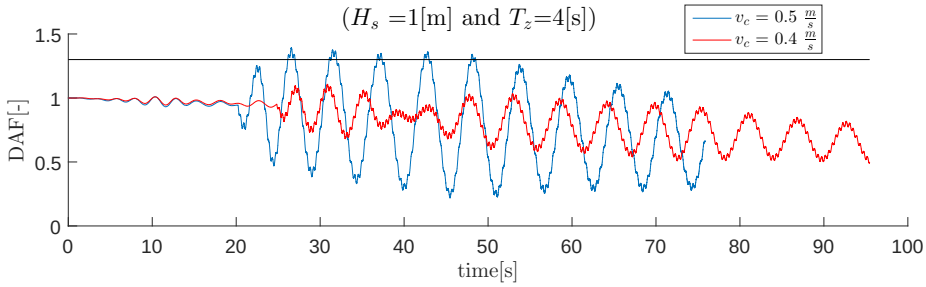

Figure 5.14: Resonating behaviour for low wave period, in load cable DAF

Out of interest several parameters have been adjusted, in order to find out whether they could reduce the force in the load cable for this specific case. When for the same wave combination the crane lowering velocity was decreased from 0.5 to 0.4 $\frac{m}{s}$, the displacements and load cable forces seemed to decrease correspondingly, as can be seen in the red line in figure 5.14. When searching for the reason behind this difference, a large distinction in slamming behaviour was observed. In figure 5.15 this is shown, in terms of vertical jacket velocity. As can be seen, the slamming

for $v_c = 0.5\frac{m}{s}$ happens almost simultaneously for both buckets, resulting in a huge jump in velocity. The velocity jump due to slamming for $v_c = 0.4\frac{m}{s}$ on the other hand is much less severe. As was discovered in section 5.1.2, slamming has quite a large impact on the system's behaviour. Therefore, it could be assumed that the discovered difference in timing and magnitude predominantly affects the results. It thus is important to mention that it can not be concluded that less high lowering velocities are better for low period waves, the influence is case specific. The fact that the outcomes are to such a large amount affected by the lowering velocity proves that the system is highly dependent on the parameters used.

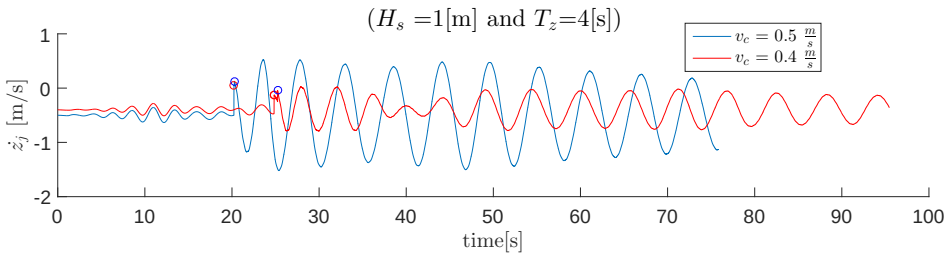

Figure 5.15: Difference in slamming for different lowering velocities

5.2.1 Monte Carlo simulations

As was stated in the previous chapter, a Monte Carlo analysis is performed, in order to be able to treat a larger set of possible irregular wave patterns per wave combination. This is needed because, as can clearly be seen in figure 5.16, different wave patterns for the same wave combinations give completely different results.

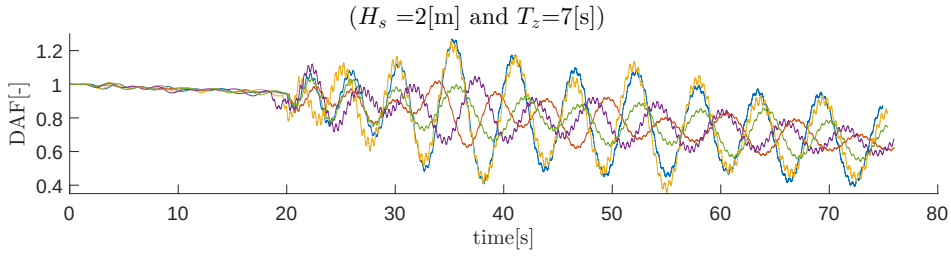

Figure 5.16: Differences in DAF, for different seeds

In a Monte Carlo analysis calculations are repeated multiple times, each time with different initial conditions, according to Kroese [27]. In this case, these conditions are determined by the phases $\underline{\alpha}_i$, which are randomly chosen between 0 and 2π and used for setting up the irregular wave. Up until now, the random seed used to determine these phases was set to one constant value. In order to determine all possible outcomes by simulating the randomness of the waves, now multiple of these seeds are to be used as an input. As an example of this, in figure 5.17 the load cable DAF maxima and minima are determined for a set of 50 different randomly chosen (uniformly distributed) seeds, using H_s of $2\ m$ and a T_z of $7\ s$. In the upper figure, the minimum DAF encountered, together with the mimimum allowed DAF of 0.1 (indicated by the black line, which approximately indicates when slack would occur) is shown and in the lower one the maximum DAF encountered and maximum allowed DAF of 1.3 are shown. It can be seen that 3 out of the 50 outcomes lie above the maximum value, which indicates that for this set of wave conditions unsafe situations could in fact occur. This proves that this analysis is very important to perform, since in table 5.1, for this exact wave combination, the DAF was only 1.091. The analysis is thus repeated for each wave characteristic combination within the range of interest.

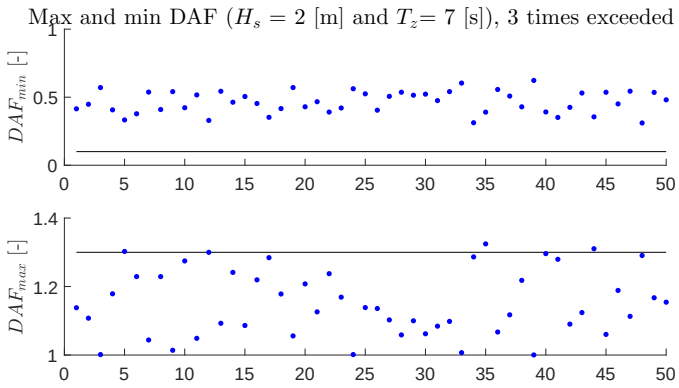

Figure 5.17: Example Monte Carlo simulation with 50 seeds

From a statistical point of view, it would be convenient to be able to predict probabilities of occurrences of DAFs to exceed 1.3. In order to be able to use probability distributions to do so, the output is required to be distributed accordingly to one of such distributions, e.g. the normal- or log-normal- distribution. In order to find out whether one of such probability distributions could be fitted, in figure 5.18, a his-

togram of the maximum DAFs found in the previous example is made. Using a built in tool in MATLAB, existing distribution functions can be fitted to this histogram. Unfortunately, none of the mentioned distribution functions fits properly (neither does any of the other existing distributions). Even when considering a larger number of seeds (100), no proper fit could be found.

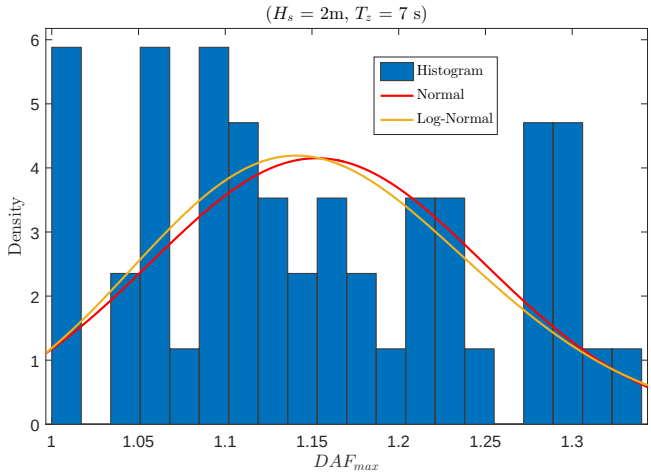

Figure 5.18: Maximum DAF histogram

With this in mind, the question arises how to decide when to- or not to install in certain wave conditions, based on the results of the model. It could in general be decided not to work with a certain wave combination when at least one of the seeds shows a DAF above the threshold value. The question then arises: how many seeds should be used in order to get a clear view on this?

In figure 5.19 three different Monte Carlo Simulations with three different numbers of seeds have been performed: respectively 15, 50 and 100. As can be seen, all of these analysis show at least one exceeded value. However, as was expected, the percentage of these occurrences is not stable over these three.

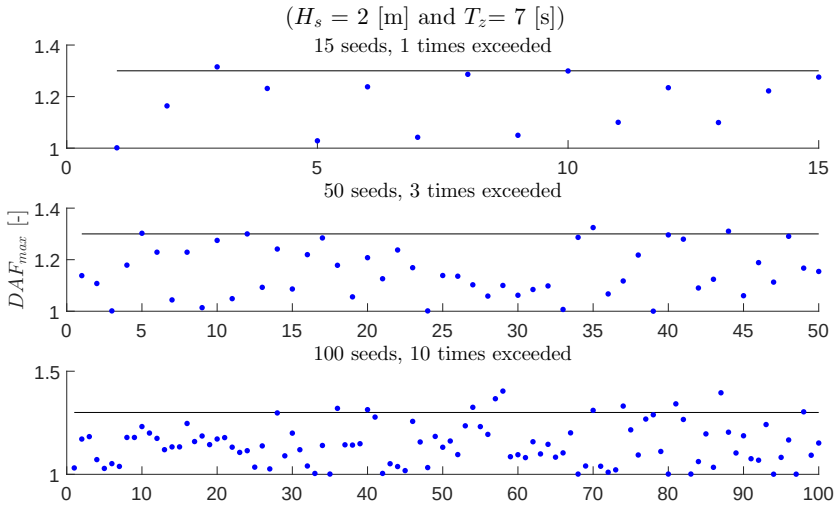

Figure 5.19: Different results for different number of seeds

Jacobsen et al. [23] performed a comparable study, containing statistical comparison of time-domain simulations with full-scale force measurements. In his research he concluded that a total set of 15 runs with different random seeds were sufficient when comparing maxima or minima in DAF. When 15 seeds were used for the same wave combination as before, the DAF once exceeded 1.3, as can be seen in figure 5.19. However, due to large unpredictability caused by slamming, which was not the case in Jacobsen's research, for this thesis it is chosen to use 50 seeds for the wave combinations which beforehand are considered to bring interesting results: for all combinations with H_s of $2\ m$ and higher and for those with a T_z in the range of the eigen-period. All remaining wave combinations of interest have been tested with a set of 15 seeds. Higher numbers of seeds are not desirable, since computational time for each individual seed takes approximately 5 minutes.

In table 5.2 and 5.3 the results of this study are given. The tables respectively state the amount of simulations that showed a DAF exceeding 1.3 and the amount of simulations that showed slack (in accordance to equation 2.10). The '$/50$' indicates that a total of 50 seeds are used and '$/15$' means 15 different seeds.

T_z / H_s	0.5	1	1.5	2	2.5
4	0/50	13/50	32/50	44/50	13/15
5	0/15	2/50	9/50	28/50	14/15
6	0/15	0/15	5/50	10/50	9/15
7	0/15	0/15	0/50	3/50	12/50
8	0/15	0/15	0/15	0/50	6/50
9	0/15	0/15	0/15	0/50	0/50
10	0/15	0/15	0/15	0/50	0/15
11	0/15	0/15	0/15	0/50	0/15
12	0/15	0/15	0/15	0/50	0/15
13	0/15	0/15	0/15	0/50	0/15

Table 5.2: Nr. of simulations with DAF > 1.3

T_z / H_s	0.5	1	1.5	2	2.5
4	0/50	1/50	5/50	6/50	10/15
5	0/15	0/50	0/50	18/50	9/15
6	0/15	0/15	0/50	0/50	7/15
7	0/15	0/15	0/50	0/50	1/50
8	0/15	0/15	0/15	0/50	0/50
9	0/15	0/15	0/15	0/50	0/50
10	0/15	0/15	0/15	0/50	0/15
11	0/15	0/15	0/15	0/50	0/15
12	0/15	0/15	0/15	0/50	0/15
13	0/15	0/15	0/15	0/50	0/15

Table 5.3: Nr. of simulations with slack

Again, low wave periods induce large forces in the load cable, due to the fact that they act within the eigen-period region of the crane and its rigging with added mass. In addition, for higher H_s values, higher chances of exceeding DAF values or slack are observed. However, it seems that for a H_s of $2\ m$, combined with a T_z of at least $8\ s$, the criteria sketched were satisfied. This would mean that installation could still safely be performed for these wave conditions, looking at the criteria sketched.

5.2.2 Result analysis

In the remaining of this section several of the more particular outcomes in the studied wave combination results are explained more elaborately. With the knowledge gained in section 5.1, the analysis of certain jacket behaviour can more easily be linked to individual force contributions. By analysing more cases, more insight in the contributions and interaction of the individual forces can be gained.

DAF remaining below 1

The first particular observation is that for some combinations of wave characteristics the DAF seems to not exceed 1. This physically indicates that the dynamic upward forces dominate over the static force in the load cable. In other words, the jacket constantly is being lifted up to such an extend that the stretched length of the load cable remains below its pre-tensioned stretch. Several of these cases have been studied and an example is given in figure 5.20. More examples can be found in appendix K.

The cases that were studied all seem to have one thing in common, which can clearly be seen in this example too: the slamming on the second- (in this case left-)

bucket is timed such that the oscillation of the jacket, caused by the first slamming, is mostly cancelled out. While the jacket is pulling more and more at the cable, it gets hit upwards again in such a fashion that it does not have the chance to fully oscillate in the cable. Even though the magnitude of the first slamming is quite severe, and the wave period is closely within range of the vertical eigen-period of the system, this effect causes the forces in the load cable to be relatively low. This shows that the timing of the slamming has quite a large influence on the system.

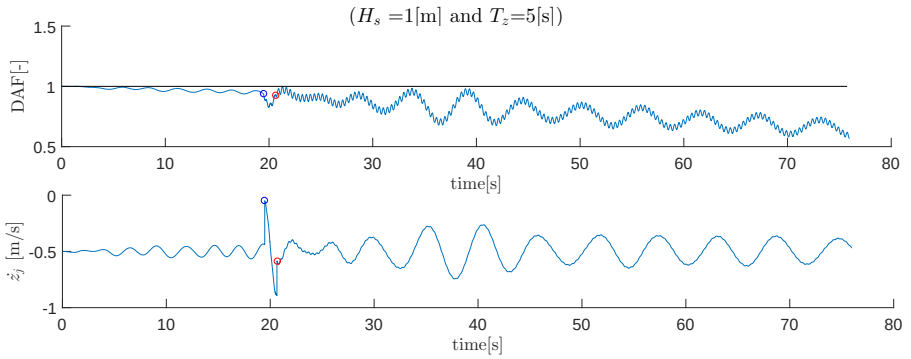

Figure 5.20: Case where DAF remains below 1

DAF exceeding 1.3

When cases are studied for which the DAF exceeds its threshold value of 1.3, the effect of slamming seems to often initiate this problem. Multiple cases that showed such an surpassing, with wave periods out of range of the system's vertical eigen-period, have been studied. Most of them could be linked to either the timing- or the magnitude of the slamming.

With the analysis performed in section 5.1.2 in mind, it is known that the slamming induces the jacket to oscillate in the rigging. From that moment on the buckets are submerged and the vertical waves have a large area to act upon. Since these vertical waves excite a forcing that follows the wave kinematics, the timing of the slamming could be essential for the phasing of the oscillation of the jacket with the waves: when both oscillations occur in the same phase, the vertical wave forces will add more energy to the oscillation than in case both oscillations occur in different phases.

In order to visualise this phasing effect, in figure 5.21 the vertical displacement of the jacket is given, in case vertical forces with different phases are introduced to it. This simulation is ran with the jacket having an initial vertical displacement of $+0.1\ m$ and with it being lowered with $0.5\ \frac{m}{s}$. At the 20^{th} second a co-sinusoidal vertical force is added to the system, with a magnitude of $\frac{1}{3}^{rd}$ of the jacket weight and a period of $4\ s$ (chosen within range of the eigen-period of the system). The added masses used in the model are in this case still incorporated, in order to create the same eigen-periods as were found in section 4.5. All other forces are switched off.

As can clearly be seen, the phase this force has to quite a large extend affects the amplitudes that are reached in the vertical oscillation. Going back to the situation with all forces incorporated, this phasing can directly be translated to the time the oscillation of the jacket in the crane starts, as a result of slamming. The timing of the start of this oscillation is essential for the remaining part of the installation. In other words, the timing of the slamming is of the essence for this phenomena too.

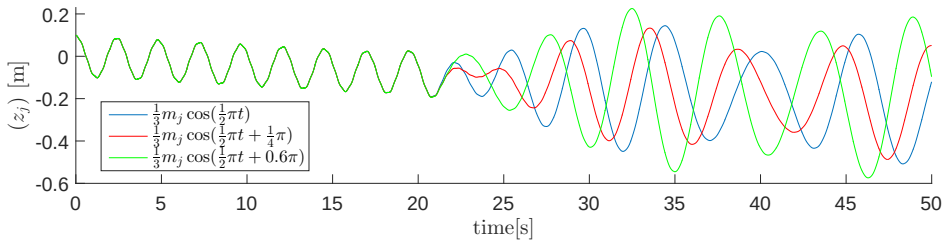

Figure 5.21: The effect of phasing

An example of a case where the vertical wave forces add energy to the system is given in figure 5.22. Here a case that showed exceeding DAF values is studied, by switching the vertical wave forces on and off. The blue respectively red line represents the jacket's behaviour found with and without the influence of vertical wave forces. Where the previous example in figure 5.7 in section 5.1.3 showed that the vertical wave forces subtracted energy from the system, here it clearly does the opposite. Especially in the second, third and fourth oscillation, between the 25^{th} and 40^{th} second, the amplitude with vertical wave forces shows large amplifications. This indicates that in this region the vertical wave force periods are synchronised with the jacket oscillation.

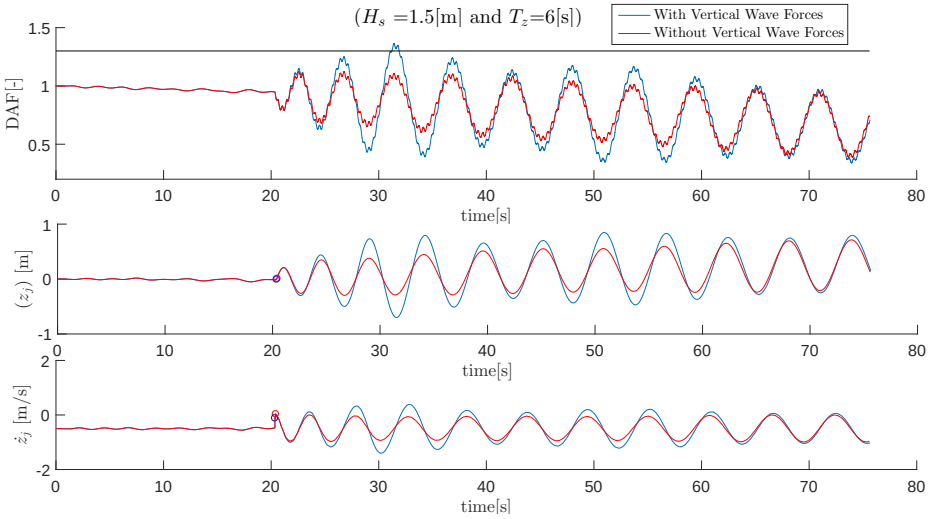

Figure 5.22: Case where vertical wave forces add energy to the system

In figure 5.23, the influence of the vertical drag- and inertia term for this case are studied separately. This time, the drag term seems to have a higher contribution than was observed in figure 5.8. The drag in this case subtracts energy from the system and the inertia adds energy. The period of the oscillation now is not adjusted by the either of the vertical wave forces.

The fact that this case shows more drag influence than was observed before, is caused by the fact that the drag- and inertia term are $90\ deg$ out of phase. The drag term is in phase with the velocity and the inertia term with the acceleration. An example in which this phase difference between the two terms can clearly be seen is given in figure 5.24. It seems that for cases that are inertia dominated, the oscillation periods grow faster than cases that are affected by drag too.

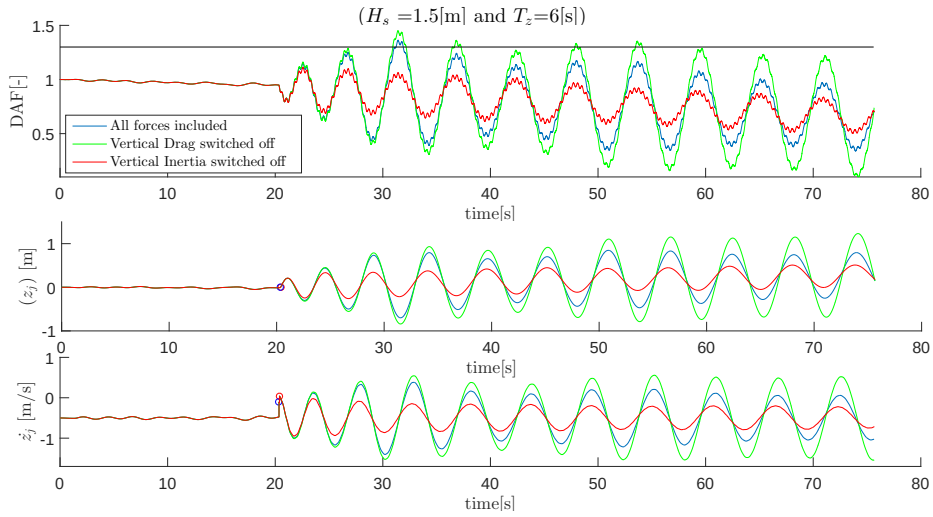

Figure 5.23: Vertical wave forces: drag versus inertia

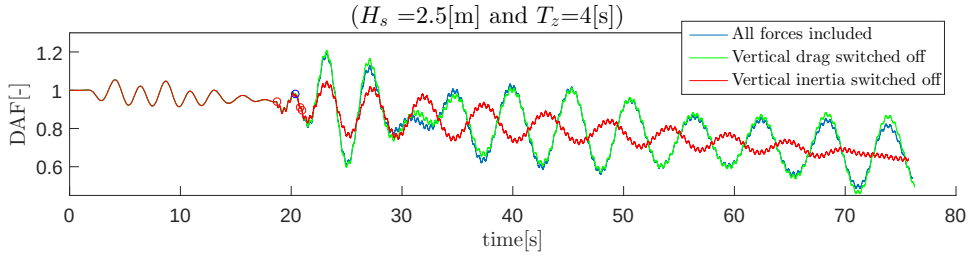

Figure 5.24: Influence of phase difference between vertical drag- and inertia terms

Another way to show the importance of the phasing of the jacket oscillation with that of the waves is by adjusting the eigen-period of the crane and its rigging. As was explained in section 4.5, this can be done by switching off the influence of added mass. The result of this study is shown in figure 5.25. As can immediately be seen, the jacket in this case oscillates in the rigging eigen-period as was found in chapter 3, which is way lower than that of the waves. The jacket's vertical displacements therefore are to a way smaller extend amplified by the vertical wave forces and the load cable DAF does not at all reach high proportions.

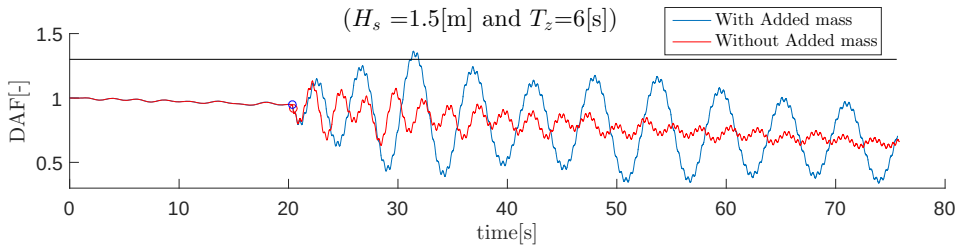

Figure 5.25: The effect of added mass, on the load cable DAF

What further can be seen in figure 5.22, is that slamming on both buckets in this case happens almost simultaneously. In order to show the importance of the magnitude of this jump, the same simulation is done without slamming. The difference between these two cases is shown in figure 5.26. This slamming magnitude results in larger amplitudes, resulting in an intolerable DAF value. It further shows that the slamming indeed is timed exactly such that the jacket- and vertical wave oscillation are in phase. In case slamming would not be considered, the jacket will oscillate in phase with the waves, since these forces now are the ones that induce the oscillation in the crane. In the simulation without slamming considered, this indeed seems to be the case.

In appendix K, three other cases are discussed, first of which shows another example where slamming on both buckets happens simultaneously, the second shows a case where slamming has taken place multiple times and the third shows an extreme slamming magnitude. For all cases the DAF and vertical velocity of the jacket are plotted with and without slamming involved, in order to study its influence. It again showed that the magnitude and timing of slamming can really initiate DAFs exceeding 1.3.

Slack line

Lastly, for some of the more extreme wave characteristics, the oscillation of the jacket reaches such large proportions that slack is encountered. An example of one of these cases is given in figure 5.27. Like was shown in section 3.6, once slack occurs, the line becomes non smooth, due to loss of load cable tension. Since the load cable behaviour is not properly modelled by a discretized fashion for this situation, the results become erroneous.

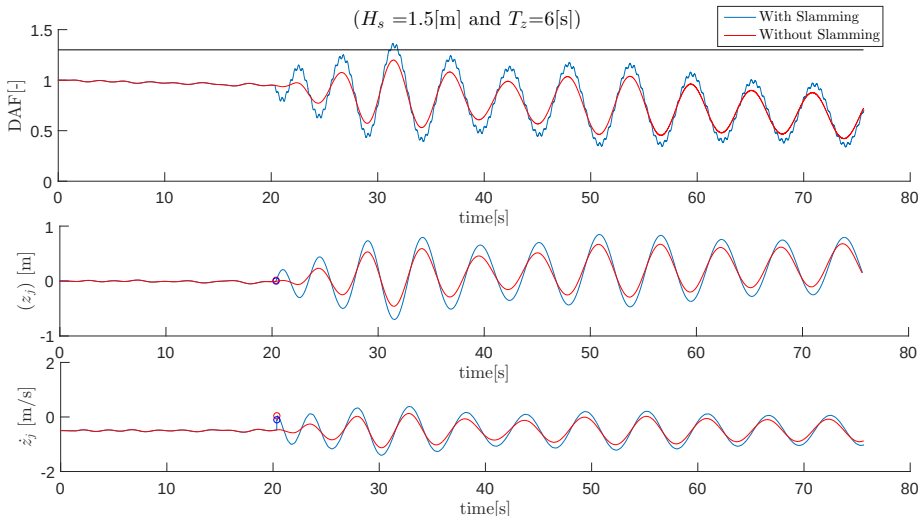

Figure 5.26: The effect of simultaneous slamming

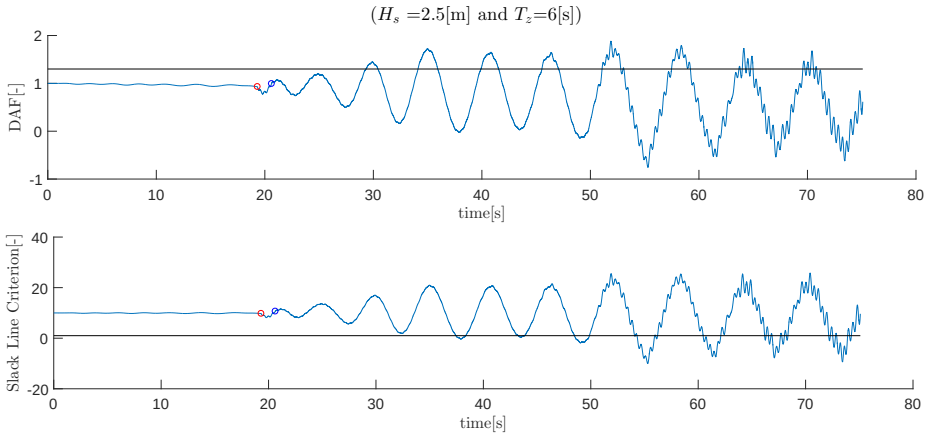

Figure 5.27: The effect of slack

5.3 Worst case scenario

In the previous sections it has been shown that the behaviour of this particular jacket design in irregular waves is hard to predict. The usage of 50 seeds in a Monte Carlo simulation showed that no proper statistical prediction can be made in the determination of the probability of occurrence of non satisfaction of the sketched criteria. Further analysis showed that the slamming, both in timing and in magnitude affects the results. It would therefore be beneficial to be able to determine a worst case scenario, in order to be able to find wave combination specific recommended installation procedures. In this section, an effort is made in order to find a worst case scenario, in terms of slamming, for waves with a H_s of $2\ m$ and a T_z of $7\ s$.

Since it is known that slamming primarily depends on the relative velocity between the jacket and the water, knowing these terms would make one able to predict the slamming magnitude. The downward velocity of the jacket prior to slamming is approximately equal to the lowering velocity of the crane (apart from small vertical jacket displacements due to crane elasticity, its horizontal displacements, and from the effect of the air cushion). The maximum relative velocity thus occurs when the upward velocity of the water is maximum. This velocity is a parameter that can be determined using the orbital velocities of the water particles, as was discussed in 2.2.

According to You in 2009 [48], the amplitude of the vertical wave velocity for oceanic waves follows a modified Rayleigh- or Weibull distribution. This distribution is formed by considering multiple sets of randomly chosen seeds for phase-determination. This time the random phases are used to calculate maxima in vertical wave particle velocities. In order to check whether the Weibull distribution indeed fits the results, a study is performed for a 300 second irregular wave, consisting out of 100 frequencies. The 300 seconds are chosen here due to the fact that in this period of time the wave pattern starts to repeat itself, which indicates that all possible velocities for this irregular wave are encountered. A total set of 50 different simulations are performed, for each of which the maximum vertical wave velocity is saved and used as an input for the Weibull distribution.

In figure 5.28 the results of this study are shown. The Weibull shows quite a nice fit through the results. A side-node for this figure is that, in order to be able to fit the Weibull distribution using a built in MATLAB distribution fit tool, the data should start at zero. The minimum calculated maximum vertical velocity therefore was subtracted from the output. The actual numbers are in fact $0.79\ \frac{m}{s}$ higher.

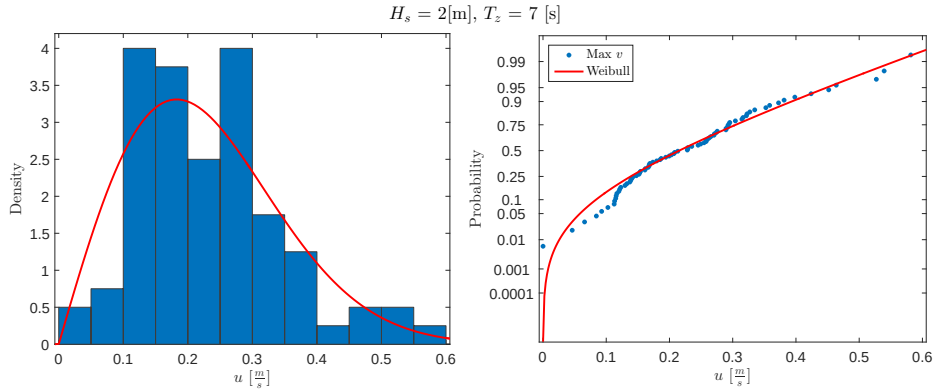

Figure 5.28: Maximum vertical velocity distribution

The formula that according to You best describes the distribution, in terms of exceedence probability Q_p, is given in equation 5.1a. According to him, this 0.96 factor shows best results in the tail of the distribution. The difference between this function and the one used by MATLAB (without the 0.96 factor) is shown in figure 5.29. The results gained by MATLAB show somewhat more conservative numbers in the tail, but apart from that, the differences can not clearly be seen. Due to the fact that You has performed this research using more seeds than was done here, it is chosen to follow his recommendation and use his formulation of Q_p. The formulation for the root mean square further is provided in equation 5.1b, where n are the amount of seeds chosen.

$$Q_p = \exp(-(\frac{u}{0.96u_{rms}})^2) \tag{5.1a}$$

$$u_{rms} = \sqrt{\frac{1}{n}(u_1^2 + u_2^2 + ...u_n^2)} \tag{5.1b}$$

Knowing the function for Q_p, a prediction can be made on maxima in vertical wave velocities, in order to determine the worst case scenario for the slamming magnitude. When taking the 1 % probable value for the discussed case, a vertical velocity of $0.54 + 0.79 = 1.33$ $\frac{m}{s}$ is found for this specific wave combination. The next step is to implement this extreme value into a simulation that uses the same wave parameters.

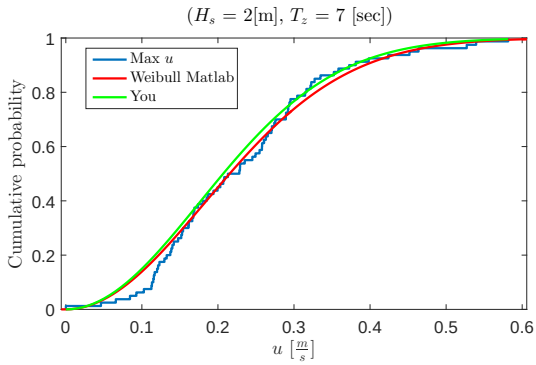

Figure 5.29: Cumulative probabilities MATLAB versus You [48]

Since the maximum upward wave velocity is considered to bring maximum slamming forces, and vertical water acceleration and velocity are always 90 degrees out of phase, the slamming will in this case always take place when the vertical wave acceleration passes 0 in a downward fashion. By the assumption made, the timing of the slamming with respect to the waves is thus fixed. In figure 5.30 the results of this worst case scenario are given. It is directed such that both buckets slam almost simultaneously, one of them with the maximum found vertical velocity of 1.33 $\frac{m}{s}$.

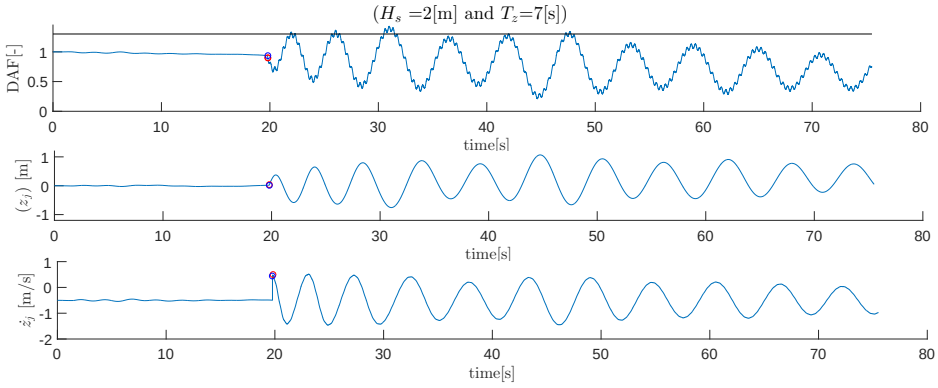

Figure 5.30: Results of worst case slamming scenario

For this worst case scenario, the outcomes of installations using different (constant) lowering velocities have been compared with each other, in order to find out whether there is a velocity for which the DAF does not exceed 1.3. Three of these velocities are shown in figure 5.31. In the bottom figure, which shows the vertical jacket's COG velocity, the effect of the relative velocity can clearly be seen: the higher the lowering velocity chosen, the higher the relative velocity and the higher the amplitude of the jump. It therefore seems that for this specific case, a lowering velocity of $0.3\ \frac{m}{s}$ would result in the DAF to remain below its maximum allowable value. Its lower slamming magnitude results in smaller vertical jacket displacements and load cable forces.

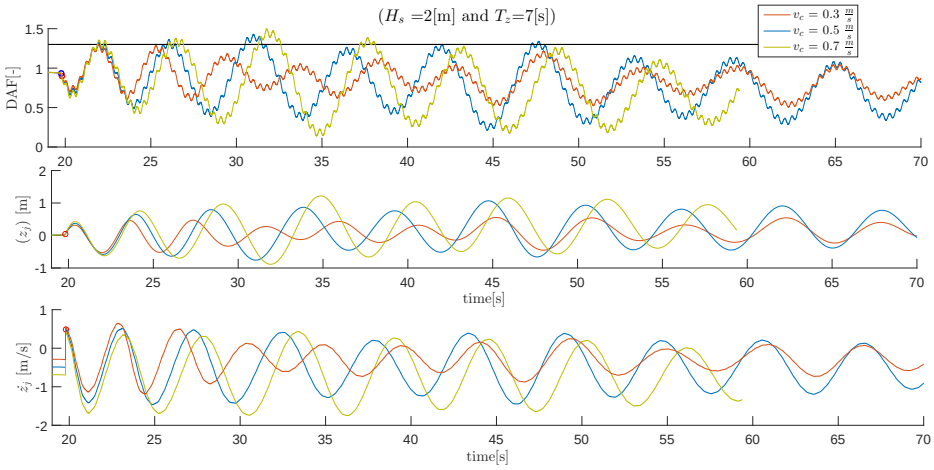

Figure 5.31: The effect of the lowering velocity in the worst case scenario

Even though the DAF in the worst case scenario for these wave conditions does not exceed 1.3, when a lowering velocity of $0.3\ \frac{m}{s}$ is used, this does not imply that this should always be chosen to be the velocity for these wave combinations. Even though this case is worst case in terms of slamming -magnitude, -simultaneity, and -timing, the subsequent wave behaviour still has a huge influence on the remaining part of the installation. For instance, the conditions in this case are such that this velocity of $0.3\ \frac{m}{s}$ does not induce multiple slamming. When for this specific case the subsequent wave pattern would be slightly different though, this could in fact occur, resulting in totally different behaviour post first slamming. Phasing further could take place in different stadia of the installation, depending on the velocity of the

crane and the wave kinematics. In the example it can be seen that amplification due to synchronisation with the waves occurs in a later stadium for $v_c = 0.3\ \frac{m}{s}$, which could be explained by the fact that for this specific lowering velocity the buckets are positioned in wave affected regions for a longer period of time. This means that the synchronisation-sensitive time period is longer. Even though this specific case is not highly affected by this phenomenon, other cases could show opposite behaviour.

It thus still is not decent to draw conclusions from this specific worst case scenario. Even though the initiation of the jacket displacements in this case is taken to be absolutely worst case, the remaining part of the installation could still show totally different behaviour and possibly result in way higher oscillation amplifications. Even though this study showed that low lowering velocities are beneficial in terms of minimizing the relative velocity between water and bucket and thus slamming magnitude, the synchronisation-sensitive time period and the chance on multiple slamming increases.

5.4 Higher amount of seeds

The study in the previous section showed that it is difficult to model a worst case scenario, and in the section prior to that it was found that a total of 50 seeds showed no recognisable distribution in the DAF maxima. So far no thorough conclusions can thus be drawn. In order to figure out whether a certain known distribution could be fitted, it is therefore required to go back to the Monte Carlo simulation and use more seeds. Since it would require too much time to do so for each of the wave combinations, only one combination is analysed: $H_s = 2\ m$ and $T_z = 7\ s$. Such a wave is chosen since its period is not within the jacket's eigen-period, but it did show exceeding DAF values in the previous sections.

In order to be able to conduct this study without spending too much computational time, the model is adjusted slightly. Firstly, the entire installation phase is shortened: only the first $25\ m$ submergence is taken into account, since in the previous sections most of the exceeding DAF values were observed prior to this number. Further, only 50 wave frequencies are considered in the JONSWAP spectrum, in stead of the 100 frequencies used before. Lastly, a different ODE solver is used in MATLAB: the 'ODE23' solver now is used, which is quicker, but has a lower accuracy than the 'ODE45' solver used in the previous calculations. Comparing the results found for both of these solvers however does not show much difference.

With these adjustments, the total time to solve one seed is reduced from approximately 350 to 80 s (on a 2.6 Ghz dual core computer), which allows a larger set of seeds to be researched. A study with a total amount of 2000 seeds is performed, and the results gained are shown in figure 5.32. As can be seen in the histogram of the maximum observed DAF values, in the right side of the figure, the Weibull distribution can now be fitted. Likewise for the Weibull fit in the previous section, in order to be able to fit the Weibull distribution using the built in MATLAB distribution fit tool, the data should start at zero. The actual maximum DAF numbers are in fact 1 higher.

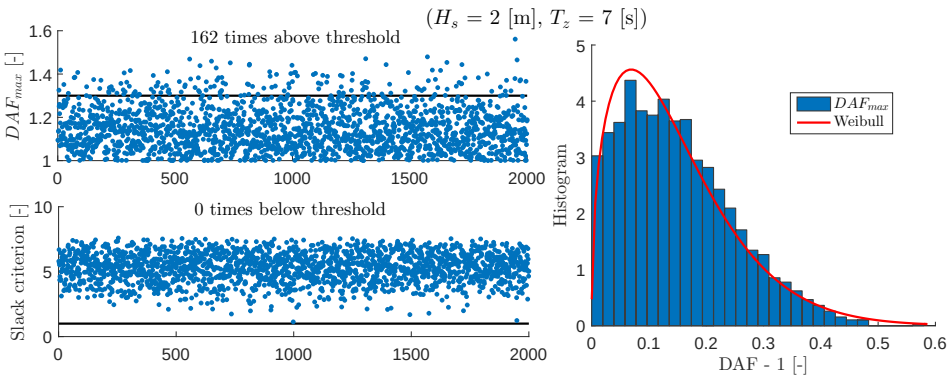

Figure 5.32: Monte Carlo simulation with 2000 seeds

Now the distribution is known to be Weibull, the chance on exceeding DAF values can easily be calculated, by making use of the cumulative probability. Doing so for this specific case, a 8.94% chance on DAF values of 1.3 or higher is found, respectively with an upper- and lower 95% confidence bound of 7.95% and 10.00%, corresponding with an error of 1.09%.

For further studies it is beneficial to know what amount of seeds is to be used in order to achieve statistically profound results. This can be done by deleting some of the results found with 2000 seeds. For six different amounts of seeds this is done, with the results shown in figure 5.33. Here, the cumulative probability functions for seeds between 50 and 2000 are plotted (solid lines), combined with the corresponding 95% confidence boundaries (dashed lines). As can be seen, higher amounts of seeds show less confidence error.

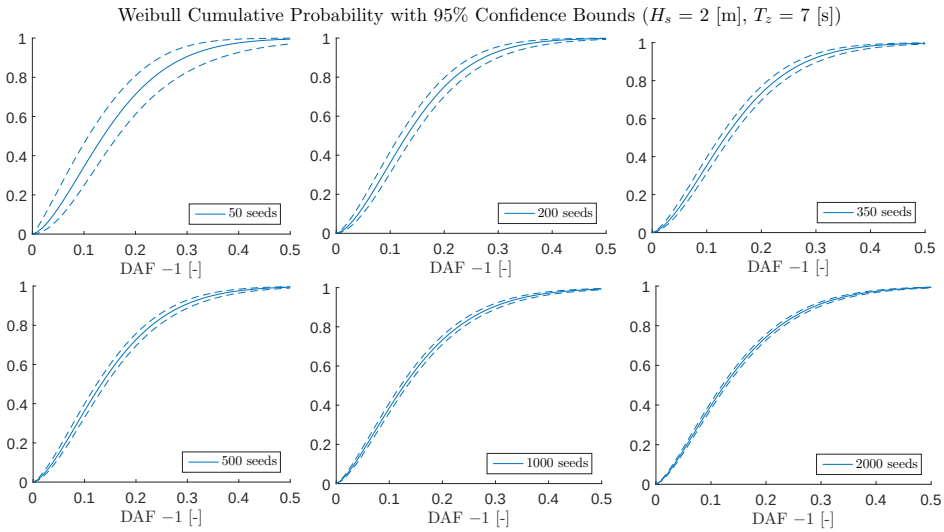

Figure 5.33: Number of seed determination

In order to show the difference for DAF values exceeding 1.3, table 5.34 shows the probability of exceeding DAF values for these numbers of seeds, together with its upper and lower 95% confidence boundaries, and the error herein. Figure 5.35, which is positioned next to the table, shows the observed errors, with an approximate fit through these points. The amount of error found thus follows an almost asymptotic line, indicating that much more seeds than 2000 will not necessarily give much better results.

Even though the error is quite large when 50 seeds are used, it is interesting to have an approximation of the probability of intolerable DAF values for all wave combinations of interest. The results found in table 5.2 therefore have been used in combination with the Weibull characteristics in order to calculate these probabilities, together with the 95% confidence upper- and lower bounds. The results are given in appendix L.

# seeds	Probability DAF ≥ 1.3	Upper bound	Lower bound	Error
50	9.42%	17.35%	4.14%	5.83%
100	7.95%	12.93%	4.36%	3.90%
200	6.83%	9.99%	4.38%	2.63%
350	7.86%	10.46%	5.85%	2.28%
500	9.05%	11.26%	7.11%	2.13%
750	9.54%	11.36%	7.90%	1.81%
1000	9.44%	11.00%	8.02%	1.57%
1500	9.27%	10.52%	8.11%	1.28%
2000	8.94%	10.00%	7.95%	1.09%

Figure 5.34: Chance on DAF exceedence per number of seeds

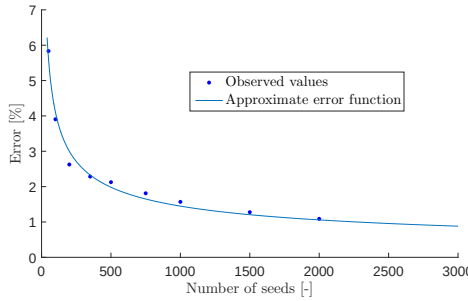

Figure 5.35: Error decrement

5.4.1 Lowering velocity

As was briefly done in the previous section, a small study can be conducted on the effect of the lowering velocity upon the probability of exceeding DAF values. From figure 5.31 it seemed lower velocities are beneficial in the reduction of load cable forces. On the other hand, as was also stated in that section, the synchronisation-sensitive time period and the chance on multiple slamming increase for these lower velocities. Now it is known that the maximum DAF values are Weibull distributed, and that errors can be reduced for a larger amount of seeds, the probability of DAF values exceeding 1.3 can be determined for different lowering velocities. Since a large number of simulations are performed, situations with synchronisation and multiple slamming are better incorporated in the results.

The study is performed for lowering velocities between 0.2 and 0.9 $\frac{m}{s}$, with increments of 0.1 $\frac{m}{s}$. Per lowering velocity, 1000 simulations are done. This number is chosen since the accompanied computational time in combination with the error of 1.57% is accepted. The small reduction in error for increased numbers of seeds does not weigh up to its growth in computational time. For v_c of 0.5 $\frac{m}{s}$, 1000 and 2000 seeds respectively take 9 and 18 hours. This number increases for smaller lowering velocities, since calculations are performed until the jacket is submerged 25 meters.

The results gained are shown in figure 5.36, merely in terms of maximum DAF values, since non of the simulations showed slack. In the left figure, the probability of DAF exceeding 1.3 is plotted (solid line), together with the accompanying 95% confidence bounds (dashed lines). In the right figure, the total amount of different numbers of slamming encountered is plotted, in percentage of the 1000 simulations (in a situation where both buckets slam only once, this number is 2). The individual Weibull cumulative probability plots are given in appendix M.

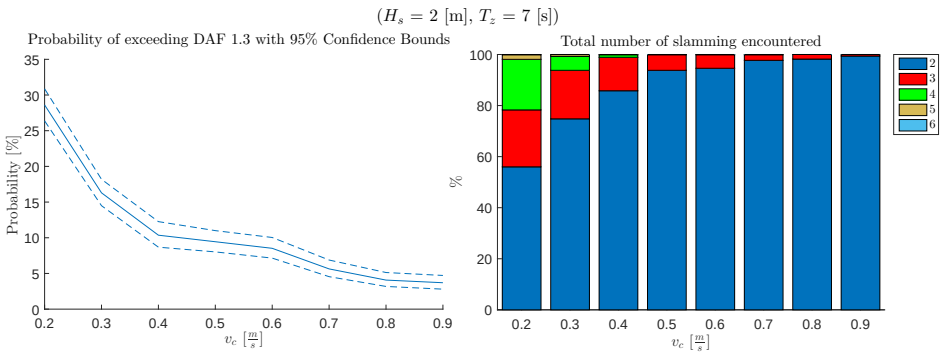

Figure 5.36: Lowering velocity analysis

Smaller lowering velocities indeed result in a higher chance on multiple slamming to occur, and, more too high DAF values are encountered for these lower velocities. One might thus assume there is a correlation between multiple slamming and exceeding DAF values. However, this assumption shows not to be true: for a v_c of 0.2 $\frac{m}{s}$, only 127 out of the 283 exceeded simulations have experienced multiple slamming. For v_c of 0.3 $\frac{m}{s}$, this number is 48 out of 167.

Looking for the reasoning behind the relation between the lowering velocity and high load cable forces, some of the DAF plots of extreme simulations are studied (some of which can be found in appendix M). Like was observed in most of the cases discussed in the previous sections in this chapter, the highest DAF values occur primarily in the regions where the bucket tops are within reach of the vertical wave kinematics. As stated in the previous section, the synchronisation-sensitive time period is significantly larger for lower lowering velocities. This indeed seems to be the reason that for these velocities the probability of intolerable DAF values is higher.

The probability of exceeding values thus decreases for increasing lowering velocities. Since the synchronisation-sensitive time period is significantly lower for these velocities, its dependency on the jacket's vertical oscillation, initiated by slamming timing and magnitude is more important. Since this system depends on more variables and interactions, the probability of exceeding DAF values decreases: it seems to be ideal to use high lowering speeds. However, it should be noted that larger relative velocities encountered at these higher values induce larger impacts upon the bucket tops. The stresses that result from these impacts are not considered in this study, but should definitely be taken into account when choosing the ideal lowering velocity.

5.5 Analysis summary

In this chapter an analysis of the results gained with the model is performed. Firstly, the individual influences each of the forces described in the previous chapter have upon the jacket behaviour in the crane are studied.

The added mass influences the frequency in which the jacket oscillates: once the buckets are in the water, the eigen-period found in chapter 3 grows extensively from $2.5\ s$ to a maximum of $6\ s$. This affects the installation procedure, since some of the wave periods within the range of interest are of the same magnitude.

It further was observed that slamming influences the subsequent jacket displacements, since the jump in velocity it results in initiates the jacket to oscillate in this eigen-period. The magnitude of the relative velocity between the bucket in question and the water determines the amplitude of this oscillation and more importantly, its timing could induce synchronisation with some of the wave components of the irregular wave. The vertical wave forces in this case will enforce the vertical oscillation amplitude of the jacket, which directly is linked to the forces in the load cable. Lastly, the independent timing between slamming on the left and right bucket could either cancel out- or enforce the oscillation amplitude.

Since the system depends on the interaction of multiple phenomena, it is very complex to predict jacket behaviour for different wave conditions. It seemed impossible to find worst case scenarios, so in order to take the randomness of the waves into account a Monte Carlo simulation is required. In order to be able to find results for all wave combinations of interest, 50 seeds were used as an input for particularly interesting combinations and 15 for the remaining ones. Even though no statistically profound conclusions can be drawn from the results acquired, an insight is gained in wave combinations that should be handled with extra care. Those with a T_z of 4 to $5\ s$ showed resonant behaviour, un-acceptable slack and intolerable load cable DAF values. For H_s of $2\ m$, wave periods lower than $8\ s$ showed intolerable DAF values.

In order to obtain statistically profound results, a larger set of seeds was required in the Monte Carlo simulation. By using 2000 seeds it showed that the maxima in DAF follow a Weibull distribution. With this knowledge the probability of intolerable DAF values can be calculated. For waves with a H_s of $2\ m$ and a T_z of $7\ s$, this showed to be 8.94%, respectively with an 95% confidence upper- and lower bound of 10% and 7.95%.

Lastly, the Weibull distribution characteristics are used in a brief parameter study on the crane lowering velocity. This study showed that the dependency on slamming decreases for decreasing lowering velocities. The probability of intolerable DAF values therefore is lower when the jacket is lowered with a higher velocity.

Chapter 6

Discussion & recommendations

From the analysis performed in the previous chapter the system showed to be very hard to predict. A lot of individual forces influence both the jacket's behaviour and each other. Per wave combination a large set of simulations should be performed in order to maximize accuracy in statistical analyses. As was briefly done in the previous chapter, such analyses can be used in parameter studies, to create ideal case specific installation procedures. More insight can be created in how to respond on behaviour encountered during installation. Since such a study would require a lot of time and effort though, it is beneficial to improve the model in advance; the fact remains that a model by definition is a simplified description of real phenomena.

In order to improve further analysis on accuracy, some of the assumptions made in this research should be re-examined and maybe incorporated differently. The model as it is now can be used as a first iterative step in this process. As a recommendation for these further studies therefore, in the remaining of this chapter the biggest assumptions made are enlightened an put up for discussion.

Firstly, in section 6.1 it is recommended to look at more criteria than those examined in this research. Recommended model accuracy improvements are mentioned in section 6.2 and in section 6.3 several additional forces and influences that should be added in case other criteria are used are discussed. Some optional design adjustments in both the rigging- and jacket design are discussed in section 6.4 and lastly the option is given to look at floating vessels, in section 6.5.

6.1 More criteria

In this thesis, only two criteria are tested, as explained in section 2.3. In practice though, more criteria are to be satisfied in order to be able to safely operate. Other examples of such extra criteria would be the maximum allowable horizontal distance the jacket drifts off, or the angle in which the crane-wires are forced into (which could be in both x- and y-direction). Both these criteria are influenced by completely different factors than were researched in this thesis, the x-directional forces here will have the predomination. In this case the high period waves will probably show more intolerable results than the lower ones, since such waves contain a lot of energy and displace a lot of water, according to Holthuijsen [20].

In figure 6.1 an example of the results of waves with $T_z = 13\ s$ is given, in terms of load cable DAF and horizontal jacket displacement (x_j). As can be seen, the DAF remains nicely below its maximum allowed value, but the jacket does drift off up to $6\ m$ in horizontal direction.

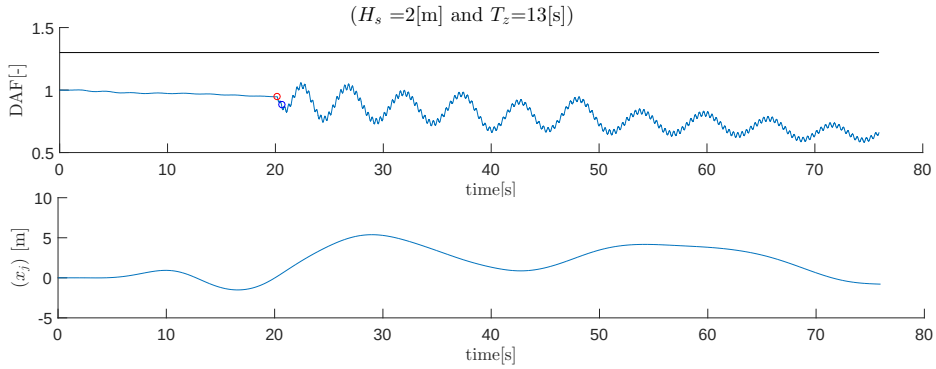

Figure 6.1: Horizontal drift off, for swell waves

As was mentioned in section 5.4.1, another criteria should be the stresses within the jacket during the installation. In this thesis, the jacket is modelled as a rigid structure and no stresses have been calculated. Especially the large relative velocities involved in the slamming however will produce large peak stresses upon the bucket tops. From a phone conversation with an SPT Offshore employee, it showed that suction buckets are designed for pressures corresponding to the water depth they are installed in, combined with additional frictional pressures. For the buckets that are used in this thesis, this would be approximately 4.5 to $5\ bar$. The pressures

accompanied by the installation should be below this threshold value.

In order to use the model to make real decisions in determination whether installation could take place in certain conditions amongst others these criteria should be considered.

6.2 Accurate modelling

In terms of modelling, a lot of assumptions have been made in the simplification of geometries, forces and in the reduction of computational time. These assumptions do have an effect on the accuracy of the results gained. More comprehensive modelling will show results closer to reality. In this section, some of the modelling assumptions that are expected to have the largest effect are discussed:

6.2.1 3D versus 2D modelling

The largest assumption made in this thesis is that the model is created in 2D. By doing so, the set of degrees of freedom per body is reduced from 9 to 3, resulting in ignorance of a lot of interactions that have an effect on the jacket behaviour. Due to the fact that in this thesis it was chosen to only look at the forces in the load cable, the decision to ignore these influences is probably quite ok. When more criteria will be researched however, these influences become more important. When large horizontal displacements in y-directions take place for example, the cables could run of of their sheaves.

In addition, waves are considered to be uni-directional. For several reasons this could give conservative results: slamming e.g. in this case always occurs on two out of four buckets at the exact same time, where in reality this might not be the case, due to the irregular behaviour of the waves, in both x and y direction. Since these mutual slamming timing seemed to be quite important, 3D models will give different behaviour. Another factor induced by this irregularity is that the forces on braces in y-direction are not the same over the entire area, where in this thesis they are.

In order to be more accurate, the model should be created in 3D. The fact that the current model is already created, means that the 3D model is not to be completely modelled from scratch.

6.2.2 Jacket modelling

In force calculations, the geometry of the jacket has been simplified quite severely to reduce computational time. The stick model has been used in horizontal wave force calculations, submergence levels have been taken equal over lengths, and nodes that hold the braces are not considered. When the members are treated separately in calculations, the results will be more accurate and less conservative.

In addition, in this thesis the jacket is modelled as a rigid structure, meaning that forces are directly transported across the structure into the slings and crane. In reality though, the geometry and material properties do have an effect on the propagation of the forces. As will be explained later in section 6.3.1, these effects will probably slightly dampen the forces that are observed in the load cable. The results gained in this thesis therefore will in fact be somewhat conservative.

A consideration is to be made whether the improvement in accuracy of the results due to these adjustments weigh up to the amount of extra computational time. In this thesis, the fact that the assumptions made regarding this topic were considered to give conservative results have led to the decision to accept the simplifications. A further study should be performed in order to show the actual effect of more accurate jacket modelling. Depending on the results of such a study, the model could be adjusted for further analysis.

A side note here in however is, that when different criteria are used, some effects that were not important in this thesis do become important. The stick model used in horizontal wave force calculations for instance is a decent assumption here, but its conservativeness could affect the results one may obtain in horizontal offsets, which could be important for other criteria.

6.2.3 Splash zone model testing

As was discovered in the previous chapter, the influences involved in the splash zone transition of the buckets are very important for the subsequent behaviour of the jacket. The forces in this region have now been analysed theoretically, via the methods described in section 4.4. Several major assumptions have been made, especially in the calculation of the air cushioning effect. In reality, the flow of both air and water will behave way more complex than was assumed in section 4.4.1. This behaviour will induce minor differences in results, resulting in differences in timing and magnitude of slamming. Some of the effects that could be encountered are listed below:

- Heat exchange from air with water;
- Viscous boundary layers inside suction bucket;
- Air leakage;
- Air cushion geometry;
- Sloshing in the buckets;
- Damping effects due to turbulent flow inside the buckets.

The formation of the air cushion, the slamming and the interaction between these two further depends on bucket geometry and environmental parameters. As was mentioned in the same sections, in order to be really accurate for the jacket design in question, it is recommended to perform either model testing or CFD analyses in this area. Actual behaviour can then be studied, which could either be used directly, or to design a more accurate theoretical approach for load calculations. Furthermore, hydrodynamic coefficients and the actual added mass of the bucket can more properly be defined, which could be beneficial in the results, since its heave added mass showed to have a large influence upon the eigen-period of the jacket oscillation.

6.2.4 Crane handling

Perhaps the most important feature that is not considered in this thesis is the fact that the crane driver in practice constantly adjusts his crane properties, as a reaction on what he sees happening. The effect this could have on the results is discussed in this section.

At first, the crane driver does not use a constant lowering velocity throughout the procedure: he will change his speed in correspondence to the conditions in which he works, and to the installation phase he is in. As was shown in section 5.4.1, in general the lowering velocity will be increased once an object such as a suction bucket is lowered through the splash zone, in order to minimize the amounts of slamming occurrences and the time frame in which the large horizontal areas are in reach of the wave kinematics. When the buckets are sufficiently submerged, the velocity will be decreased again, until the buckets reach close proximity of the seabed. Apart from these major adjustments, the crane driver could react upon large jacket oscillations, by timing an increase in lowering speed when the jacket moves downward.

In addition to the adjustments the crane driver makes on the lowering velocity, he will constantly check, and if necessary adjust the angle of his boom. This boom angle control has not been considered in the model either, because of the fact that

actions are reactionary and there are no guidelines to be found that state when and how adjustments are to be made. Lastly, in case the model is adjusted to 3D, the crane driver controls the remaining crane degrees of freedom.

Due to the fact that non of these crane handling adjustments are taken into account, the results gained in this thesis will be somewhat to the conservative side (in case the crane driver would do his work properly).

Since these adjustments in practice are influenced by human actions, it is difficult to incorporate them in the model. Some sort of a control mechanism is to be built in, which detects events and acts upon them. The event function that was used for the slamming for instance can be used to do so. Accurately considering all the crane operator's actions will be close to impossible, but several could be incorporated. In dialogue with a crane operator some of these control mechanisms can be designed and implemented in the model. By doing so, the conservativeness of the results can be lowered, which could result in less intolerable cases. The model as it is now can be used in this process, by performing parameter studies on e.g. ideal lowering velocities or boom angles. The analysis performed in section 5.4.1 can be extended by using different velocities throughout installation.

In appendix N an example is given in which the lowering velocity is adjusted during installation. Here, the jacket initially was lowered with $0.5\ \frac{m}{s}$, stopped half a bucket diameter from the seabed and lowered further with a smaller velocity of $0.1\ \frac{m}{s}$. Introducing a resting period in between these two different velocities, in order to let the jacket dampen out by drag, seemed to positively affect the DAF in subsequent installation. The difference in DAF between the scenario with a resting period in blue and that without in red is given in figure 6.2.

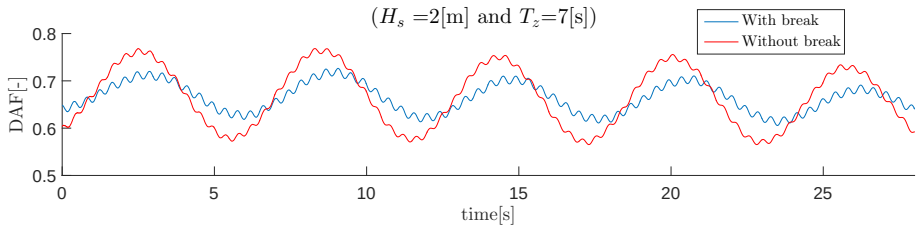

Figure 6.2: The influence of a resting period, on the load cable DAF

This example therefore proves that it could be beneficial to include these control features into the model.

6.2.5 Model validation

No validation of the complete model is present. Programs as Orcaflex, SIMO or Ansys Aqwa could be used in order to check whether results will be found similar to those achieved with the model. The problem with these programs however remains that they too use large assumptions. Especially the methods in slamming determination are generalized and will thus probably show different results as were acquired in this thesis. Orcaflex [35] for instance uses slamming coefficients and SIMO [31] uses the change in added mass in order to calculate slamming. As was stated in section 4.4 both these methods depend much on what happens prior to slamming and on the bucket geometry, which makes it hard to not make large assumptions. Especially the bucket splash zone transition will thus be filled with assumptions. As was stated earlier in this section, either model testing or CFD analyses should be performed in order to come up with real accurate results.

However, since these programs are widely used and their analysis are globally accepted, they could undoubtedly be used to validate the remaining parts of the installation. They especially could be used in order to validate whether the hydrodynamic coefficients used in the model are well chosen. The heave added mass of the bucket for instance showed to have a large influence on the jacket behaviour.

6.3 Other forces and influences

On top of all the forces that were discussed in chapter 4, there are more influences that could be considered in order to improve the model in its accuracy. For this research it has been assumed that these forces are of minor influence upon the criteria studied. In case more criteria are chosen to be incorporated however, some of these forces should be taken into account. In this section several of these additional forces and influences are discussed.

6.3.1 Damping

Within the model, all damping is implemented in the drag terms of the horizontal- and vertical waves. In order to visualise and quantify the effect this has, a simulation is ran where the jacket is given an initial positive vertical displacement of $1\ m$, while it is being held still at $20\ m$ submergence. Merely the force induced by the vertical drag term is considered in the calculations. The wave kinematics however are set to

zero, resulting in only the jacket's velocity terms to be used in the force determination. It should thus oscillate in its eigen-period, with a decreasing amplitude. This behaviour indeed is observed, as can be seen in figure 6.3.

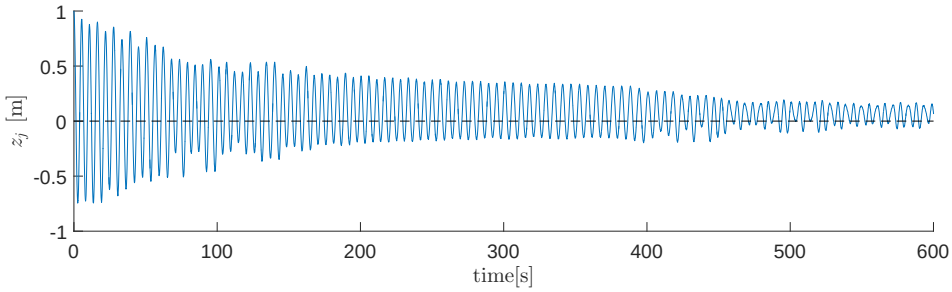

Figure 6.3: Damping by drag

The fact that this large time frame is chosen already indicates that the damping ratio ζ is fairly low. Its value can be calculated via equation 6.1, by making use of two oscillation's amplitudes (a_1 and a_{n_o}) and the amount of oscillations observed in between these values (n_o).

$$\delta = \frac{1}{n_o} \ln \frac{a_1}{a_{n_o}} \tag{6.1a}$$

$$\zeta = \frac{\delta}{\sqrt{4\pi^2 + \delta^2}} \tag{6.1b}$$

However, since the vertical displacements of the jacket are affected by the boom rotation and horizontal displacements, this calculation will not give proper results. The effect of these other displacements can be observed in figure 6.3, by the offset of the oscillation: the jacket does not oscillate around zero. The calculation does however give an insight in the magnitude of damping. By these equations, a damping ratio of 0.7% is found, which is a low number considering it is the only damping term involved in the model.

In reality, there are more factors that induce damping. Material damping for instance is usually identified as damping associated with hysteresis energy loss in materials, as it experiences stress cycling. This damping type could be considered in the crane elements, the slings and in the jacket itself. Another important inducer is inter-facial damping, which results from contacting surfaces at bolted joints, sliding joints or welded joints. This will definitely be present in both the crane and in the

jacket. As was mentioned in the previous section, the latter in this thesis is modelled to be rigid, so forces and displacement are directly transported to the slings. In practice though, the forces and distributions are transported via the members, the nodes and additional steel, which results in part of the energy to be dissipated.

In the previous chapter it was discovered that the slamming induces a rotational oscillation of the crane boom. Where in the model this small oscillation remains the same over the entire subsequent installation phase, in reality it will soon be vanished, due to damping features mentioned in this section. As was observed in several cases, the amplitude of this small oscillation could in fact be that extra force in the load cable that causes the DAF to exceed 1.3 (like is shown in multiple examples in appendix K). Adding a term that dampens this oscillation to the model therefore directly results in less simulations with exceeding DAF values.

In order to visualise this effect, in figure 6.4 the simulation of section 5.1 (H_s= 2 m and T_z= 7 s) is ran once more, with a damping term added to the boom rotation. A linear rotational boom damping ratio of 1% is iteratively sought and implemented. As can be seen in the figure, the small period oscillation around the main DAF in this case indeed dampens out to a lower amplitude over time.

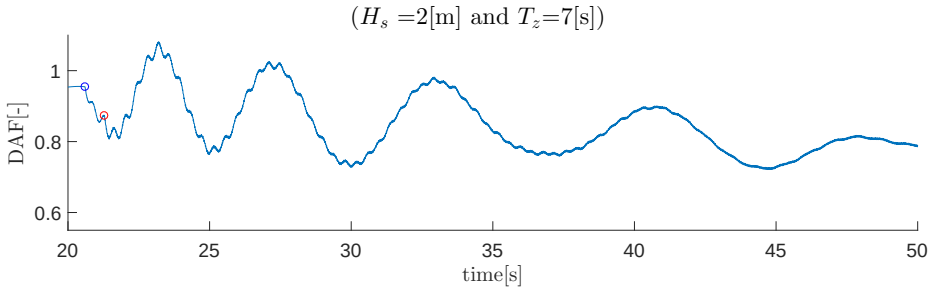

Figure 6.4: The influence of crane boom damping, on the load cable DAF

This damping however is only an approximation to visualise the effect it has. In order to accurately incorporate these kinds of damping in the crane elements though, they should be added using material- and joint -corresponding damping coefficients.

Another factor that induces damping is the waves: when an object moves close to the free water surface, outgoing surface waves will be generated, caused by the work done to dampen motion of the object. In the model it is assumed that the damping energy dissipates through a quadratic term, implying that this linear damping term

is implemented in the drag term of Morison's equation. It could however be treated separately. The resulting force generated by the outgoing surface waves is defined as the wave damping force and is proportional to the velocity of the object.

However, if the object oscillates with a high or low frequency, this force vanishes. According to DNV [9], the period of oscillation for which this is the case depends on the diameter of the object of interest:

$$T > \sqrt{\frac{2\pi D}{g}} \tag{6.2}$$

In order to find out whether this requirement is satisfied for the model, the x-directional period of the left bucket has been studied, in the time it crosses the sea surface. This is done for minimum T_z values and, due to the fact that the interest primarily focusses on rough sea states, a H_s of $2\ m$ is chosen. In order to show the oscillations for much smaller, high frequency waves too, a H_s of $0.5\ m$ is used as well, in combination with a T_z of $2\ s$. Outcomes for both these conditions are plotted in respectively the upper and lower figure in figure 6.5.

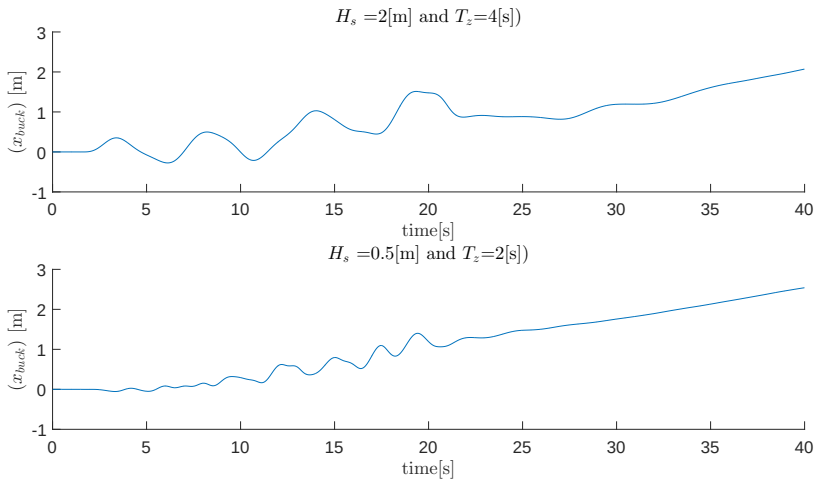

Figure 6.5: Horizontal bucket oscillation in vacinity of the sea surface

The horizontal jacket oscillation period for the first case, approximately 4 to $5\ s$, is sufficiently high to satisfy the maximum allowed period of $2.4\ s$ found by equation 6.2. For the other wave conditions though, the oscillation period of approximately 2

s does not satisfy the maximum allowed period to disregard wave damping. However, as was determined before, by looking at wave scatter diagrams of the North sea [19], such low periods do not occur that often and are therefore not considered in this thesis. When in further studies a wider spectrum of waves are researched and these wave combinations are involved, wave damping should be considered.

Further, once the buckets are fully submerged and the jacket members cut through the sea surface, the period of oscillation is even higher, due to inertia. In addition, these members have a relatively small diameter, so the maximum allowable period automatically decreases in correspondence. Therefore, wave damping on these members has not been incorporated here and there is no need to implement these influences in further studies.

In order to see what happens to the load cable DAF when a linear vertical damping is added to the system, an extra upward pointing force upon the jacket's COG is implemented, proportional to its vertical velocity. Via an iterative process the damping coefficient that is used here in is chosen such that a damping ratio of 5 % is found. For two cases that have been discussed in the previous chapter, the newly achieved DAFs are plotted in figure 6.6. In red, the simulation is ran with damping considered. Important to note is that this example is created in order to visualise the effect damping has upon the system; the derivation of the actual damping is an approximation and not at all representative for what happens in reality.

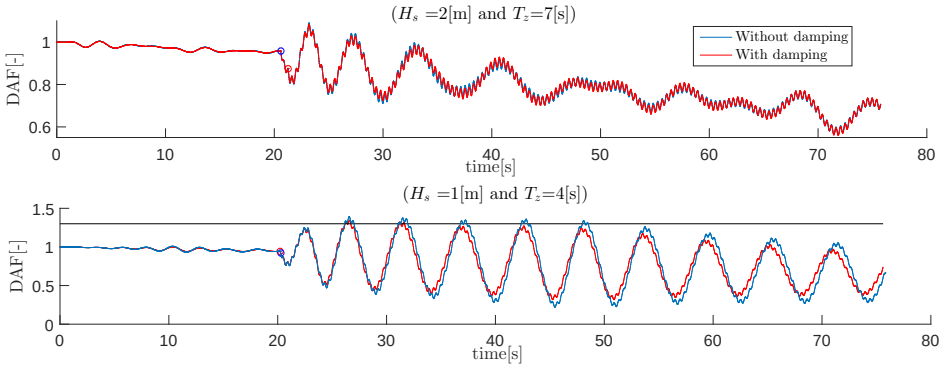

Figure 6.6: The effect of 5% vertical damping, on the load cable DAF

The DAF of the lower figure is affected more by damping than in the upper figure. As was discussed in section 5.2, the wave combination of this lower figure showed high magnitude simultaneous slamming and a wave period in range of the system's

vertical eigen-period. The oscillations in vertical velocity therefore are high in magnitude. Since the damping is proportional to the velocity, it is logic that it affects this case extensively: damping often has a large influence in resonant behaviour.

From the examples given in this section can be summarized that damping plays a role in the magnitude of the load cable DAF, especially in the cases that show resonant behaviour. In order to be accurate therefore, it would be beneficial to include proper damping terms in the model, in the form of material damping, interfacial damping and geometric damping of the jacket. Wave damping should only be added for situations where it would have effect.

6.3.2 Diffraction

In the model, Morison's equation is used in the determination of forces induced by the horizontal wave kinematics. Even though this method gives a good approximation of these forces, it lacks a good determination of the effect the structure has upon the wave kinematics. In reality, diffraction will play a role: the motions of the jacket, primarily the buckets, induce diffracted waves. In figure 6.7, the wave force regimes according to Chakrabarti [7] are shown. The diffraction region, which can be found in the right bottom of the figure, counts for smaller wavelengths and higher diameters. The buckets therefore especially will induce diffraction. For the wave combinations used in this thesis, the bucket's regions are indicated with in blue. For T_z values of $6\ s$ and lower, the diffraction region is entered.

In 1954 Mac-Camy and Fuchs [30] developed a theoretical expression for the horizontal force per unit length that takes this diffraction into account. They discovered that their force in fact corresponds to the inertia term in Morison's equation. Therefore, if the two expressions are set equal to each other, the Mac-Camy and Fuchs force can be expressed in Morison's mass term format. This can then be incorporated as a corrected added mass coefficient and, due to the fact that the inertia force is linear with respect to the acceleration, alternatively as a correction on the wave particle acceleration. The advantage of this latter method is that the modification can be performed on each wave component in the irregular wave spectrum. The correction on the acceleration is provided in equation 6.3, as was found in a hydrodynamic manual by USFOS [41]. As can be seen, it automatically detects whether the diffraction should be considered, due to the fact that it incorporates the diameter over wave length ratio.

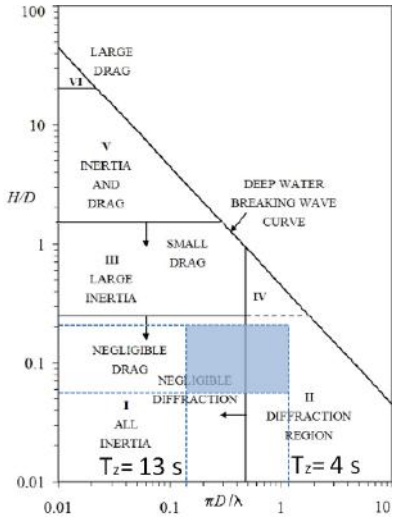

Figure 6.7: Wave regimes according to Chakrabarti [7]

$$\dot{u}_{mf} = \dot{u} \min \left[1, \frac{1.05 \tanh(2\pi \frac{d}{\lambda})}{\left(\left| \pi \frac{D}{\lambda} - 0.2 \right|^{2.2} + 1 \right)^{0.85}} \right] \tag{6.3}$$

In order to show the relevance of the diffraction, in figure 6.8 the difference in DAF and horizontal jacket displacements is shown, when this correction is incorporated in the model (in red) and when it is not (in blue). Waves with a small T_z value are chosen in this study, since lower wave periods via the dispersion relation are directly linked to smaller wave lengths, resulting in larger diameter wave length ratios and thus diffraction.

The effect the diffraction has upon the x-displacements can clearly be seen. The effect it has on the DAF on the other hand is negligibly small. Therefore, the assumption that for the criteria used in this research diffraction can be rejected holds. However, if one would look at criteria based on the horizontal displacements of the jacket, diffraction should be handled with more care. The Mac-Camy Fuchs correction is be an easy way to incorporate diffraction in that case.

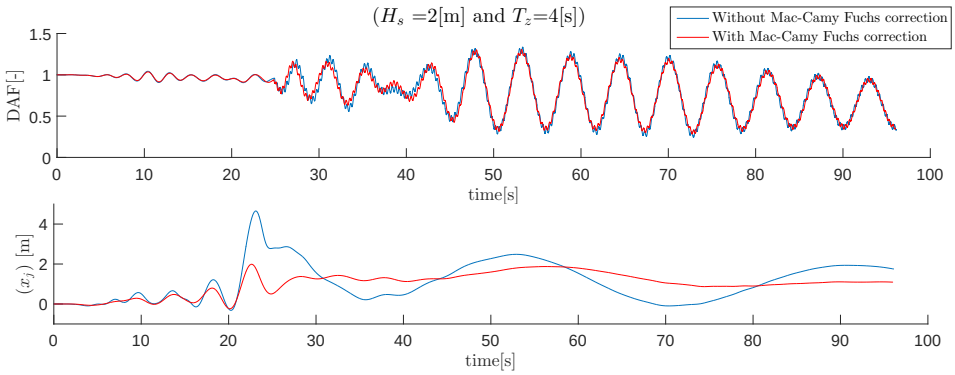

Figure 6.8: The effect of the Mac-Camy Fuchs correction

6.3.3 Seabed forces

As was explained in section 4.6 and appendix J, the decision to use a constant lowering velocity results in forces that are too high compared to reality, when the buckets are in proximity of the seabed. The installation therefore are stopped when the bucket reached 30% of the bucket's diameter from the seabed.

In order to show the magnitude of these forces, which primarily are induced by increasing added mass and hydrodynamic pressure, in figure 6.9 a simulation is ran which stops only $0.2\ m$ above the seabed. As a comparison, the forces induced by the seabed interaction (in red) are plotted next to the buoyancy force and the vertical wave force (respectively blue and green). Once the bucket gets close to the bottom, the seabed forces show a jump in magnitude, up to values that are comparable with the jacket's weight.

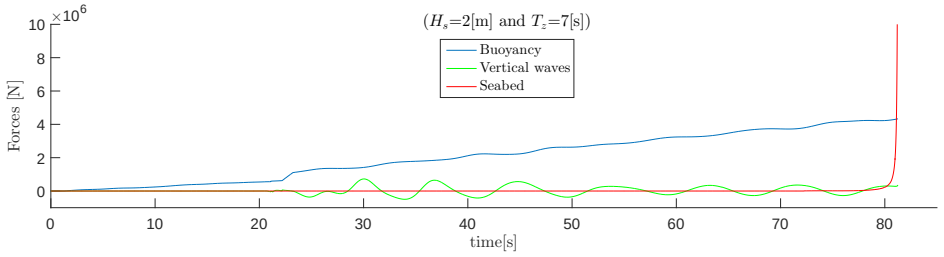

Figure 6.9: Seabed forces with a lowering velocity of $0.5\ \frac{m}{s}$

Since these forces act in the vertical upward direction, they are directly linked to the load cable forces, and could induce slack behaviour. It is therefore important to find out to what extend they affect the jacket displacements for lower lowering velocities. This is studied using the displacements and velocities found in appendix N, where the jacket was held still approximately $5\ m$ above the seabed for a period of of $200\ s$, in order to let it dampen out somewhat in the waves. These lastly observed values are used as initial conditions for further simulation, where the jacket is lowered with a velocity of $0.1\ \frac{m}{s}$ until it reaches $0.2\ m$ above the seabed. The results gained are given in figure 6.10. The peak in force is drastically lowered compared to the one found in the previous example.

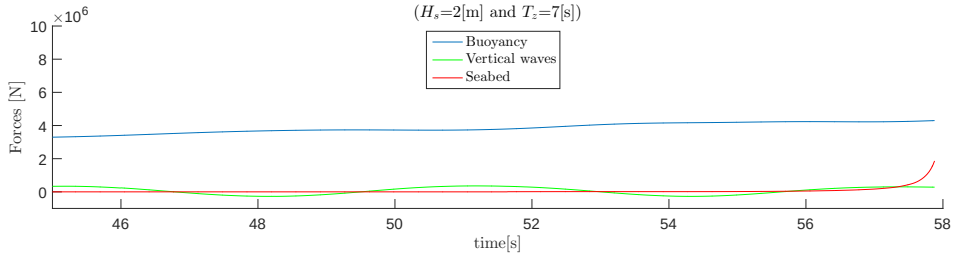

Figure 6.10: Seabed forces with a lowering velocity of $0.1\ \frac{m}{s}$

The seabed interaction forces are already incorporated in the model. However, since only one constant lowering velocity is used, the simulation is stopped somewhat earlier, in order to prevent huge forces to occur. When the adjustments in lowering velocity, as described in section 6.2.4 are incorporated in the model, the simulation can be ran for a longer period of time, so the seabed region is incorporated too. Since the forces grow rapidly for large lowering velocities, they could cause slack. In further studies these forces should therefore absolutely be taken into account.

6.3.4 Jacket member slamming

Likewise for the buckets, the jacket members are subject to slamming forces once they cross the sea surface. Since more extensive research has been conducted on slamming forces on cylinders using the slamming coefficient, the determination of these forces are more reliable than for the buckets (as has been discussed in section 4.4.2). Loads of theories and experiments have been conducted on cylinder slamming coefficients, and more recently, numerical approximations have been made.

The latter is caused by the fact that computer power increased rapidly, theoretical approximations lack accuracy and experiments are expensive. Greenhow and Yanbao [17] compared the theories as were discussed in section 4.4.2 with the experiments, by rewriting the half-widths of the flat plates of von Karman and Wagner (respectively figure 4.12a and 4.12b) to those of circular cylinders. In figure 6.11 some of the outcomes they found on slamming coefficients against penetration depths are shown. The results gained by experiments by Campbell and Weynberg [6] (line 1 in the figure), based on drop tests in still, disturbed and aerated water, still is the most widely used theory for slamming problems on horizontal cylinders. Their formula for the slamming coefficient, given by equation 6.4, is widely accepted in the industry and is used as a recommended method in guidelines by DNV [9]. In the equation, s is the submergence of the cylinder, given by $h + \frac{D}{2}$, D is the diameter of the cylinder and h is the distance from the center of the cylinder to SWL. The maximum value of C_s in this case is thus 5.15.

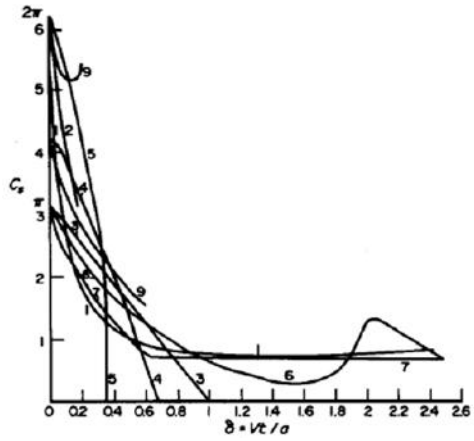

Figure 6.11: Slamming coefficients, against penetration depth. 1-Campbell and Weynberg(1980), 2-Fabula ellipse theory(1957), 3-von Karman, 4-semi-Wagner, 5-Wagner (flat plate approach), 6-von Karman (Kaplan and Silbert, 1976), 7-semi-von Karman, 8-semi-Wagner, 9-Wagner (exact body approach)

$$C_s(s) = 5.15\left(\frac{D}{D+19s} + \frac{0.107s}{D}\right) \tag{6.4}$$

In order to determine to what extend these additional slamming phenomena affect the results, a quick calculation is performed on their magnitude upon the horizontal braces. Using equation 4.28, with a total brace contact area A_{ss} of 0.813 m (diameter) times 27 m (length), the slamming force is calculated to be $5.8 \cdot 10^4$ times v_{rel}^2 N. Since v_{rel} will primarily be in the order of 0 to 1.5 $\frac{m}{s}$, the slamming force on the horizontal brace will always be small. The value calculated here is even conservative: in reality the contact area will be smaller, since the slamming will never occur over the entire member length in once.

The impacts upon the other jacket members further will be considerably smaller, due to their angle with the horizontal plane. This proves that the assumption made not to incorporate these slamming phenomena into the model has been correct.

6.3.5 Object motion control

In practice further equipment is used to control object motions in lifting procedures: tugger wires, guide wires, additional constant forces and guiding stiffness, and active or passive heave compensation tools. The first mentioned are mainly used to make sure the structure is positioned in the right yaw-direction. Additionally, the stiffness of the wires and guiders prevent the structure to move in x- and y directions (surge, sway, roll and pitch). The effect this has on lifting wires of the crane is negligible, therefore the influences of tugger wires, guide wires and guiding tools have not been considered in this thesis. Looking at other criteria though, it is recommended to incorporate these forces in the system.

Active and passive heave compensation tools on the other hand do have a huge effect on the vertical dynamic effects on the crane. It could be a recommendation to use such tools in able to create a wider weather window, but they do introduce additional static weight in the crane. Siemens therefore prefers installation without the use of these tools.

6.3.6 Miscellaneous influences

A couple of additional forces that are considered to have a negligible effect on the system, even in case other criteria are examined, are given below. They are discussed less extensively, but it is worth to mention them, in order to sketch a complete picture.

Wind forces

The jacket elements that are not submerged yet are exposed to wind, causing primarily horizontal forces upon the jacket, the crane boom, crane cables, slings and hook. In this thesis these wind influences have not be taken into account, since it was assumed that they have a negligible effect on the total forces in the load cable. Its influence on these types of installation would not be affected that much, compared to that of the waves. In addition, vessels in practice have limiting wind velocities in which installation is allowed to be performed. These harsh wind conditions often are accompanied by wave conditions that exceed the limit too.

Horizontal slamming

Apart from vertical slamming, once jacket elements are in the splash zone breaking waves can induce horizontal slamming forces too. Due to the fact that there is no need to consider such breaking waves for these installation procedures, since these only occur in harsh wave conditions outside of the range of interest, the horizontal slamming forces do not have to be considered either.

Vertical/horizontal components due to horizontal/vertical wave forces against braces under an angle

In the model, horizontal wave kinematics only excite horizontal wave forces on diagonal braces. The same accounts for the vertical wave forces. In reality though, this is not exactly the case: due to the fact that these braces are positioned under an angle, horizontal forces will in fact have a vertical component too. This phenomena is partially taken into account in the determination of the equivalent diameters of the stick model, but no physical vertical forces are modelled that are caused by the horizontal waves. However, it is assumed these forces are negligibly small and do have a minor effect on the jacket behaviour.

Skew loads

Lastly, skew loads are additional loads caused by equipment or fabrication tolerances and other uncertainties with respect to asymmetry and associated force distribution in the rigging arrangement. Some effects that may cause skew loads according to DNV [10] are listed below. Apart from the fact that it would be hard to incorporate these phenomena in the model, these forces are considered to have a minor effect on the results.

- sling length inaccuracies;
- fabrication tolerances of lift points;
- deflections of lifted object;
- crane hook geometry;
- multi hook lifting;
- doubled slings;
- difference in sling elongations;
- etc.

6.4 Design adjustments

Within this thesis, several design choices are made prior to the analysis. All results gained have used these designs in the calculations. In practice, the model can be used in performing parameter studies to improve certain design decisions, as a first step in an iterative process to lower the chance of intolerable DAF values. Adjustments could either be made in the rigging- or jacket design, depending on the goal that is to be achieved. Several optional design adjustments for both cases are discussed in this section. The knowledge gained in this thesis is used to converge to specific factors that probably have the largest beneficial effect.

6.4.1 Adjustments in rigging design

As was observed in the last sections of chapter 3, the design of the rigging affects the natural frequency in which the jacket can freely oscillate. The assembly of the crane boom, boom hoist cable, load cable, and hook obviously depend on the installation vessel chosen, but the sling formation can be designed project specifically.

In this thesis, the natural period of the rigging assembly in combination with added mass showed to be within range of possible wave combinations. In practice this will be prevented as much as possible: either the sling length, material, diameter, angle in which they are positioned or the amount of slings used should be adjusted such that the natural period of the system is out of this range. By doing so, the chance on resonance will be reduced and higher workability ranges will be achieved.

In order to show the change in natural frequency, in case larger diameter slings are used, and in case the initial angle of the slings are chosen differently, the upper figure in figure 6.12 compares the accompanying behaviour of the jacket when it is given an initial vertical displacement of $0.1\ m$ with that found in section 4.5. All environmental forces are switched of in this simulation.

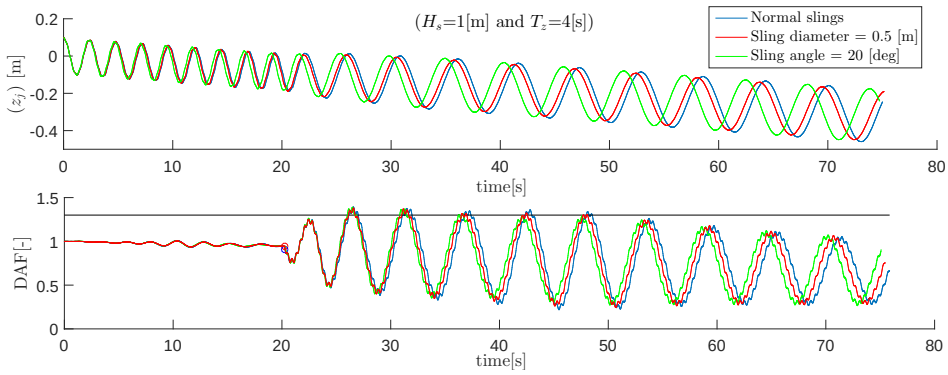

Figure 6.12: Eigen period and DAF, with adjusted slings properties

In the red line the diameter of the slings is increased from 0.184 to 0.5 m. This would logically result in higher sling stiffness, causing the total assembly's stiffness to increase and the natural period to decrease. Looking at the results, the growth of the natural period indeed happens somewhat slower. In the green line the initial angle of the slings is decreased from 30 to 20 deg. This corresponds with an additional 7 m sling length, which would logically result in a lower sling stiffness, and a more rapidly growing natural period. However, since an increase in length of the slings results in a decreasing length of the load cable, this adjustment shows the opposite behaviour. Due to the fact that less load cable length is now used, the total system's stiffness increases and the period of the jacket oscillating in the water grows less fast.

In order to show the effect the adjustments have upon the load cable forces, in the bottom figure of 6.12 a simulation is ran using wave periods in range of the resonance regions. In these simulations, the forces are switched back on. Here, it can be seen that the delay in period growth results in somewhat different load cable forces. Using these sling properties still seems not to be sufficient though: the added mass still highly affects the eigen-period.

These examples do show that adjustments in the rigging can be used in order to make sure the period grows slower, reducing the chance on resonant behaviour. The lowering velocity of the crane can be of help in this too: the faster the jacket is lowered, the faster the length of the cable increases, the stiffness decreases, and the period increases. It would be recommended to perform parameter studies in order to find the perfect rigging arrangement.

6.4.2 Adjustments in jacket design

The model can be used for finding design improvements for the jacket too. A good example of a design aspect that has an influence on the timing and magnitude of the slamming for instance is the perforation rate of the buckets. In figure 6.13 the splash zone velocities (vertical and rotational) are shown for three different perforation rates: a very small one, 0.5% (in green), the rate used in calculations, 5% (in red) and a large one of 20% (in blue).

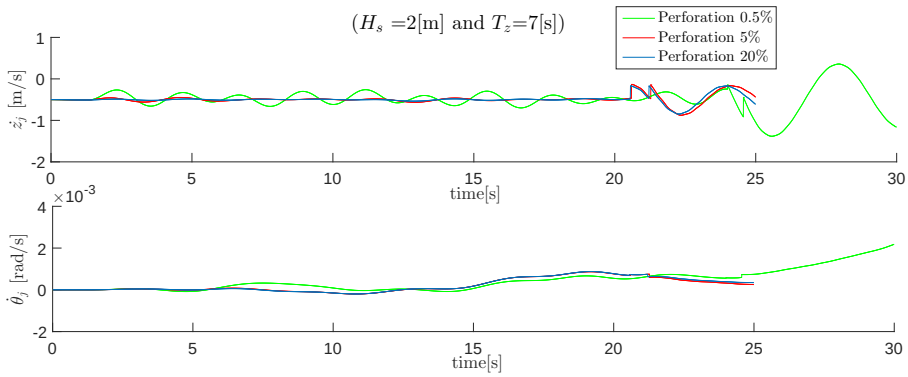

Figure 6.13: Different slamming behaviour for different perforation rates

As can be seen, the difference between the latter two is not that high, indicating that the air cushioning effect is very small already with the chosen perforation rate. For the 0.5% case however, the air cushioning effect influences the system more severely, causing the slamming to occur a couple of seconds later, with a way smaller first slam-magnitude. This results in completely different subsequent behaviour, as can be seen in figure 6.14. Here the jacket displacements and load cable DAF are compared for a perforation of 0.5% in blue and 5% in red. The low perforation rate induces a large upwards buoyancy force upon the buckets: the jacket gets lifted up approximately half a meter prior to the moment the water inside hits the top of the bucket. This initial upwards displacement causes the jacket to basically fall down once the first bucket has slammed, resulting in an increment in the load cable DAF. As can be seen in the right bottom figure, it even reaches a value of 1.3. This example proves the importance of the perforation rate that is to be chosen.

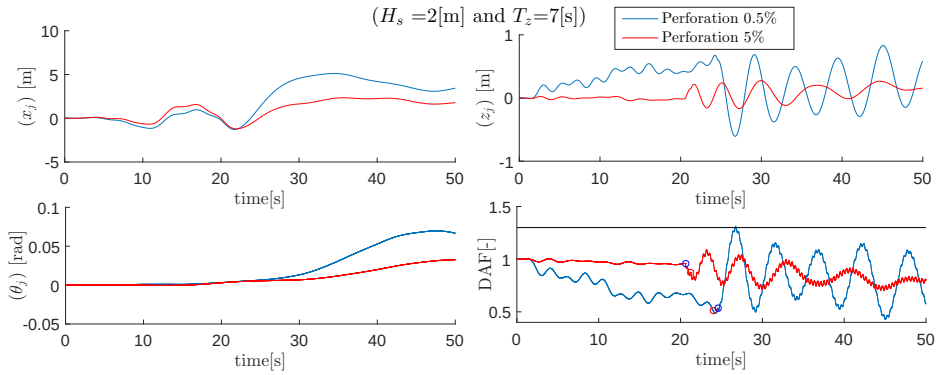

Figure 6.14: Different displacements and DAF values for different perforation rates

Another result from increasing perforation rates is a decrease of the the bucket's heave added mass (as can be seen in the derivation of this specific added mass, in appendix H). Since this added mass showed to affect the eigen-period, it could be beneficial to lower its value. In order to test whether this is true, in the upper plot in figure 6.15 the eigen-period study is performed for three different perforation rates. As expected, the larger perforation rates show slower eigen-period growth over submergence. The added mass for 10% and 20% perforation rate respectively lead to 4% and 24% decrease of heave added mass for the buckets.

Looking at the load cable forces for the same three perforation rates, in waves with periods in resonance regions, it seems the higher perforation rates indeed show way less resonant behaviour than the 5% used before. This is purely caused by the lower added mass, since from the splash zone analysis it was concluded that the perforation rate of 5% shows the same air cushioning and slamming timing as higher rates. For further studies, it therefore is interesting to look at this rate, in order to find a for in water installation- ideal perforation rate.

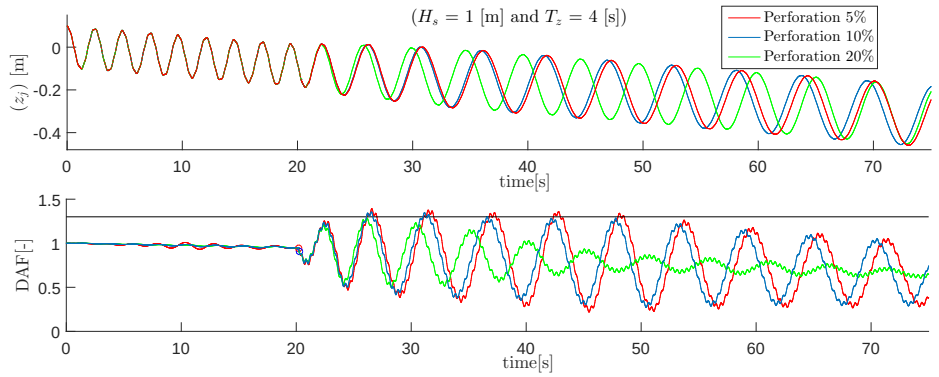

Figure 6.15: The effect of the change in eigen-period, caused by decreasing added mass as a result of larger perforation rates

Another design consideration could be to adjust the geometry of the inner bucket. In the design used, the bucket has a flat, horizontal inner top. In order to lower slamming magnitudes and create a smoother transition for the water and or air to escape through the ventilation hole, the top could be placed under an angle, pointing towards the ventilation hole. Apart from the beneficial effects on the air cushion and slamming, the bucket added mass will be affected too.

The adjustments in the bucket design however should be in line with their function: where adjustments could result in smoother splash zone transition, it could affect the efficiency of the actual soil installation and stability once it is positioned.

6.5 Floating installation vessels

In the first chapter it has been mentioned that it is interesting to perform the same analysis using a floating vessel in stead of a jack-up. By using such a floater, more degrees of freedom will be introduced to the system. The vessel itself will now move in the waves, causing the crane origin to have its own displacements and velocities, depending on the wave conditions. The crane will therefore be introduced with additional displacements, velocities and accelerations, which have an effect upon the entire system: relative velocities and oscillation periods for example change. All forces discussed in this research will be affected by these phenomena, resulting in more complex jacket behaviour.

Introducing a floater as an installation vessel, the tables acquired in the previous chapter will be somewhat different. Expected is that more of the wave combinations will show exceeding DAF values, since the crane tip now pulls more severely at the other end of the load cable. Higher relative velocities could be encountered, leading to larger slamming- and vertical wave forces. On the other hand, the geometry of the vessel could be used in a beneficial fashion, by performing the installation at the leeward side of the vessel. By doing so, the waves that are encountered by the jacket are dampened and less severe. It should however made sure that this method does not cause problems in the vessel's roll motion.

Since the benefits of these types of vessels over jack-ups primarily lay in the larger deck spaces and the possibility to install at bigger water depths, it is interesting to be able to compare the two in terms of the criteria sketched in this thesis. The model created can be adjusted such that the extra degrees of freedom of the floating vessel are incorporated. The vessel's COG movements can be written in terms of the irregular wave patterns by means of RAO's, which can be rewritten to the movements of the crane origin- and tip, by using translational and rotational transfer functions as were used in this thesis.

6.6 Discussion summary

In this chapter a discussion is started on how the model created can be used for further research. The largest assumptions made in the previous chapters are put up for discussion and recommendations are made stating how some of these assumptions could, or should, be treated differently. In case the model is used for further analysis, some adjustments can be made as a first step in iteratively improving the model and installation procedures. Based on the results gained from this thesis, some recommendations are given, which could help in this process.

The most important features that would improve the model and research are by looking at more criteria and including forces and influences correspondingly. Improvements in results could further be gained by considering a 3D system, and by taking crane handling and damping terms into account. Since slamming showed to be an important factor in the system, it would be beneficial to improve the theories used in this thesis, by performing geometry-specific model tests.

Lastly, some recommendations have been made in improvements in both the rigging- and jacket design: it seems that jacket oscillation eigen-periods can be somewhat tuned by using different sling arrangements and adjustments in bucket design.

Chapter 7

Conclusions

The main goal of this research was to gain insight in maximum wave conditions in which installation of a four-legged suction bucket based jacket foundation could safely take place. The criteria used to define these limits were based on the maximum allowable forces in the crane load cable.

In order to achieve this goal, a 2D time domain MATLAB model has been created, containing the most important features of a heavy lifting jack-up crane vessel and its appropriate rigging elements. The model is used to calculate the forces in the crane cable, as a result of the jackets behaviour through its interaction with the water.

The environmental forces that act upon the jacket during the installation are based on a $40\ m$ deep ocean, with a current that follows a water depth dependent profile, and with an irregular wave field, which is modelled with the JONSWAP spectrum. The most important forces and influences that are caused by these waves have been incorporated in the model. For this specific jacket design some particular phenomena occur when the large suction buckets are lowered through the splash zone: an air cushion is created within the buckets and a vertical slamming arises when the water collides with the inner top. The latter initiates a jump in the jackets vertical velocity, resulting in oscillation in the crane. The non-linear interaction between the random waves and these splash zone phenomena cause unpredictably in maximum slamming magnitudes and impact times. An effort is made to theoretically define these forces, by comparing methods found in literature with a more direct approach that uses the law of conservation of momentum. The latter is chosen to be used in calculations, since it requires the least assumptions.

With the resulting model, for a predefined set of wave combinations simulations are performed in order to be able to study jacket behaviour and forces in the load cable during installation. From this study, insight is gained in individual force contributions and their mutual interaction: looking at the jacket's oscillation in the crane, the system's heave added mass affects the vertical eigen-period such that once the buckets are in the water, it extensively grows from $2.5\ s$ to a maximum of $6\ s$. The jump in the jacket's vertical velocity, that results from slamming, initiates the jacket to oscillate in this eigen-period. The magnitude of the relative velocity between the bucket in question and the water determines the amplitude of this initial oscillation. More importantly, the initiation of this oscillation could be timed such that synchronisation with the waves occurs. The vertical wave forces in this case will enforce the vertical oscillation amplitude of the jacket, which directly is linked to the forces in the load cable. Lastly, the independent timing between slamming on the left and right bucket could either cancel out- or enforce the oscillation.

Due to the fact that the system depends on the interaction of multiple phenomena, it showed to be very complex to predict the jacket's behaviour for different wave conditions. In order to take the randomness of the waves into account, a Monte Carlo simulation is performed, by using multiple simulations per wave combination, each with different initial conditions. 50 Seeds are used as an input for particularly interesting combinations and 15 for the remaining ones. Even though no statistically profound conclusions can be drawn from the results acquired, an insight is gained in which wave combinations should be handled with extra care. Those with a T_z of 4 to $5\ s$ indeed showed resonant behaviour, resulting in un-acceptable slack and causing intolerable load cable DAF values. For a H_s of $2\ m$, wave periods lower than $8\ s$ showed intolerable DAF values.

In order to obtain statistically profound results, more than 50 seeds were required. By using 2000 seeds it showed that the DAF maxima are Weibull distributed. Knowing this, the probability of intolerable DAF values can be calculated. For waves with a H_s of $2\ m$ and a T_z of $7\ s$, this showed to be 8.94%, respectively with an 95% confidence upper- and lower bound of 10% and 7.95%. Due to the fact that this large number of simulations is computationally expensive, merely this wave combination is studied.

For the same wave combination the Weibull distribution characteristics are used in a brief parameter study on the crane lowering velocity. This study showed that the probability of intolerable DAF values is lower for higher velocities, due to the fact that the dependency on slamming decreases for decreasing lowering velocities. Like this, more studies could be performed using the model made. The knowledge

gained throughout the research is used to converge to specific factors that would have the largest beneficial effect when adjusted. From the discussion it seems that profit primarily can be gained from crane handling methods, improvements in rigging arrangements and from better modelling- and or adjusting the design of the four suction buckets.

Appendix A

Parameters used in calculations

A.0.1 Jacket Design

In table A.1, the parameters and dimensions used in order to set up the jacket model are given. These values are obtained from detailed drawings from the Siemens jacket design. The model is simplified by not considering the geometry of the nodes that are used to connect the legs and braces to each other. Their mass however is included in the total mass.

A.0.2 Rigging and crane

In table A.2, the parameters and dimensions used in order to set up the crane- and rigging, as described in chapter 3 are given. The dimensions of the crane are based on the 'Liebherr crane around the leg' crane, the load cable parameters on 'PS620 cables' by Wire Rope Industries [21] and the slings on eight-stranded 'G1960 Noble ropes' by Noble's Big Lift devision [34].

The mass moment of inertia of the crane boom is calculated using equation A.1, considering the boom to be a rigid rod with length L and mass m, rotating about one end. This assumption is often made in mechanical calculations in case of a crane boom, according to Ramamurti [37].

$$J = \frac{mL^2}{3} \tag{A.1}$$

Jacket	Mass $[kg]$	$1175 \cdot 10^3$
	Inertia $[kgm^2]$	$6 \cdot 10^{10}$
	Total height $[m]$	66
	Footprint $[mxm]$	28 x 28
	COG (from bottom bucket) $[m]$	19.67
Buckets	Diameter $[m]$	9.5
	Height $[m]$	9.5
	Wall thickness shell $[m]$	0.05
	Wall thickness top $[m]$	0.065
	Perforation rate $[\%]$	5
Legs	Diameter $[m]$	1.22
	Length $[m]$	56.4
	Batter angle $[deg]$	6.53
Horizontal braces	Diameter $[m]$	0.813
	Length $[m]$	27.87
Lowest diagonal braces	Diameter $[m]$	0.813
	Length $[m]$	30.66
	Angle with horizontal $[deg]$	38.3
Mid diagonal braces	Diameter $[m]$	0.813
	Length $[m]$	25.65
	Angle with horizontal $[deg]$	38.4
Highest diagonal braces	Diameter $[m]$	0.61
	Length $[m]$	25.45
	Angle with horizontal $[deg]$	43.8

Table A.1: Jacket parameters

Crane boom	Mass $[kg]$	$50 \cdot 10^3$
	Length $[m]$	108
	Inertia $[kgm^2]$	$1.9 \cdot 10^8$
Boom hoist cable	Youngs modules $[Pa]$	$112 \cdot 10^9$
	Diameter $[m]$	0.057
	Nr of cables [-]	14
	Total stiffness $[\frac{N}{m}]$	$4.3 \cdot 10^7$
	Mass $[\frac{kg}{m}]$	13.93
Load cable	Youngs modules $[Pa]$	$112 \cdot 10^9$
	Diameter $[m]$	0.044
	Nr of cables [-]	8
	Total stiffness $[\frac{N}{m}]$	$1.9 \cdot 10^7$
	Mass $[\frac{kg}{m}]$	9.83
Hook	Mass $[kg]$	$10 \cdot 10^3$
Slings	Youngs modules $[Pa]$	$109 \cdot 10^9$
	Diameter $[m]$	0.184
	Nr of slings[-]	2
	Total stiffness $[\frac{N}{m}]$	$3.8 \cdot 10^8$
	Mass $[\frac{kg}{m}]$	105.4
	Length $[m]$	15
	Initial angle $[deg]$	30

Table A.2: Rigging parameters

Appendix B

Wave spectrum definitions

As was explained in section 2.2, the JONSWAP spectrum is used in order to create irregular waves. In this appendix, the equations used in order to describe this spectrum are given. Equation B.1 and B.2 describe the JONSWAP spectrum, which is a modification of the Pierson-Moskowitz spectrum, and is given in equation B.3.

$$S_J(\omega) = A_\gamma S_{PM}(\omega)\gamma^{\exp(-0.5(\frac{\omega-\omega_p}{\sigma\omega_p})^2)} \tag{B.1}$$

$$\sigma = \begin{cases} 5 & \text{if } \frac{T_p}{\sqrt{H_s}} \leq 3.6; \\ e^{(5.75-1.15\frac{T_p}{\sqrt{H_s}})} & \text{if } 3.6 < \frac{T_p}{\sqrt{H_s}} \leq 5; \\ 1 & \text{if } \frac{T_p}{\sqrt{H_s}} > 5. \end{cases} \tag{B.2}$$

$$S_{PM}(\omega) = \frac{5}{16} H_S^2 \omega_P^4 \omega^{-5} \cdot \exp(-\frac{5}{4}(\frac{\omega}{\omega_P})^{-4}) \tag{B.3}$$

Here, γ is the non-dimensional peak shape parameter (average value is 3.3), $\omega_p = \frac{2\pi}{T_p}$ is the angular spectral peak frequency [$\frac{rad}{s}$], ω is the set of frequencies over which calculations are to be done [$\frac{rad}{s}$]. According to DNV [9] a set of 100 frequencies assures the randomness for floater motions. Further, $A_\gamma = 1 - 0.287\ln(\gamma)$ is a normalizing factor [-] and σ the spectral width parameter[-], (0.07 for $\omega \leq \omega_p$ and 0.09 for $\omega > \omega_p$). The peak period T_p can be calculated by multiplying the zero-crossing period T_z with 1.28.

Appendix C

Crane cable validation

In this appendix, the modelled crane cable as described in section 3.1 is validated by a Java Script which describes the displacements of a double elastic pendulum shown in figure C.1 [11]. The first $9\ s$ of the system with three different initial conditions is checked, respectively shown in figures C.2, C.3 and C.4:

- $\theta_1 = \theta_2 = 0deg$
- $\theta_1 = 45deg$, $\theta_2 = 0deg$
- $\theta_1 = \theta_2 = 45deg$

Important to mention here is that the initial elongation is not considered in the initial conditions of the double pendulum in the Java script. Therefore, as described before, even when both $\theta's$ are set to be zero, a z-directional oscillation occurs, around the pre-tensioned length, as can be seen in figure C.2. From these three figures further can be seen that the MATLAB model coincides well with the results gained from the Java script. It therefore proves that this part of the model is correct.

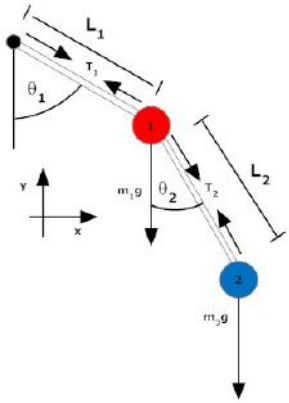

Figure C.1: Double pendulum, used to validate model [11]

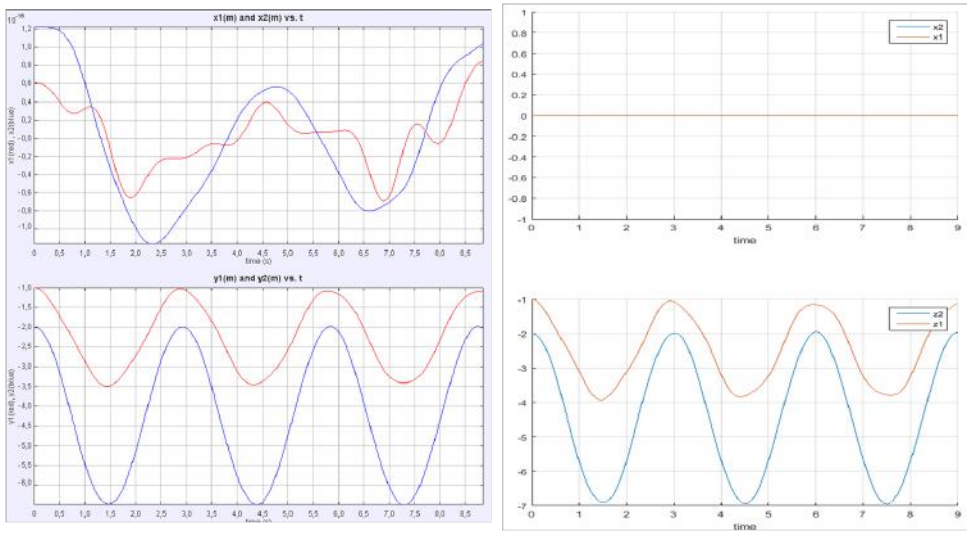

Figure C.2: Validation by Java Script, $\theta_1 = \theta_2 = 0deg$

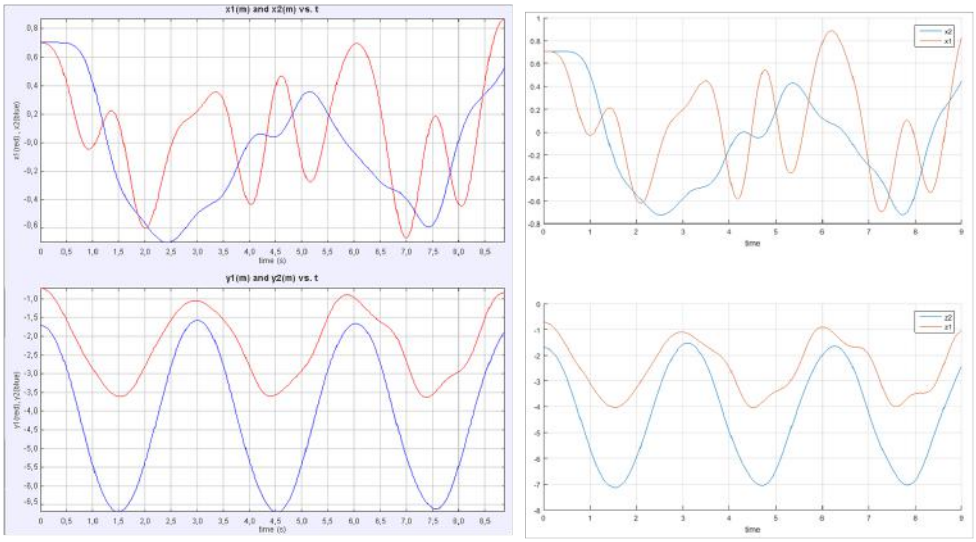

Figure C.3: Validation by Java Script, $\theta_1 = 45deg$, $\theta_2 = 0deg$

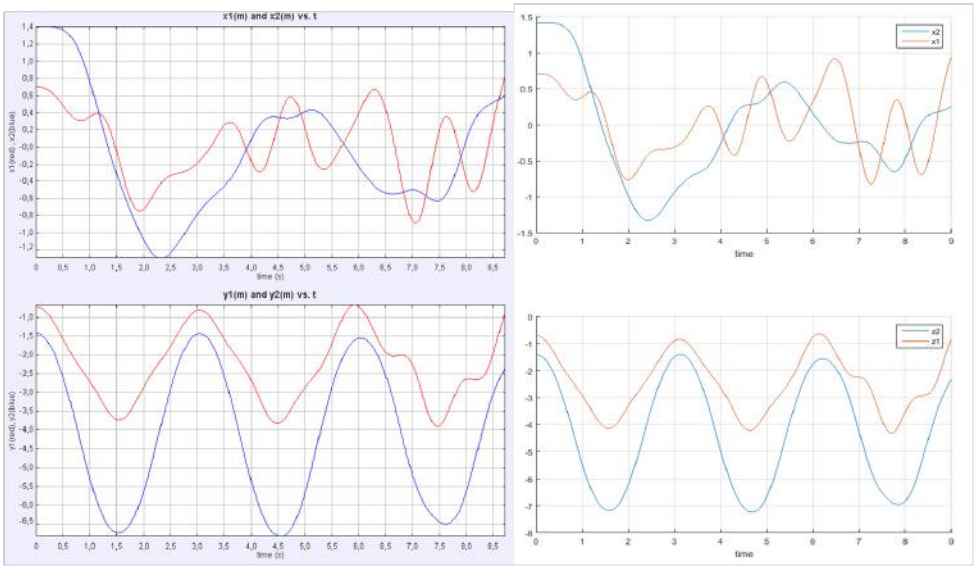

Figure C.4: Validation by Java Script, $\theta_1 = \theta_2 = 45deg$

Appendix D

Numerical errors in MATLAB crane model

In this appendix the numerical errors in the crane model are shown and discussed: when a system is held in rest position, displacements and velocities should remain zero. However, as was mentioned in chapter 3, both MATLAB and some of the initial position determinations cause small errors which result in oscillations in displacements of the degrees of freedom. The errors that are observed are very small though, and considered negligible in this thesis.

This first example is given in addition to the numerical error encountered in the load cable, which has been mentioned in section 3.1. Once more cable elements are added to the system, which is shown in figure D.1, the behaviour of the elastic pendulum changes, due to the changing mass distribution. Both the magnitude of the error and the time instant when the growth stops are lower with an increasing amount of cable elements. Obviously, the time for the solver to do its work increases with this number too, due to the fact that more degrees of freedom are added to the system.

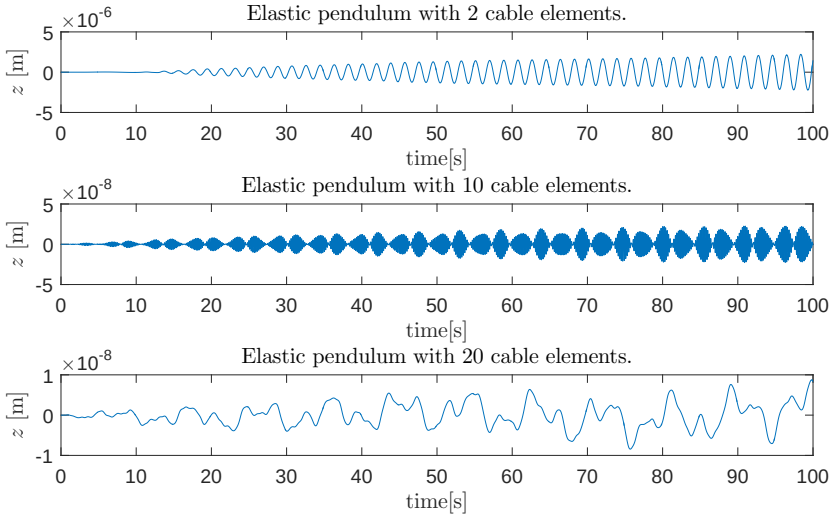

Figure D.1: Numerical error in vertical displacements elastic pendulum for multiple elements

When the crane boom is added to the model, numerical errors once again slightly affect the system. For a load cable with only one element, the crane boom rotation and x-and z-displacements of the hook are shown in figure D.2.

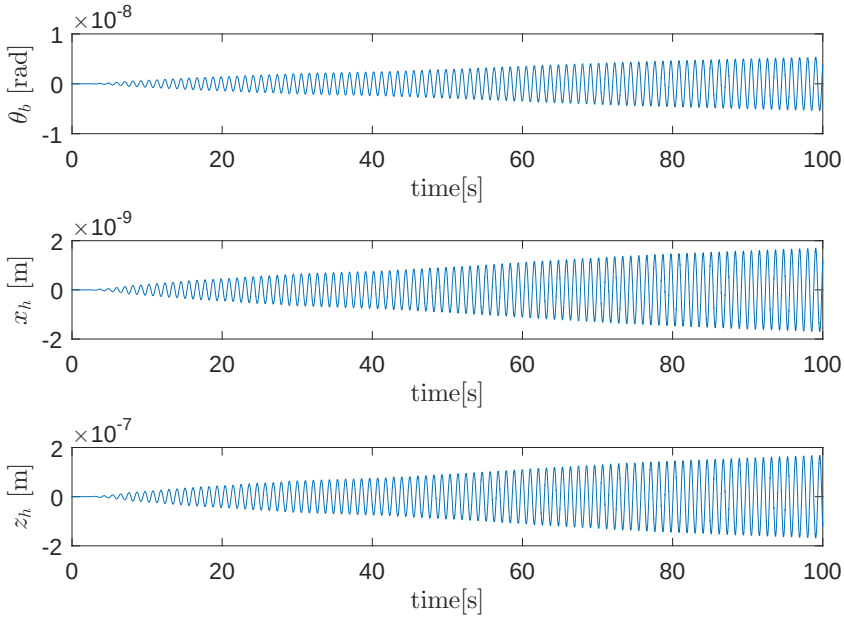

Figure D.2: Numerical error in rotation of the crane boom and displacements of the hook with one load cable element

When more load cable elements are added, which is done in figure D.3, the behaviour changes: the amplitude of the displacements is lowered drastically and its growth stops more rapidly. Furthermore, a more striking change is the behaviour of the x-directional hook displacement: it seems not to have a smooth sinusoidal line and it oscillates around a small offset. This could possibly be explained by the fact that the rotation of the boom, causing the x-displacement of the hook, has to travel through all the elements in the load cable, creating a wave in the load cable. The small delay that this modelled transmission causes, could cause a small phase difference.

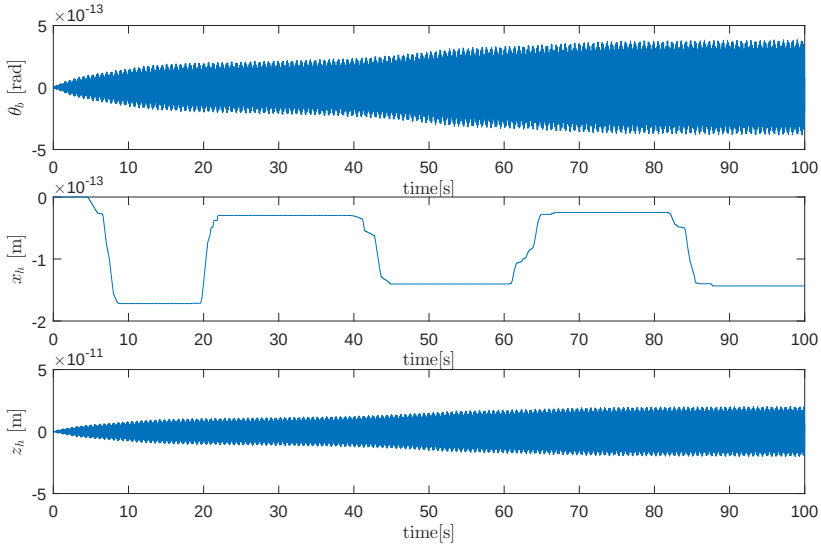

Figure D.3: Numerical error in rotation of the crane boom and hook displacements with 10 load cable elements

In figure D.4, a plot is given for the rotation of the crane boom θ_b, the x- and z-displacements of the hook (respectively x_h and z_h) and the displacements of the square (respectively x_j, z_j and θ_j). No external forces nor initial displacements and 10 load cable elements are used in calculation. As can be seen, the numerical errors which have been discussed for each of the elements are clearly seen in the system's behaviour. Looking at the magnitudes however, these errors will have a negligible effect on the system's outcomes once forces are added.

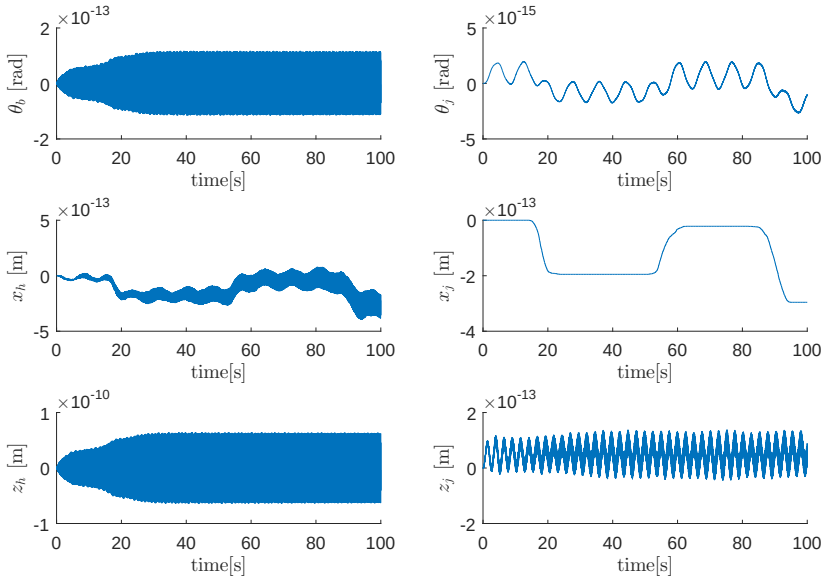

Figure D.4: Numerical error in rotation of the crane boom, and hook and square displacements, with 10 load cable elements

Appendix E

Stick model

In this appendix, the stick model is explained, which is used in order to generate equivalent diameters from the jacket's upper part. These diameters are required in Morison's equations.

The first step in determining these diameters via this method is to project each member onto a line parallel to the x-axis, according to Dubbers[13]. Therefore, only the horizontal load components are considered, as was explained in 4.1.1. A consequence of this assumption is that only the angle between the member axis and its projection perpendicular to the wave propagation will be used (β_b):

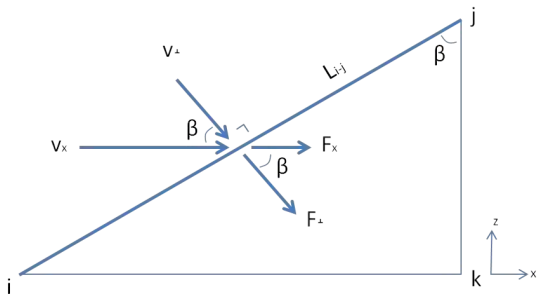

Figure E.1: Projection of the member onto line parallel to x-axis

The kinematics and the forces in Morison's equation can now be subdivided in forces in line of the wave direction and forces perpendicular to the wave direction, which are related through this angle β_b:

$$\begin{aligned} F_D &= F_{D\perp} \cos\beta_b; \\ F_I &= F_{I\perp} \cos\beta_b; \\ v_\perp &= v_x \cos\beta_b; \\ a_\perp &= a_x \cos\beta_b \end{aligned} \tag{E.1}$$

So, if angle β_b is zero, the member is perpendicular to the wave direction and $v_\perp = v_x$. If the angle is $90\ deg$, the member is parallel with the flow and $v_\perp$ is zero. Using these properties, the drag-and inertia forces perpendicular to the member can be rewritten to those in line with the wave direction and in terms of angle β_b (Morison in its general sense is used here):

$$\begin{aligned} F_D &= \frac{1}{2}\rho v_x |v_x| C_d D L_{i-j} \cos^3\beta_b; \\ F_I &= \frac{1}{4}\rho\pi D^2 a_x C_a L_{i-j} \cos^2\beta_b \end{aligned} \tag{E.2}$$

These member forces should be identical to the forces that will occur on that same element, using equivalent diameters D_d and D_a (for drag and inertia respectively) and an equivalent elevation E (the upper- minus the lower boundary of the range were the member resides):

$$\begin{aligned} F_{De} &= \frac{1}{2}\rho v_x |v_x| C_d D_d E; \\ F_{Ie} &= \frac{1}{4}\rho\pi D_a^2 a_x C_a E \end{aligned} \tag{E.3}$$

Now, by setting these equations equal to each other, the equivalent diameters can easily be subtracted:

$$\begin{aligned} D_d &= D\frac{L_{i-j}}{E} \cos^3\beta_b; \\ D_a^2 &= D^2\frac{L_{i-j}}{E} \cos^2\beta_b \end{aligned} \tag{E.4}$$

This procedure is to be done for each individual member per range of elevation. By simply adding the equivalent diameter for all member within that range, the total equivalent diameter is found.

As an example, this method is performed for one range of elevations (E) containing four legs, four braces in the $x-z$-plane, and four braces in the $y-z$-plane. The batter angle is not taken into account, which indicates that the legs are assumed to be in line with the $x-z$-plane. All elements that are to be considered in the equivalent diameter for that elevation range are shown in figure E.2.

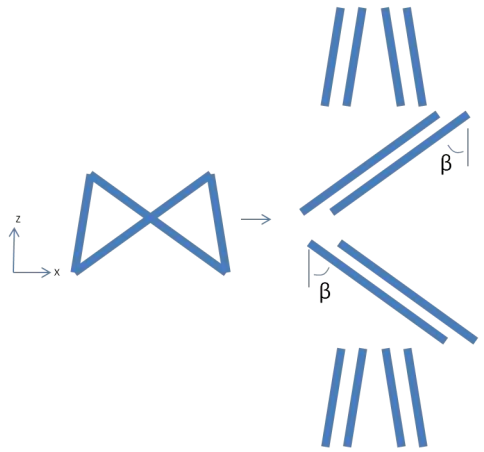

Figure E.2: Stick model method on a range of elevations

Firstly, the legs are quite simple assuming near verticality: Δx, Δy and β_b are 0, so $D_d = D_a = D$.

The diagonal members in the near vertical plane, parallel to the wave direction are to be calculated as was explained before: $\Delta y = 0$, $L_{i-j} = \sqrt{\Delta x^2 + \Delta z^2}$. Inserting this in equations E.4 and rewriting gives $D_d = D\cos^2\beta_b$ and $D_a^2 = D^2\cos\beta_b$.

The last four members: the diagonals perpendicular to the wave direction have Δx and $\beta = 0$ and $L_{i-j} = \sqrt{\Delta y^2 + \Delta z^2}$. Therefore $D_d = D\frac{\sqrt{\Delta y^2+\Delta z^2}}{\Delta z}$ and $D_a^2 = D^2\frac{\sqrt{\Delta y^2+\Delta z^2}}{\Delta z}$.

The total equivalent diameters for this range of elevation is derived by adding up all outcomes.

Appendix F

Determination of the reference x-coordinate for submergence calculations

In this appendix, the approach on how to calculate the reference x-coordinates for submergence calculations is given.

As was explained in section 4.1.2, the representative x-coordinate used for the wave kinmatic calculations is considered to be that in the middle of the submerged part of the jacket component's centerline. In order to determine this coordinate, first the intersection of the centerline with the MSL is to be determined. This x_0 coordinate can be calculated using the known mid-top coordinates, x_t and z_t and the angle in which the jacket is positioned, θ_j, by means of equation F.1a. Once this coordinate is known, the coordinate of interest, x, can be calculated using the element's bottom coordinate z_b in equation F.1b or F.1c, in case the element is partially- or fully submerged respectively. In case the element is fully submerged, indicates coordinate (x_t, z_t) is positioned below MSL.

$$x_0 = x_t + z_t \tan(\theta_j) \tag{F.1a}$$

$$x = x_0 + \frac{|z_b|}{2} \tan(\theta_j) \tag{F.1b}$$

$$x = x_t + \frac{(z_t + |z_b|)}{2} \tan(\theta_j) \tag{F.1c}$$

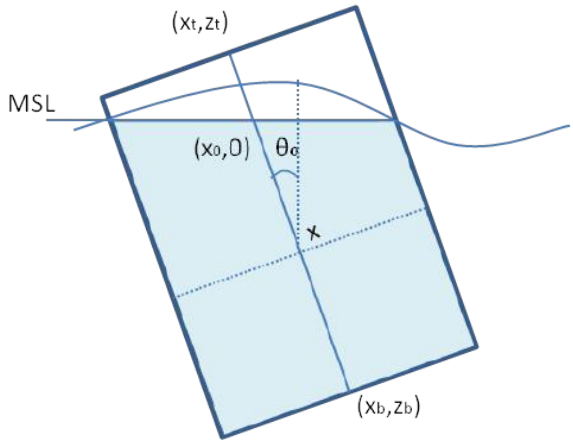

Figure F.1: Reference x-coordinate

Appendix G

Derivation of Drag- and Inertia coefficients

In this appendix, respectively a number for the drag-and inertia coefficients are derived, which are needed in Morison's equation, described in section 4.1.

The drag coefficient C_d is a dimensionless quantity used to quantify the drag or resistance. It depends on several factors: the Reynolds number (R_e), the surface roughness (k_s) and the Keulegan Carpenter number (K_c).

The most important factor is the Reynolds number, which can be calculated by dividing the relative object-water velocity times the diameter by the kinematic viscosity ($\nu = 1.19 \cdot 10^{-6} \frac{m^2}{s}$ for sea water of 15^oC). Figure G.1a shows the coefficient for different Reynolds numbers: for R_e between 10^2 and 10^5, C_d for cylinders is 1.05, then it shows a distinct drop (critical flow regime) and from R_e=10^6 it climbs up again. The critical flow regime depends on the non dimensional surface roughness $\Delta = \frac{k_s}{D}$ of a cylinder (figure G.1b): it shifts the dropping point in between the range of $R_e = 10^5$ to 10^6.

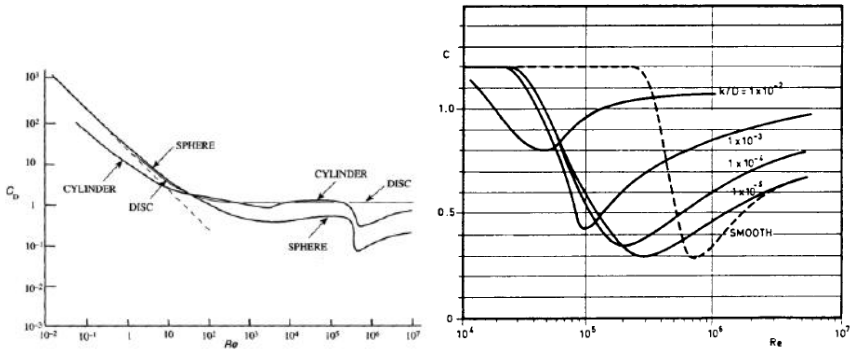

(a) C_d vs R_e **(b)** Critical flow regime

Figure G.1: Drag coefficient

Since the critical regime is hard to define, it is chosen to use a drag coefficient of 1.05 in the regime where $R_e < 5 \cdot 10^5$ (in-dependable of roughness and K_c). For regimes exceeding that value for R_e, equations G.1 to G.4 will be used. For painted steel, k_s of $5 \cdot 10^{-6}$ is used, which, as well as the equations used, is based on guidelines by DNV [9].

$$C_d = C_{ds}(k, R_e)\psi_w(K_c) \tag{G.1}$$

$$C_{ds}(\Delta) = \begin{cases} 0.65 & \text{if } \Delta < 10^{-4} \text{ (smooth)}; \\ \frac{29+4\log_{10}(\Delta)}{20} & \text{if } 10^{-4} < \Delta < 10^{-2}; \\ 1.05 & \text{if } \Delta < 10^{-2} \text{ (rough)}. \end{cases} \tag{G.2}$$

In order to find the actual drag coefficient, which might differ from the steady value, the wake amplification factor (ψ_w) is to be used. This factor depends on both C_{ds} and K_c and is given as:

$$\psi_w(K_c) = \begin{cases} C_\pi + 0.1(K_c - 12) & \text{if } 2 \leq K_c < 12; \\ C_\pi - 1 & \text{if } 0.75 \leq K_c < 2; \\ C_\pi - 1 - 2(K_c - 0.75) & \text{if } K_c \leq 0.75. \end{cases} \tag{G.3}$$

$$C_\pi = 1.5 - 0.024(\frac{12}{C_{ds} - 10}) \tag{G.4}$$

Due to the fact that irregular waves are considered, K_c is to be calculated using the zero crossing period T_z and the standard deviation of the water particle velocities of each wave component (σ_u). The equation for K_c is given in equation G.5. σ_u is calculated using the formula for standard deviation, given in equation G.6, with μ_u being the mean value of the horizontal velocities on that element.

$$K_c = \frac{(\sqrt{2}\sigma_u)T_z}{D} \tag{G.5}$$

$$\sigma_u = \sqrt{\frac{1}{N}\sum_{i=1}^{N}(u_i - \mu_u)^2} \tag{G.6}$$

The added mass coefficient C_a is a non-dimensional added mass, represented by dividing the added mass per unit length by the cross sectional area times density. It too depends on K_c the surface roughness, and for K_c's higher than 3 on the steady value of the drag coefficient.

$$C_a = \begin{cases} 1 & \text{if } K_c < 3; \\ \max\left\{ \begin{array}{l} 1 - 0.044(K_c - 3); \\ 0.6 - (C_{ds} - 0.65) \end{array} \right\} & \text{if } K_c > 3. \end{cases} \tag{G.7}$$

Appendix H

Bucket heave added mass

In this appendix, the heave added mass of the fully submerged bucket, a_{33} is calculated, by making use of the disk added mass described in DNV [9]. The maximum value of added mass is built op by that of the bucket itself and the water that is entrapped within it. It therefore depends on the ventilation hole, since water that can escape through this hole, does not displace water in vertical direction. The relation between added mass of a non perforated disk (a_{33S}) and the one of a perforated structure (a_{33}) is given by equation H.1 (p describes the rate of perforation):

$$\frac{a_{33}}{a_{33S}} = \begin{cases} 1 & \text{if } p < 0.05; \\ 0.7 + 0.3\cos(\pi \frac{(p-0.05)}{0.34}) & \text{if } 0.05 < p < 0.34; \\ e^{\frac{0.1-p}{0.28}} & \text{if } 0.34 < p < 0.50. \end{cases} \tag{H.1}$$

The total added mass in case of a bucket is built up from calculations of that of a two-dimensional disk (a_{33_0} in equation H.2), amplified with a term that states the height of the structure (λ_h) and amplified with the above mentioned perforation influence. The entrapped water volume inside the bucket is to be included in the added mass by adding its mass to that of the disk, as can be seen in H.3.

$$a_{33_0} = \rho_w \frac{2}{\pi}\frac{4}{3}\pi\left(\frac{1}{2}D_{out}\right)^3 \tag{H.2}$$

$$a_{33S} = \left(1 + \sqrt{\frac{1-\lambda_h^2}{2(1+\lambda_h^2)}}\right) a_{33_0} + \tfrac{1}{4}\pi h_{bi}(D_{in})^2\rho_w \quad \text{with } \lambda_h = \frac{\sqrt{\frac{1}{4}\pi D_{out}^2}}{H_{buck}+\sqrt{\frac{1}{4}\pi D_{out}^2}} \tag{H.3}$$

Appendix I

Derivation suction in exiting buckets

In this appendix the derivation of the first order differential equation needed to solve the suction force within the buckets while they exit is given. This phenomena is treated in section 4.4.3. Terms used are given in figure I.1.

The pressure of the air pocket, $P_s(t)$, consist out of the atmospheric pressure and a dynamic variation term $\mu_s(t)$. This time however, an under-pressure is created, causing the second term to have a negative influence upon the total pressure:

$$P_s(t) = P_{atm} - \mu_s(t) \tag{I.1}$$

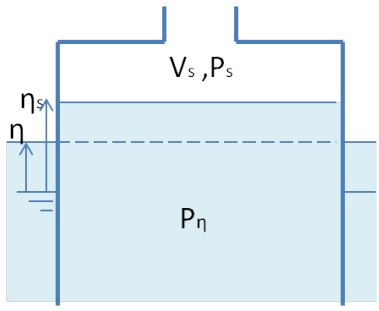

Figure I.1: Air pocket formation during bucket exit

The acquired air pocket pressure $P_s(t)$ is to be set equal to that of the water line inside the bucket, $P_\eta(t)$:

$$P_\eta(t) = P_{atm} + \rho_w g\eta(t) - \rho_w g\eta_s(t) \tag{I.2}$$

By setting these pressures equal to each other, the waterlevel inside the bucket $\eta_s(t)$ can be determined:

$$\eta_s(t) = \eta(t) + \frac{\mu_s(t)}{\rho_w g} \tag{I.3}$$

The dynamic pressure $\mu_s(t)$ describes the suction in the bucket. In order to be able to calculate this dynamic pressure, the air flux into the bucket should be determined using both the continuity equation (equation I.4) and the rewritten Bernoulli's equation (equation I.5):

$$\rho_s(t)Q_{in}(t) = \frac{d\rho_s(t)}{dt}V_s(t) + \rho_s(t)\frac{dV_s(t)}{dt} \tag{I.4}$$

$$Q_{in}(t) = A_v\sqrt{\frac{2\mu_s(t)}{\rho_{air}}} \tag{I.5}$$

Likewise as was done in the derivation of the air cushion pressure during splash zone entry, some assumptions are made regarding the air- and water behaviour: the air is considered to be an adiabatic, compressible ideal gas and water is considered to be incompressible.

Due to these assumptions, the air pocket density can be calculated via the isentropic relation, which is given in equation I.6. Filling in $P_s(t)$ and differentiating it over time gives the derivative in equation I.7.

$$\rho_s(t) = \rho_{air}\left(\frac{P_s(t)}{P_{atm}}\right)^{\frac{1}{\gamma_a}} \tag{I.6}$$

$$\frac{d\rho_s}{dt} = -\rho_{air}\frac{1}{\gamma_a P_{atm}}\dot{\mu}_s(t)\left(1 - \frac{\mu_s(t)}{P_{atm}}\right)^{\frac{1}{\gamma_a}-1} \tag{I.7}$$

The instantaneous volume of the air pocket and its derivative over time are given in equation I.8 and I.9. Here, h_{top} is the global z-coordinate of the associated inner bucket top.

$$V_s(t) = A_{ti}(h_{top} - \eta_s) \tag{I.8}$$

$$\begin{aligned} V_s &= A_{ti}(z_{tot} + z_j + \sin(\theta_j)x_{L0} + \cos(\theta_j)z_{L0} - v_c t - \eta - \frac{\mu_s}{\rho_w g}); \\ \frac{dV_s}{dt} &= A_{ti}(\dot{z}_j + \cos(\theta_j)\dot{\theta_j}x_{L0} - \sin(\theta_j)\dot{\theta_j}z_{L0} - v_c - \dot{\eta} - \frac{\dot{\mu_s}}{\rho_w g}). \end{aligned} \tag{I.9}$$

Filling the acquired terms in into the continuity equation given in equation I.4, makes it able to subtract the derivative of the dynamic pressure inside the air pocket. This formulation is given in the text in section 4.4.3, in equation 4.36. For each bucket, an extra degree of freedom is added to the model, in order to be able to solve this differential equation.

Appendix J

Bucket in proximity of the seabed

As was explained in section 4.6, as soon as the buckets reach close proximity of the seabed, three phenomena occur according to DNV [9]:

- Changes in added mass;
- Change in drag terms;
- Hydrodynamic pressure build up inside the buckets.

In the model these forces are implemented, but since their asymptotic behaviour in close range of the seabed is not nullified by the decreasing lowering velocity of the crane, it is chosen to stop the solver when the buckets are approximately 30% of their diameter from the seabed. Since these forces act in the vertical direction though, they are of importance for the load cable forces. Therefore they are still considered in the model, for further usage.

The determination and implementation of the three phenomena mentioned are discussed in this appendix:

J.0.1 Changes in added mass near bottom

Due to the fact that the seabed introduces a boundary layer for the surrounding water to escape to, the heave added mass of the buckets will be affected in this region. This change induces two phenomena: the most obvious one is the influence it has upon the structure's added mass and thus upon inertial forces. Secondly,

the sudden change in magnitude induces an extra upward force, which is given by equation J.1:

$$F_e = \frac{1}{2}\frac{da_{33}}{dh_b}v_b^2 \tag{J.1}$$

Here, h_b describes the distance to the seabed and v_b the vertical bucket velocity. So in order to be able to calculate this force, the added mass should be written in terms of h_b. For a circular disk, the behaviour near the seabed is modelled by StatiolHydro in 2007 [33]. Their outcomes are shown in figure J.1a. Using the points indicated in this figure and fitting a curve using the curve fitting tool in MATLAB, an approximate formula can be generated for the dependency. This curve fit is shown in figure J.1b and its formulation is given in equation J.2.

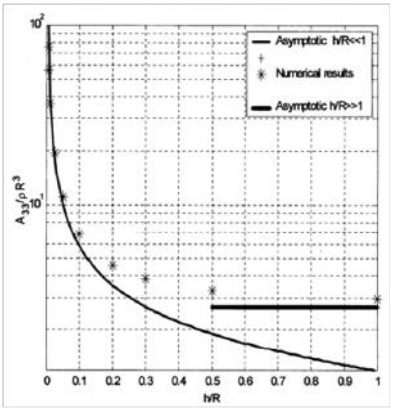

(a) According to model testing by Statoil [33]

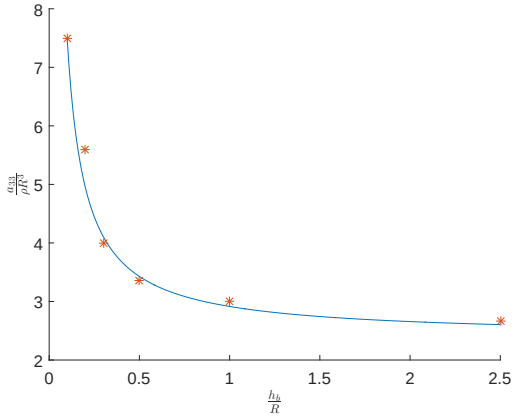

(b) Approximation used in model

Figure J.1: Change in added mass of a disk in proximity of seabed

$$\frac{a_{33}}{\rho_w R^3} = 0.52\left(\frac{h_b}{R}\right)^{-0.99} + 2.395 \tag{J.2}$$

The disk added mass can be rewritten for the added mass of the entire bucket, as was done before and is explained in appendix H (equations H.1 to H.3).

As can be seen in figure J.1b, the slope of the graph for $\frac{h_b}{R}$ smaller than approximately 0.3 rapidly increases. This results in the derivative of the heave added mass to reach huge values once the bucket is close to the bottom. Following equation J.1, the force induced by this change will therefore automatically largely increase too. The only way to limit the forces upon the system therefore is to lower the lowering velocity of the crane. In order to be really accurate, the velocity within the model should therefore be adapted. This asymptotic effect resulted in the decision to stop the solver once the buckets are approximately 30% of their diameter from the seabed.

J.0.2 Changes in drag terms near bottom

The interaction with the seabed affects the drag terms too. The closer the structure gets to the seabed, the higher the drag coefficient will be. DNV [8] shows this dependency for a circular cylinder (figure J.2a). Unfortunately, an alternative dependency which could be linked to the bucket geometry more properly could not be found. However, due to the fact that the drag coefficient for the cylinder only gets twice as high, this dependency will be used for the bucket geometry as an approximation.

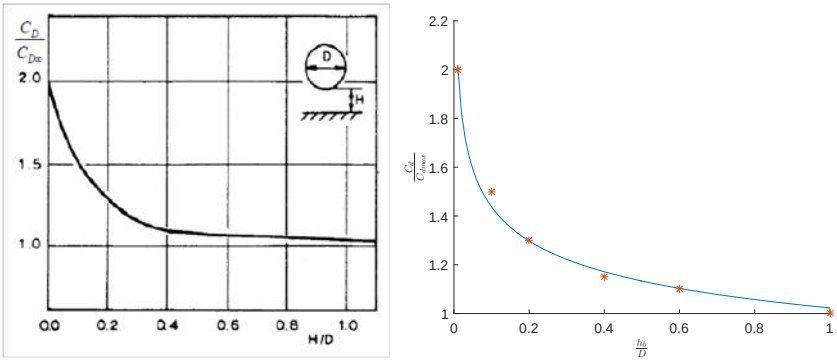

(a) According to DNV [8] **(b)** Approximation used in model

Figure J.2: Change in drag coefficient of a cylinder in proximity of seabed

Like was done with the determination of equation J.2, some points in figure J.2a are taken as a reference to come up with a curve fitted approximate equation for the changing drag coefficient. The outcome is shown in figure J.2b and its equation is given in equation J.3. Once the buckets reach a distance of one times the bucket

diameter to the seabed, the vertical drag coefficient starts to increase, as does the vertical drag force.

$$\frac{C_d}{C_{d\infty}} = 1.023 \left(\frac{h_b}{D} \right)^{-0.1477} \tag{J.3}$$

Especially for this drag term applies that the influence on the system will be minimum, since drag in that water depth is almost zero. The forces that are related to the velocity term will therefore be dominated by the force treated before, F_e.

J.0.3 Hydrodynamic bucket pressure near bottom

The last phenomena in this region is the hydrodynamic pressure build up within the buckets. This pressure increases because of the fact that the area for the water evacuation decreases, as is shown in figure J.3. In order to be able to calculate this pressure, the flow velocity of the water escaping the bucket, v_{flow}, should be determined. This can again be done using the continuity equation, as was done for the air cushion in equation 4.18. This time though, the density of water is considered, which, due to its incompressibility is constant over time. Therefore the continuity equation reduces to equation J.4.

$$Q_{out} = \frac{dV_w}{dt} \tag{J.4}$$

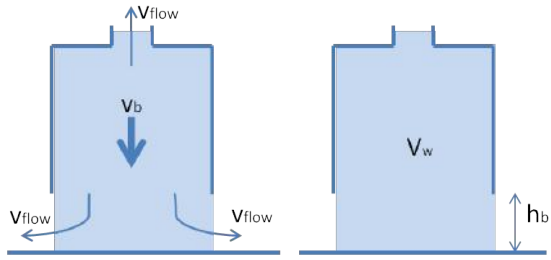

Figure J.3: Velocities and trapped water volume near seabed

As can be seen in figure J.3, the total entrapped volume of water, V_w, depends on h_b. This distance can be written in terms of the water depth and the global z-coordinate of the bottom of the bucket in question. By adding this number to the inner bucket height, and multiplying it with the horizontal inner bucket area,

V_w can easily be calculated by equation J.5a. When differentiated over time, the velocity terms can be recognised to be equal to the bucket's downward velocity v_b, as is shown in equation J.5b

$$V_w = A_{ti}\left(h_{bi} + d + z_{tot} + z_j + \sin\left(\theta_j\right)x_{L0} + \cos\left(\theta_j\right)z_{L0} - v_c t\right); \tag{J.5a}$$

$$\frac{dV_w}{dt} = A_{ti}\left(\dot{z}_j + \cos\left(\theta_j\right)\dot{\theta_j}x_{L0} - \sin\left(\theta_j\right)\dot{\theta_j}z_{L0} - v_c\right) = A_{ti}v_b \tag{J.5b}$$

The outward flux Q_{out} further equals the outward velocity (v_{flow}) times the outward area, consisting of the ventilation hole area and the bottom escape area. This latter area in reality relies on the interaction with the soil: it depends on the extent of mobilisation of the soil due to the water flow. However, for simplicity reasons here it is assumed that the soil does not mobilise at all; the mobilisation depends on soil parameters, which are site specific. Hence, the area from which the water can escape underneath the bucket can be calculated by multiplying h_b with the circumference of the bucket. Inserting this in in the continuity equation, the outward flow velocity can be calculated using equation J.6.

$$(CA_v + \pi D_b h_b)v_{flow} = A_{ti}v_b \tag{J.6}$$

The pressure that is induced by this outward velocity flow can simply be calculated using Bernoulli's equation and is given in equation J.7. k_{flow} here is the pressure loss coefficient of the ventilation hole, which is directly linked to the contraction coefficient. When multiplied with the inner (perforated) bucket top area, the force this hydrodynamic pressure induces upon the bucket is calculated.

$$P_w = \frac{1}{2}k_{flow}\rho_w v_{flow}^2 \qquad \text{with} \qquad k_{flow} = \left(\tfrac{1}{C} - 1\right)^2 \tag{J.7}$$

Appendix K

Miscellaneous simulation results

In this appendix more examples of particular jacket behaviour are given, in addition to those given in section 5.2.

Firstly, two more examples for which DAF remains below 1 are shown:

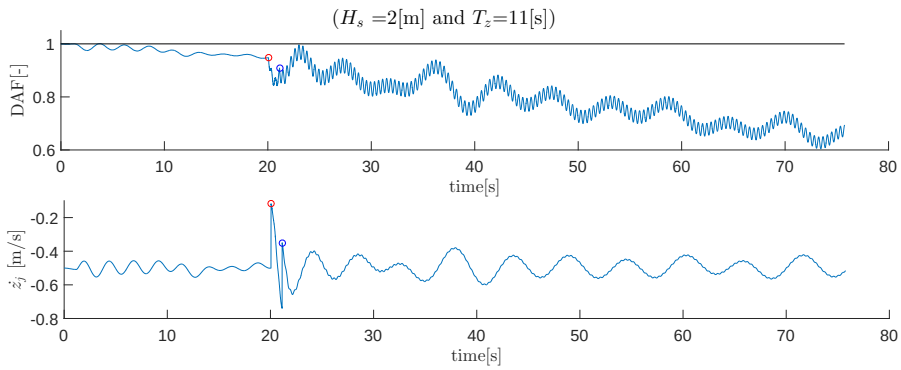

Figure K.1: Case with DAF remaining below 1

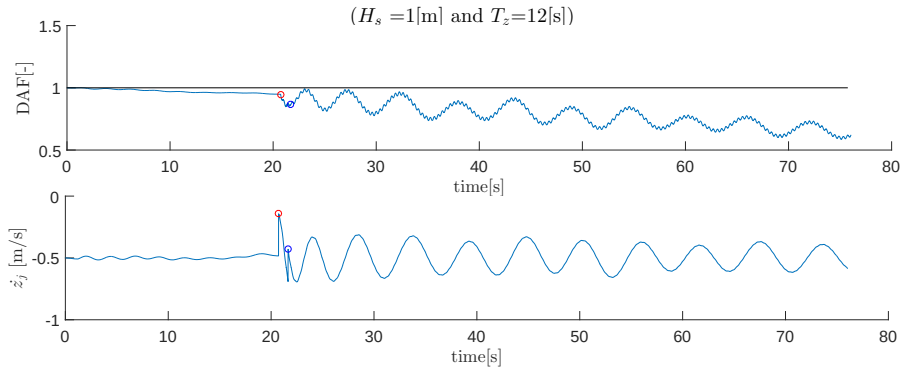

Figure K.2: Case with DAF remaining below 1

Below, three more examples that state the importance of slamming timing and magnitude are given. In all examples, the simulation is repeated with slamming switched off (in red), in order to show the actual influence it has on the outcomes.

Firstly, another example of simultaneous slamming is given in figure K.3. The upper figure shows the load cable DAF for the first $50\ s$ and the lower figure shows the vertical velocity of the jacket's COG. Again, the fact that both bucket slamming instants follow each other at almost the exact same time enforce a huge vertical velocity jump of the jacket. This jump reaches such large proportions, that the vertical velocity of the jacket switches sign and turns positive. Physically this means that the jacket is lifted upwards with the waves for a while (however, not to such an extend that slack line is reached). These upward displacements force the jacket into oscillating in the crane with a large amplitude, causing the DAF to exceed its maximum value.

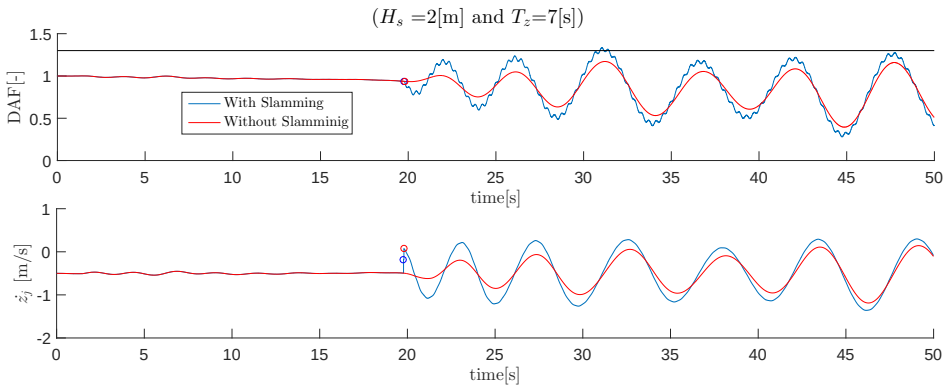

Figure K.3: Case with exceeding DAF due to simultaneous slamming

In figure K.4, a case is pointed out where the left bucket slams twice; apparently the assumption made, that a lowering velocity of $0.5\ \frac{m}{s}$ is sufficiently high to prevent multiple slamming to occur is questionable. Again, this phenomena results into large displacements, oscillation magnitudes and thus load cable forces.

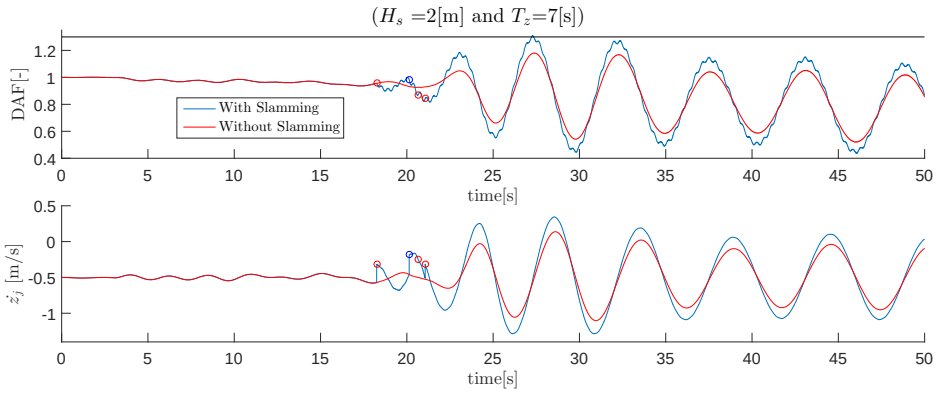

Figure K.4: Case with exceeding DAF due to multiple slamming

Figure K.5 shows a case where the effect of high magnitude slamming combined with timing can clearly be seen. For these conditions, the relative velocity between the water and left bucket reaches such a high level, that the collision with this bucket causes the jacket to be lifted up by the waves, like was observed two cases before. Again, the vertical displacements caused by this large slamming results in high amplitude rotational oscillations which cause the DAF to exceed its maximum allowable value. Even though the timing of the second slam is such as discussed in the case where the DAF remained below 1, the fact that the jacket oscillates in the same phase as the wave forces still enforces the behaviour.

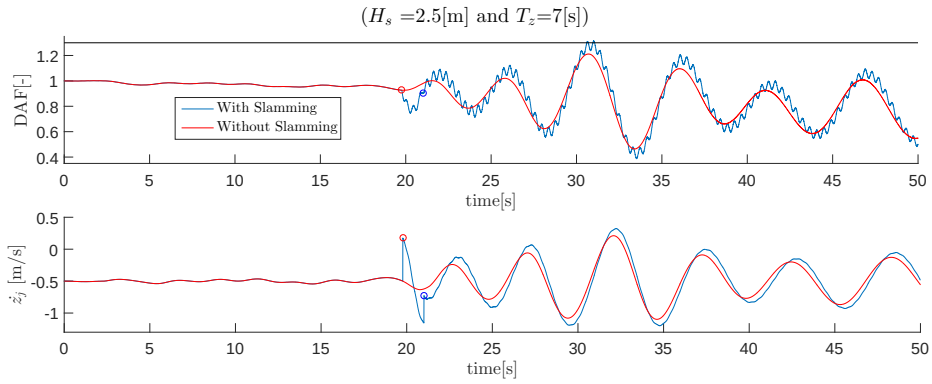

Figure K.5: Case with exceeding DAF due to high magnitude slamming

Appendix L

Probabilities of intolerable DAF values

In this appendix for all wave combinations of interest the characteristics of the Weibull distribution are used in order to calculate the probabilities of intolerable maximum DAF values, together with the 95% confidence bounds. The error herein is quite large, since only 15 or 50 seeds are used, in accordance to table 5.2.

	$H_s = 0.5$ [m]		
T_z [s]	**Probability DAF $\geq$ 1.3**	**Upper bound**	**Lower bound**
4	2.1%	2.9%	1.4%
5	0.5%	1.0%	0.1%
6	0.1%	1.5%	0.0%
7	0.0%	0.4%	0.0%
8	0.0%	0.8%	0.0%
9	0.0%	0.0%	0.0%
10	0.0%	0.1%	0.0%
11	0.0%	0.0%	0.0%
12	0.0%	0.0%	0.0%
13	0.0%	0.0%	0.0%

Table L.1: Probabilities H_s=$0.5m$

	$H_s = 1$ [m]		
T_z [s]	**Probability DAF $\geq$ 1.3**	**Upper bound**	**Lower bound**
4	26.0%	36.1%	16.9%
5	5.6%	12.4%	1.8%
6	1.0%	11.4%	0.0%
7	0.2%	1.5%	0.0%
8	0.0%	2.7%	0.0%
9	0.0%	0.0%	0.0%
10	0.0%	0.3%	0.0%
11	0.0%	0.0%	0.0%
12	0.0%	0.0%	0.0%
13	0.0%	0.0%	0.0%

Table L.2: Probabilities H_s=$1m$

	H_s = 1.5 [m]		
T_z [s]	**Probability DAF $\geq$ 1.3**	**Upper bound**	**Lower bound**
4	64.6%	74.3%	52.6%
5	18.7%	28.1%	10.9%
6	7.3%	14.6%	2.8%
7	2.0%	6.7%	0.4%
8	7.7%	23.5%	1.1%
9	0.0%	1.6%	0.0%
10	0.0%	3.2%	0.0%
11	0.0%	0.0%	0.0%
12	0.2%	6.7%	0.0%
13	0.0%	0.2%	0.0%

Table L.3: Probabilities H_s=1.5m

	H_s = 2 [m]		
T_z [s]	**Probability DAF $\geq$ 1.3**	**Upper bound**	**Lower bound**
4	85.9%	91.7%	76.4%
5	53.4%	64.0%	41.6%
6	21.5%	31.2%	13.2%
7	9.4%	17.4%	4.1%
8	5.3%	12.0%	1.7%
9	3.4%	9.1%	0.9%
10	1.4%	5.6%	0.2%
11	0.4%	3.0%	0.0%
12	2.0%	7.1%	0.3%
13	0.0%	0.3%	0.0%

Table L.4: Probabilities H_s=2m

	H_s = 2.5 [m]		
T_z [s]	**Probability DAF $\geq$ 1.3**	**Upper bound**	**Lower bound**
4	89.5%	96.6%	69.6%
5	84.6%	94.0%	63.3%
6	64.0%	80.3%	40.3%
7	24.1%	34.1%	15.3%
8	9.4%	17.2%	4.2%
9	1.3%	4.9%	0.2%
10	2.1%	13.1%	0.1%
11	2.5%	15.8%	0.1%
12	1.2%	9.7%	0.0%
13	0.7%	3.6%	0.0%

Table L.5: Probabilities H_s=2.5m

Appendix M

Lowering velocity analysis

In this appendix the Weibull cumulative probability plots are given in figure M.1, for the lowering velocities studied in section 5.4.1.

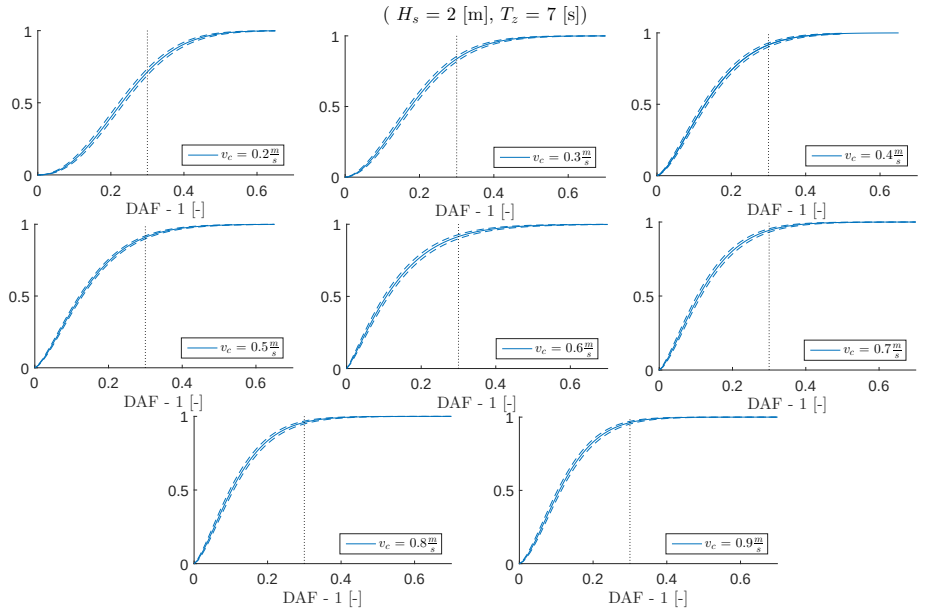

Figure M.1: Weibull cumulative probabilities, for different lowering velocities

In figure M.2 load cable DAF plots are given that show exceeding DAF values, for a v_c of 0.2, 0.4, 0.6 and 0.8 $\frac{m}{s}$. The lower velocities clearly show vertical wave amplified behaviour, without the first couple of oscillations being severe. For higher velocities, the large amplitudes are directly observed in the first oscillations, due to the magnitude or mutual timing of the slamming.

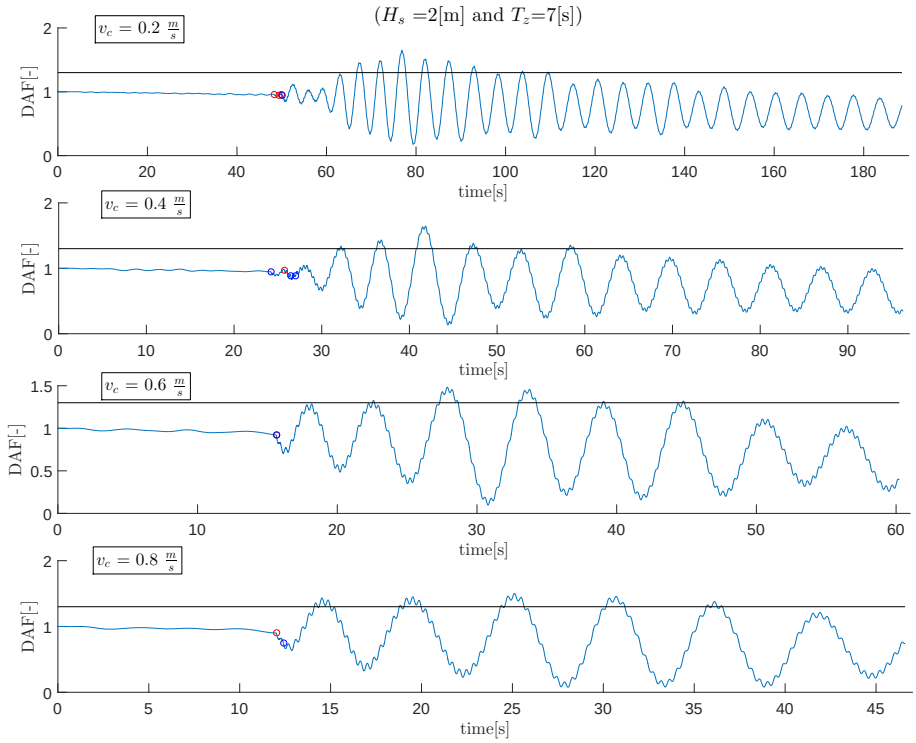

Figure M.2: Cases with exceeding DAF values, for different lowering velocities

Appendix N

Adjusting the crane lowering velocity

As an example to show the importance of adjusting ones crane velocity during installation, the displacements and velocities of the buckets are calculated in case the jacket would be submerged to a distance half the bucket's diameter from the seabed. Prior to that, the jacket is lowered with a constant velocity of $0.5\ \frac{m}{s}$. The calculations were stopped and the lastly acquired displacements and velocities were saved. Using these conditions as starting conditions, a new solver was started, with the lowering velocity set to zero. Figure N.1 shows the global z-coordinate of both bucket bottoms, as well as the load cable DAF, when the jacket is held in the same position for a period of $200\ s$. In the DAF behaviour it can be seen that the amplitudes only slightly decrease over time. The same can be observed for the vertical displacements of the buckets. The horizontal wave forces cause the jacket to remain rotated around its COG, causing the larger oscillation in the bucket displacements.

After a period of approximately $150\ s$ the buckets oscillate with an amplitude of $10\ cm$, merely 1 % of the bucket's diameter. Once this 'resting' position is fully adopted, the crane operator can slowly lower the jacket towards the seabed, e.g. with a lowering velocity of $0.1\ \frac{m}{s}$. Via this method, the effect the interactions the seabed have upon the structure could be minimized. As an example how this resting period affects the ratio of hydrodynamic forces over static forces in the load cable, figure N.2 shows two lines: both show the outcomes for the jacket being lowered with a constant $0.1\ \frac{m}{s}$, between the position calculations were stopped and the position where the bottoms of the bucket touch the soil. In the blue line, the period

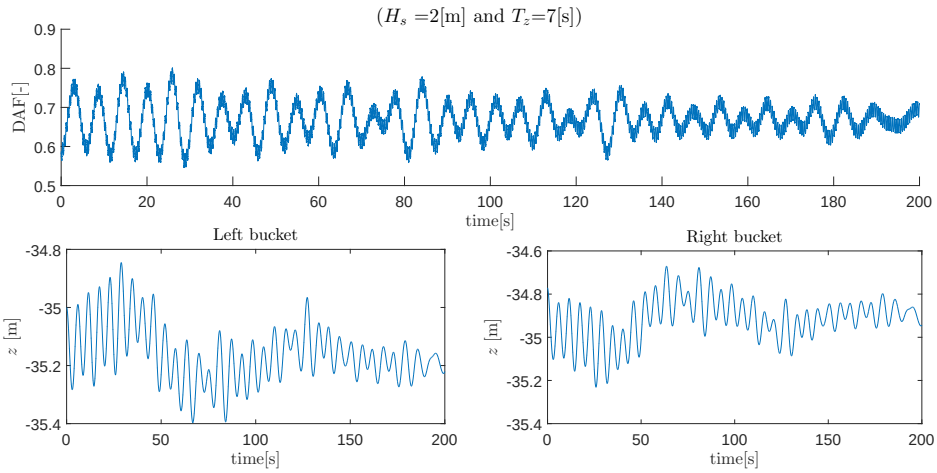

Figure N.1: Damping due to drag

of rest is incorporated: it starts after $150\ s$ and uses those displacements and velocities as initial conditions for further calculations. The red line on the other hand is lowered immediately after it is stopped; the initial conditions found as a start for figure N.1 are used in stead. Clearly, the latter simulation shows bigger amplitudes in dynamic forces, proving that such a rest period could be important.

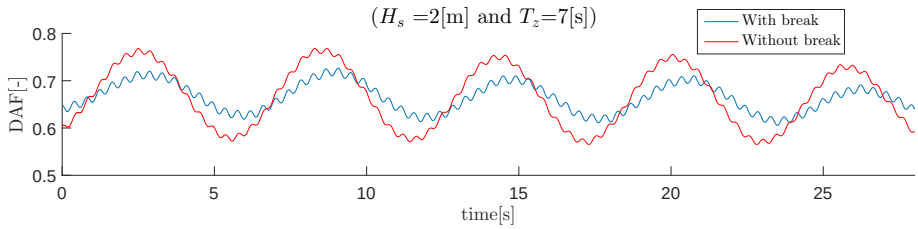

Figure N.2: The influence of a resting period, on the load cable DAF

Appendix O

Miscellaneous diffraction results

In this appendix, two more examples are given which show the influence of the Mac-Camy Fuchs correction on the DAF and horizontal displacement of the jacket, as was discussed in section 6.3.2. Firstly, the effect on a wave train with a period of 7 s is shown, followed by that with a period of 13 s. The effect observed on the DAF for both cases is negligible, but, especially for the higher period case, the effect on the horizontal displacements is quite severe.

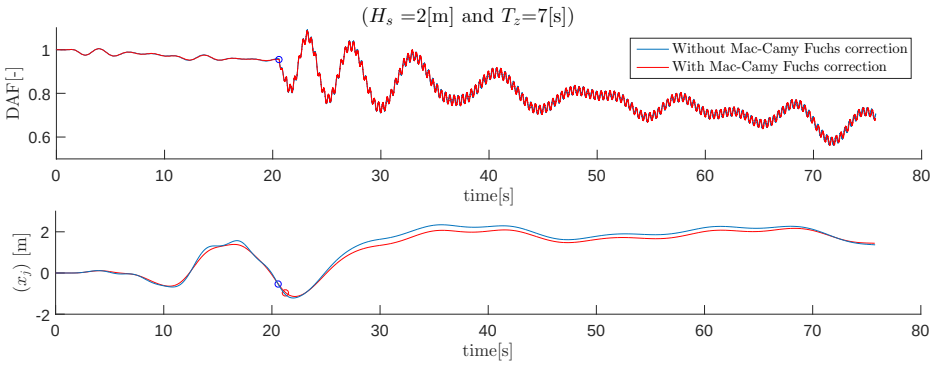

Figure O.1: The effect of the Mac-Camy Fuchs correction with T_z=7s

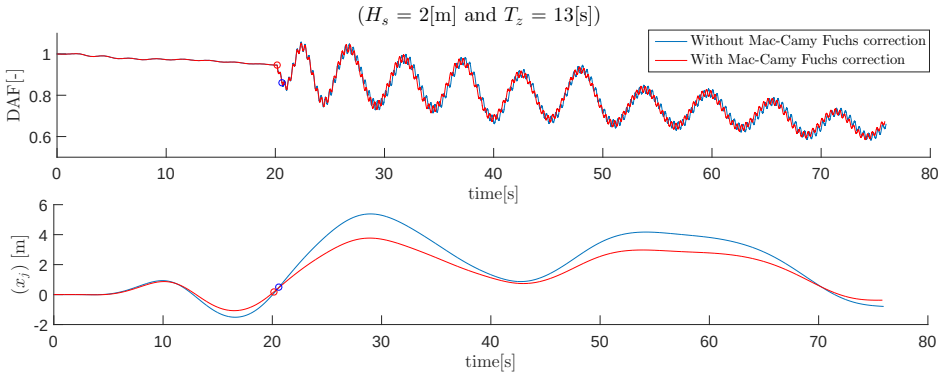

Figure O.2: The effect of the Mac-Camy Fuchs correction with $T_z = 13s$

Bibliography

[1] B. Barlas. Interactions of waves with an array of tandem placed bottom-mounted cylinders. *Journal of Marine Science and Technology*, 20(1):103–110, 2012.

[2] T.O. Bertelsen. Installation of large subsea structures. Master's thesis, Norwegian University of Science and Technology, 2014.

[3] T. Bunnik and B. Buchner. Numerical prediction of wave loads on subsea structures in the splash zone. *Proceedings of the fourteenth international offshore and polar engineering conference*, 2004.

[4] J.B. Calvert. Theory of discharge from an orifice. 2003.

[5] I.M.C Campbell, J. Wellicome, and P.A. Weynberg. An investigation into wave slamming loads on cylinders. *Wolfson Marine Craft Unit Report - University of Southampton*, (317), 1977.

[6] I.M.C Campbell and P.A. Weynberg. Measurement of parameter affecting slamming. *Wolfson Unit for Marine Technology - University of Southampton*, (317), 1980.

[7] S.K. Chakrabarti. *Hydrodynamics of Offshore Structures*. Springer Verlag, 1987.

[8] DNV. *C205 - Environmental conditions and environmental loads*. Det Norske Veritas, 1991.

[9] DNV. *H103 - Modelling and analysis of marine operations*. Det Norske Veritas, 2011.

[10] DNV. *H205 - Lifting Operations*. Det Norske Veritas, 2014.

[11] T. Dooling. Double pendulum with elastic rods model, January 2013.

[12] P. Dourmashkin. Mit course notes classical mechanics.

[13] R.A.W. Dubbers. *The equivalent stick model reviewed*. TU Delft, January 2004.

[14] O.M. Faltinsen. *Sea Loads on Ships and Offshore Structures*. Cambridge university press, 1990.

[15] O.M. Faltinsen. *Hydrodynamics of High-Speed Marine Vehicles*. Cambridge university press, 2005.

[16] G.L. Garrad Hassan. Offshore wind energy. *February*, 26:4, 2007.

[17] M. Greenhow and L. Yanbao. Added masses for circular cylinders near or penetrating fluid boundaries - review, extension and application to water-entry, -exit and slamming. *Ocean Engineering*, 14, 1987.

[18] N. Hall. *Isentropic Flow*. NASA, May 2015.

[19] S. Haver. On the prediction of extreme wave crest heights, 2002.

[20] L.H. Holthuijsen. *Waves in Oceanic and Coastal Waters*. TU Delft and UNESCO-IHE, 2007.

[21] Wire Rope Industries. Crane & lifting solutions. Technical report, 2014.

[22] I. Iyalla, M. Hossain, and J. Andrawus. Calculating hydrodynamic loads on pipelines and risers: Practical alternative to morison's equation. *Advanced Materials Research*, 367:431–438, 2012.

[23] T. Jacobsen, T.B.I. Naess, and D. Karunakaran. Comparison with full scale measurements for lifting operations. *Marine operations speciality symposium*, 2012.

[24] J.G. Jalon and E. Bayo. *Kinematic and Dynamic Simulation of Multibody Systems*. Springer-Verlag, 2009.

[25] J.M.J. Journée and W.W. Massie. *Offshore Hydromechanics*. Faculty of Mechanical Maritime and Materials Engineering, TU Delft, 2001.

[26] I.E. Kopsov and P.C. Sandvik. Analysis of subsea structure installation. *The Fifth International Offshore and Polar Engineering Conference*, 1995.

[27] D.P. Kroese. Why the monte carlo method is so important today. *WIRE's Comput Stat*, 6:386–392, 2014.

[28] L. Li et al. Analysis of lifting operation of a monopile for an offshore wind turbine considering vessel shielding effects. *Marine structures*, 39:287–314, 2014.

[29] Z.H. Ma et al. The role of fluid compressibility in predicting slamming loads during water entry of flat plates. *International Society of Offshore and Polar Engineers*, 2015.

[30] R.C. Mac-Camy and R.A. Fuchs. Wave forces on piles: a diffraction theory. *US Army Corps of Engineers, Beach Erosion Board*, (69), 1954.

[31] Marintek. *SIMO Theory Manual, Version 3.6, rev:2*, December 2009.

[32] T. Naess, J. Havn, and F. Solaas. On the importance of slamming during installation of structures with large suction anchors. *Ocean Engineering*, 89(1):99–112, 2014.

[33] F.G. Nielsen. How to estimate hydrodynamic coefficients applicable for lifting from the sea bed. 2007.

[34] Nobles. Wire rope & synthetic slings. Technical report, Nobles Big-Lift Division, 2009.

[35] Orcina, Ltd. *OrcaFlex Manual*, 2015.

[36] L. Park et al. Dynamic factor analysis considering elastic boom effects in heavy lifting operations. *Ocean Engineering*, 38:1100–1113, 2011.

[37] V. Ramamurti. *Mechanics of Machines*. Narosa Publishing House, India, 2002.

[38] A. Selvaag. Wave impact forces on complex structures during lowering through the splash zone. Master's thesis, Norwegian University of Science and Technology.

[39] N.J. Smith et al. The slam force on a flat plate in free flight due to impact on a wave crest. *Journal of Fluids and Structures*, 12:183–196, 1998.

[40] K.E. Thomsen. *Offshore wind: A Comprehensive Guide to Successful Offshore Wind Farm Installation*. Elsevier, 2014.

[41] USFOS. *Hydrodynamics, Theory Discription of use Verification*, October 2010.

[42] B. Valpy and P. English. Future renewable energy cost: offshore wind. how technology innovation is anticipated to reduce the cost of energy from european offshore wind farms. KIC InnoEnergy, BVG associates, 2014.

[43] l. van der Veen and S. van den Akker. Sound solutions, construction of offshore wind farms without underwater noise. Technical report, Stichting De Noordzee, 2012.

[44] T. von Karman. The impact on seaplane floats during landing. *National advisory committee for aeronautics*, 321.

[45] J.H. Vugts. *Handbook of bottom founded offshore structures*.

[46] J.W. Wagenaar and P.J. Eecen. Current profiles. Technical report, NoordzeeWind, 2010.

[47] H. Wagner. Über stoss- undgleitvorgänge an der oberfläche von flüssigkeiten. *Zeitsch. f. Angew. Math und Mech*, 12(4):193–235, 1932.

[48] Z.J. You. The statistical distribution of nearbed wave orbital velocity in intermediate coastal water depth. *Coastal Engineering*, 56:844–852, 2009.

TU Delft Delft University of Technology

SIEMENS